8-2008

A New Rough Wall Layer Modeling for Turbulent Flows Using the Brinkman Equation

Meng-Huang Lu
Western Michigan University

A NEW ROUGH WALL LAYER MODELING FOR TURBULENT FLOWS USING THE BRINKMAN EQUATION

by

Meng-Huang Lu

A Dissertation
Submitted to the
Faculty of The Graduate College
in partial fulfillment of the
requirements for the
Degree of Doctor of Philosophy
Department of Mechanical and Aeronautical Engineering
Dr. William W. Liou, Advisor

Western Michigan University
Kalamazoo, Michigan
August 2008

INFORMATION TO USERS

The quality of this reproduction is dependent upon the quality of the copy submitted. Broken or indistinct print, colored or poor quality illustrations and photographs, print bleed-through, substandard margins, and improper alignment can adversely affect reproduction.

In the unlikely event that the author did not send a complete manuscript and there are missing pages, these will be noted. Also, if unauthorized copyright material had to be removed, a note will indicate the deletion.

ProQuest LLC
789 E. Eisenhower Parkway
PO Box 1346
Ann Arbor, MI 48106-1346

ACKNOWLEDGMENTS

I would like to express appreciations to my academic advisor and committee chairperson, Dr. William W. Liou, who provided me with professional assistance and thoughtful guidance throughout the completion of my dissertation. My sincere gratitude should also go to the members of my committee, Dr. Christopher Cho, Dr. Tianshu Liu, and Dr. Peter Parker, who spent their precious time reviewing my work. Special thanks to Dr. Iskender Sahin who once served on the committee.

My most profound gratitude goes to my parents and parents-in-law for all the understanding, interest, love and financial support you provided throughout the whole time during my dream of pursuing the doctoral degree.

Finally, I would like to thank my lovely wife, Hen-Ju Lin, who always loves me, encourages me and takes care of family while I was absent. I also thank my children, Joann and David, for all your support and company while I working on this dissertation. This dissertation is dedicated to you for your love, support, and encouragement.

Meng-Huang Lu

TABLE OF CONTENTS

Table of Contents—continued

CHAPTER

Table of Contents—continued

CHAPTER

Table of Contents—continued

CHAPTER

Table of Contents—continued

CHAPTER

Table of Contents—continued

LIST OF FIGURES

List of Figures—continued

List of Figures—continued

List of Figures—continued

List of Figures—continued

NOMENCLATURE

b	channel width
C_f	skin friction coefficient
Da	Darcy number
d_p	effective diameter
H	channel height
K	permeability
k_s	roughness height
k_s^+	normalized roughness height
k_{eq}	equivalent sand roughness height
k_{eq}^+	normalized equivalent sand roughness height
k	turbulent kinetic energy
k^+	normalized turbulent kinetic energy
L	plate length
Re	Reynolds number
Re_θ	Reynolds number based on momentum thickness
R_t	turbulent Reynolds number
U_0	free stream velocity
U_b	bulk velocity
U_e	edge velocity
U^+	normalized velocity

Nomenclature—continued

u_τ	friction velocity
$u_i^+ u_j^+$	normalized Reynolds stress
u_i^+	normalized turbulence intensity
y	normal distance from the wall
y^+	normalized distance from the wall
ΔU^+	roughness function
δ	boundary layer thickness
δ^*	displacement boundary layer thickness
δ_B	thickness of roughness region
ε	dissipation rate of turbulent kinetic energy
ε_β	porosity
θ	momentum thickness
ν	fluid viscosity
ρ	fluid density

CHAPTER I

INTRODUCTION

Turbulent boundary layers over rough surfaces occur in a wide range of flows, such as boundary layers on naval vehicle platforms, turbomachinery, pipes, heat exchangers, as well as aircrafts and present great challenges and interests in aeronautical and mechanical engineering. Compared to the flow over smooth surfaces, surface roughness influences the flow structures in the turbulent boundary layer around the rough surface and causes the increase of drag and wall heat transfer. In general, a wall with surface roughness can be considered smooth when the roughness is embedded in the viscous sub-layer portion of the turbulent boundary layer. On the other hand, if the roughness height is large compared to the thickness of the viscous sub-layer, the surface resistance becomes independent of the viscosity and the rough surface is considered fully rough. Between the two conditions is the intermediately rough region. In order to quantify the range of roughness, a roughness Reynolds number k_s^+ is commonly introduced.

$$k_s^+ = \frac{u_\tau k_s}{\nu} \tag{1.1}$$

where u_τ denotes the friction velocity and k_s represents the roughness height. According to Nikuradse [1], a rough surface is considered aerodynamically smooth if $k_s^+ < 5$. For such surfaces, the wall shear is dominated by the viscous effect. For $k_s^+ > 70$, the surface is considered fully rough. The surface shear force is mainly contributed by the form drag of the roughness elements, instead of the viscous drag. For $5 < k_s^+ < 70$, the surface is intermediately rough, and both the viscous drag and the form drag are significant components of the total drag force. Schlichting [2] proposed to characterize roughness element by using equivalent sand roughness. Sand roughness has since frequently being used to correlate measured surface data [3-5]. It can be determined by using the velocity law of the wall for turbulent boundary layer [6] or the geometric features of the surface, such as the spacing, the shape, and the height of the roughness [7].

The effect of surface roughness has been considered in many experimental studies since Nikuradse [1]. Clauser [8,9] and Hama [5] suggested that the effect of surface roughness on the mean flow was confined to the inner layer causing an increase of the skin friction and the lowering of the log-law mean velocity profile, compared with that for smooth walls. This log-law velocity

downward shift is referred to as the roughness function ΔU^+ for k-type roughness, such as sandgrains and two-dimensional rods [10]. The roughness function ΔU^+ for k-type roughness has been found to vary with the Reynolds number based on the shear velocity and has been correlated to the equivalent sand roughness k_{eq}^+ in the fully rough regime. Clauser [8,9] and Hama [5] also found that the velocity defect form of the mean velocity in the outer region is independent of surface roughness. Many other measurements [11-21] have provided support to the universality of the velocity defect law. The collapse of the mean velocity defect profiles for rough and smooth walls is consistent with the wall similarity hypothesis of Townsend [22], stating that the rough wall and smooth wall boundary layers would have the same turbulence structures in the core part of the boundary layer at sufficiently high Reynolds numbers. Schultz and Flack [14,17] and Flack et al. [18,20] measured the turbulent boundary layers over flat plates with different k-type surface roughness, including packed uniform spheres, sandpaper, and woven meshes. The results of these studies support Townsend's wall similarity hypothesis. However, there are also measurements that suggest otherwise [23-28]. Krogstad et al. [24] and Krogstad and Antonia [25,26] conducted a series of works on comparing zero pressure gradient turbulent boundary layers over surface

roughness of two-dimensional rods and three-dimensional mesh screens. Keirsbulck et al. [27] measured zero pressure gradient turbulent boundary layers over rough wall of two-dimensional square bars. Their results show that the surface roughness changes the profile of the velocity defect in the inner region, which results in a higher degree of isotropy of the Reynolds normal stresses and modifies the Reynolds shear stress profiles in the outer region of the boundary layer. This indicates that the interaction of the inner and outer regions of the turbulent boundary layers over rough surfaces may be important in some cases.

Surface roughness also poses a major challenge to numerical simulations. This is true for Reynolds-averaged Navier-Stokes (RANS) type of engineering calculations and is particularly serious for direct simulations such as large eddy simulation (LES) and direct numerical simulation (DNS) [29]. For numerical calculations using RANS, surface roughness is often not resolved. Mathematical models for the effects of roughness on the mean flow and the heat transfer are used to provide a closure to the equations. The need for a closure modeling is normally met by modifying the existing models for turbulence. For example, the value of ω on the wall in the $k-\omega$ turbulence model [30] was altered to include the effects of wall roughness. A hydrodynamic roughness

length was added [31] to the two-layer $k-\varepsilon$ turbulence model [32]. The boundary conditions for k and ε were also adjusted accordingly. The success of this approach of adapting smooth-wall turbulence modeling formulations for surface roughness in RANS calculations is highly flow dependent. The discrete element approach models the regular array of discrete roughness elements by adding a form drag term in the momentum equations and also by accounting for the lockage effects of roughness in the continuity equation [33]. For direct simulation, the rough wall layer requires special care. The simulations are extremely demanding on computational resources with surface-fitted grids and the localized geometric variation can only be considered in an exact manner for limited types of roughness. Some sorts of modeling are normally used. For example, an artificial forcing to mimic the drag force generated by a distribution of zero-volume virtual cones was used in Miyake et al. [34]. A force field model [35] was proposed for the resolved scale in the LES framework for wavy wall geometry with superimposed fine-grain roughness. In comparison with the abundance of research on smooth wall modeling, there have been significantly less efforts that focus on developing mathematical modeling for rough walls, which is surprising considering the practical importance of the

rough-wall effects.

Before we introduce our own research objectives, we first provide reviews of the existing literature on experimental and numerical studies of rough wall turbulent boundary layer flows.

Review on rough wall experimental studies

The effect of surface roughness has drawn significant attentions in many experimental studies for the last few decades. Several reviews on turbulent boundary layers over rough walls can be found in the literature [11,36,37]. It is found that the magnitude of roughness function ΔU^+ is not only determined by k_s, but also depended on the geometry of surface roughness. Perry et al. [10] distinguished two major types of roughness based on behavior described by different laws in pipe flow experiments. The first type of the roughness was so-called k-type, as characterized by a smooth wall roughened with closely packed sandgrains, or with two-dimensional spanwise rods placed in even spacing along the streamwise direction. The roughness function of k-type roughness depends on a Reynolds number based on the shear velocity and on a length associated with the size of the roughness. The second type of the roughness was so-called d-type, as characterized by a wall roughened with two-dimensional narrow spanwise grooves or cavities

placed in even spacing along the streamwise direction. The roughness function of d-type roughness does not depend on the roughness scale. Instead, it depends on the pipe diameter in rough pipe flows. It is also found out that d-type roughness satisfies the Rotta's condition of exact self-preservation [38]. Many experimental studies provide evidences supporting this condition [10,12,39-41]. The roughness function of k-type roughness in turbulent boundary layer flows is proved identical to that in pipe flow [1,3,4], yet experimental support for roughness function of d-type roughness in turbulent boundary layer flows is lacking.

k-type roughness

For k-type roughness in the fully rough regime, many experimental measurements were carried out on turbulent boundary layers over flat plates with surface roughness of closely packed uniform spheres [17], sandpaper [14-16,18,20,21,42], cylinder [43,44], perforated plate [15,16], two-dimensional spanwise rods [13,24-27], and three-dimensional mesh [13,15,16,18,20,24,26,42].

Akinlade et al. [15] performed experimental investigations on the velocity defect profiles of zero pressure gradient turbulent boundary layers over a hydraulically smooth surface and three different rough surfaces of sandpaper, perforated plate, and woven wire

mesh. The flows were considered in both transitionally and fully rough regimes and Reynolds numbers based on momentum thickness ranged from 3730 to 12,260. Their results showed that the velocity defect profiles in the outer region collapsed onto the same curve regardless different Reynolds numbers and surface roughness when employing a mixed outer scale. Although the velocity defect profiles collapsed on different surfaces using mixed outer scale, some significant differences, such as the strength of wake, continue to exist between smooth and rough wall flows even in the outer region. Bergstrom et al. [16] proposed a new skin friction correlation for a zero pressure gradient turbulent boundary layer over flat plates with surface roughness of sandpaper, perforated plate, and woven mesh. The flow Reynolds number based on momentum thickness ranged from 3730 to 13,550. The skin friction coefficient, C_f, was correlated to the ratio of the displacement thicknesses to boundary layer thicknesses, δ^* / δ, accounting for the effects of Reynolds number and surface roughness.

Schultz and Flack [17] measured turbulent boundary layer over a flat plate with two types of surface roughness, closely packed uniform spheres and the same roughness covering with a finer-scale grit. The Reynolds number based on momentum thickness ranges from 3000 to 15000. Their results indicated that roughness texture has

no effect on the downward shift of the mean log-law velocity profile when using the maximum peak to trough height as the roughness length scale. The Reynolds stress profiles for two measured surface roughness showed good agreement across the entire boundary layer and collapsed with smooth wall results outside of the roughness sublayer. However, departures from wall similarity may be observed for rough surfaces where the ratio of five equivalent sand roughness heights to the thickness of the inner layer is large than 0.2. Flack et al. [18] measured turbulent boundary layer over flat plates covered with sandpaper and woven mesh roughness at Reynolds number based on momentum thickness about 14,000. The ratio of the boundary layer thickness to the equivalent sand roughness height is greater than 40. Their results provide strong support for Townsend's wall similarity hypothesis [22] for uniform three-dimensional roughness. Flack et al. [20] investigated the critical roughness height for outer layer similarity between smooth and rough wall turbulent boundary layers with two surface roughness, sandpaper and woven mesh. The ratio of the boundary layer thickness to roughness height, δ / k_s, varies from 16 to 110 at Reynolds number based on momentum thickness between 7300 and 13,000. Their results indicate that a critical roughness height, where the roughness begins to affect most or all of the boundary

layer, does not exist. Connelly et al. [42] carried out velocity profile measurements in zero pressure gradient turbulent boundary layer flow over a smooth wall and rough walls with roughness of sandpapers including a wide range of roughness heights. The ratio of the boundary layer thickness to the roughness height, δ/k_s, ranged from 16 to 110, while the ratio of the boundary layer thickness to the equivalent sand roughness height, δ/k_{eq}, ranged from 6 to 91. Their results provide evidence that roughness effects on the mean flow are confined to the inner layer. The outer layer similarity of the mean velocity profile is still valid even for relatively large roughness. Similarity in the velocity-defect profiles between smooth and rough walls is always applicable when the rough wall has reached streamwise self-similarity.

Brzek et al. [21] reported the effects of roughness and Reynolds number on the velocity and Reynolds stress profiles in inner and outer variables for zero-pressure-gradient turbulent boundary layer over sandpapers. All velocity profiles collapsed using the scaling of Zagarola and Smits [45]. The results of the Reynolds stresses in the inner region showed that the roughness has the largest influence on the streamwise component of the Reynolds normal stresses. The Reynolds stresses in outer variables also showed self-similarity for fixed experimental conditions. For increasing roughness height,

k_s^+, the results showed that all Reynolds stress profiles became similar in shape indicating that the Reynolds stresses become more isotropic near the wall.

George and Simpson [43,44] reported turbulent structures of two- and three-dimensional turbulent boundary layers over flat plates with roughness of cylinders. They showed that the major contributors to the transport rates of Reynolds stresses are production and turbulent diffusion from the term by term evaluation of the various terms in the transport-rate equations for the Reynolds stresses. For both two- and three-dimensional rough wall turbulent boundary layers, the turbulent kinetic energy balance revealed that dissipation is an important term, in addition to the production and turbulent diffusion term. Most of the turbulent kinetic energy is produced in the neighborhood of the top of the roughness element and is transported away from this region by the velocity fluctuations. The distributions of three components of mean vorticity were also examined. For two- and three-dimensional rough wall turbulent boundary layers, the distributed roughness elements generate a large amount of vertical vorticity close to the top of the roughness element. High levels of spanwise vorticity are also generated close to the top of the roughness element with magnitudes greater than either of those for the other two components of vorticity. In

addition, the vortical structures do not persist in the streamwise distance since they are overcome by the subsequent sweeps of high momentum fluid that occur over the top of the next downstream element.

A series of works has been conducted on comparing zero pressure gradient turbulent boundary layer over surface roughness of rods and mesh-screen [13,24,26]. The two rough surfaces have very different surface geometries although designed to produce the same roughness function that have nominally the same effect on the mean velocity profile. The general implication is that different roughness geometries with the same ΔU^+ will have similar turbulence characteristics, at least at a sufficient distance from the roughness elements. However, significant differences in the Reynolds stresses, especially those involving the wall-normal velocity fluctuation, over the outer region have been observed. It is claimed that if the boundary layer is constantly fed by information from the wall region which is uniquely connected to the surface geometry, this information will eventually affect the outer layer to such a degree that the flow will be modified compared to the flow over a smooth surface. The differences are such that the Reynolds stress anisotropy is smaller over the mesh-screen roughness than the rod roughness. The Reynolds stress anisotropy is largest for a smooth wall. There is

nonetheless evidence that for the three-dimensional roughness, the small scales are more closely isotropic than for either the two-dimensional roughness or the smooth wall. Keirsbulck et al. [27] measured zero pressure gradient turbulent boundary layer over rough wall of two-dimensional square bars. The energy budget analysis showed that the transport terms are larger for smooth-wall than those for rough-wall near the wall. Their results also indicated that the vertical component of the velocity is more sensitive to the roughness effect than the longitudinal component, especially in the near wall regions as it has been observed earlier by other authors [13,26].

The experimental studies of k-type roughness showed that the roughness function ΔU^+ cannot be determined only by the roughness height k_s. It is believed that equivalent sand roughness plays a more important role among various roughness types for mean flow effects, and should be more effective than roughness height k_s itself in defining the extent of the roughness sublayer [17,46]. However, it cannot be predicted a *priori* for a generic roughness from measurements of the roughness alone. Further research is needed to identify the physical length scale that best characterizes a generic rough surface.

d-type roughness

The major distinction between k-type and d-type roughness is that the roughness function ΔU^+ of d-type roughness is not proportional to the roughness height k_s. Although there were several experimental studies on turbulent boundary layers over d-type rough wall [47-51], the interaction between the cavities or narrow spanwise grooves and the shear layer of the flow is not fully understood [37]. Perry and Li [47] carried out experimental measurements on turbulent boundary layers over smooth walls as well as k-type and d-type rough walls at various Reynolds numbers. They provided strong support to Townsend's [22] attached eddy hypothesis according to the experimental results of spectral and the broadband turbulence intensity. Choi and Fujisawa [48] experimentally investigated the turbulence structure of the boundary layer over a two-dimensional square cavity on a flat plate. Their results indicated a small reduction in total drag according to measurements of pressure coefficient and friction coefficient on a turbulent boundary layer over d-type roughness. Matsumoto [49] measured mean velocity profiles in two-dimensional zero pressure gradient turbulent boundary layers over spanwise grooved rough walls with the ratio of spacing to width of groove ranging from 10 to 40. The experimental

results showed that the characteristics of the measured rough wall boundary layer are somewhat different from those of the past d-type rough wall boundary layer. The equilibrium state could exist for the measured rough wall boundary layer. However, its region became narrower as the ratio of spacing to width of groove increased, and formed a line to distinguish between smooth wall and rough wall boundary layers when this ratio went beyond 30. Furthermore, a drag reduction was found in a boundary layer over rough walls for the ratio of spacing to width of groove is between 10 and 20. Djenidi et al. [50,51] performed experimental studies on a turbulent boundary layer over two-dimensional spanwise square cavities placed along streamwise direction. They visualized the ejections of cavity fluid into the outer flow as well as fluid flows into the cavities. Their results also showed that all the Reynolds stresses are larger over the d-type rough wall comparing to those of smooth wall, indicating that the strong momentum exchange is associated with the interaction between inflow and outflow of cavity fluid. It is conjectured that outflows play an important role in maintaining the level of turbulent energy in the layer and enhancing the approach towards self-preservation.

Review on rough wall numerical studies

Direct simulation type roughness modeling

Surface roughness alters the flow structure in the turbulent boundary layer near the wall and causes the increase of drag and wall heat transfer. DNS, LES, and RANS have been employed to examine the turbulent flows over rough surfaces. There are two commonly used approaches in DNS and LES to simulate the effect of surface roughness. The first approach accounts for the blockage effect of the roughness element on the flow by adding a form drag term in the momentum equation [34,52-54]. The coefficient for the form drag term is determined a *priori* by examining the corresponding experimental data. The second is the body force/immersed boundary method [35,55-57] where the no-slip boundary is enforced via a body force term.

Miyake et al. [34,52] employed DNS to investigate the turbulent flow in a channel bounded by one rough and another smooth wall with periodic conditions in streamwise and spanwise directions. The rough wall was modeled as line force by a distribution of zero-volume "virtual" cones for the sand-grain roughness, and external force [55] for two-dimensional spanwise ribs. Mean flow property of velocity and thermal fields are

found to be little influenced by the property of roughness elements but depends on total drag, except for in the layer close to the wall where direct interference with roughness elements manifests itself. The mixing is found to be controlled by large scale motion which is inherent to the logarithmic layer, getting closer to the wall. Li and Shao [53] performed LES on turbulent flows over arrays of roughness elements positioned on a smooth surface. The drag force term was inserted as a sink term in the momentum equations and the numerical results showed that drag partition depends not only on the magnitude of the roughness frontal area but also on the sizes and arrangement of roughness elements. The results indicated that the pressure drag coefficient is sensitive to roughness-element dimensions, and the arrangement of roughness elements may lead to different interferences of turbulent wakes. The impact of the latter factor is not insignificant. Scotti [54] developed a new method to simulate the effects of a roughened surface on a turbulent boundary layer using DNS. The uniform body force term that coupled with friction velocity was introduced in the momentum equations and the flow is forced by this term acting in the streamwise direction at Reynolds number based on the friction velocity of 1000. However, it is not meant to precisely reproduce the flow near the roughness but to account for its effects on the

flow above.

In the body force/immersed boundary method, Goldstein et al. [55] employed the immersed boundary technique to model a riblet covered surface on one wall of a fully developed turbulent channel flow using DNS. The beneficial drag reduction effect of riblets is a result of the damping of cross-flow velocity fluctuations, and the damping effect is explicitly modeled by applying a cross-flow damping force field in elongated streamwise zones with a height and spacing corresponding to the riblet crests. The simulation results supported cross-flow damping as a beneficial mechanism of drag reduction effect of riblets. Lee [56] performed LES of rough-wall channel flow with periodic conditions in streamwise and spanwise directions using the virtual boundary method to represent a rough surface. Typical downward shifts in mean velocity profile in the log region were observed with no variation of the slope. However, the uncertainty of the subgrid-scale model in the roughness region and a lack of validity of the virtual forcing method in turbulence simulation posed major drawbacks in this numerical study. Bhaganagar et al. [57] carried out a numerical investigation on the effects of surface roughness in turbulent incompressible plane-channel flow with periodic conditions in streamwise and spanwise directions between a smooth wall and one

covered with regular three-dimensional roughness elements using DNS. They concluded that roughness tends to increase the intensity of the velocity and vorticity fluctuations in the inner layer, while in the outer layer, the roughness alters the velocity fluctuations, yet the vorticity fluctuations are relatively unaffected. Moreover, the streamwise and spanwise dimensions of roughness elements of fixed height play a crucial role in determining whether the roughness affects the outer layer. The spanwise size of the roughness does not influence the mean velocity statistics, but does have a large impact on the velocity fluctuations in the outer layer. This may explain why investigators with different roughness geometries can observe similar roughness function ΔU^+, but offer different interpretations of the outer-layer physics based on their observations of higher-order statistics in the outer layer.

RANS type roughness modeling

For the numerical calculation using RANS, the averaged effect of surface roughness is modeled. One commonly used approach is adding form drag terms in the governing equations to account for the roughness effect [58-63]. However, the coefficients in the model formulations for the form drag are flow-specific [58-61,63].

Taylor et al. [58-60] developed a discrete element model for turbulent flow over rough surfaces. This formulation includes surface roughness form drag and blockage effects as a constituent part of the partial differential equations and does not rely on a single-length-scale concept such as equivalent sand roughness. The roughness model includes the necessary empirical information on the interaction between three-dimensional roughness elements and the empirical input was determined using data from well-accepted experiments. The results indicated that the discrete element approach of two-dimensional rib-type roughness rib-type roughness has a more narrow range of application for different surface geometries than the discrete element approach of three-dimensional, a mixture of cones and hemispheres distributed roughness. Tarada [61] introduced a complementary roughness drag coefficient model into a low Reynolds number k-ε model. The formulation of the complementary roughness drag coefficient model takes into account the isolated, wake interference and skimming roughness flow regimes, and is calibrated on a wide range of published experimental data concerning flow over deterministic roughness. However, detailed knowledge of the roughness element is needed to employ this model. Yamamoto [63] employed the virtual force model that represents the effect of each roughness element on the

mean flow field into a low-Reynolds-number k-ε turbulence model. The coefficients of the forcing terms were determined through the computational optimization of the experimental measurements on k-type and d-type roughness that were used to compare with the simulation results. The predictions in the mean flow velocity were in good agreements with experimental data, yet the turbulent kinetic energy and Reynolds shear stress for d-type roughness were over-predicted. The turbulence transport for k-type roughness element is away from the wall; in the contrast, toward to the wall for d-type roughness element. Therefore, the forcing terms that were computational optimized in k and ε equations predicted well for k-type roughness element, yet over-predicted in d-type roughness element.

RANS-based calculations have also been performed by using roughness models modified from the existing turbulence models developed for smooth wall flows [31,64-67]. Krogstad [64] modified the damping function of van Driest [68] to reproduce the roughness function for large roughness. Youn et al. [65] employed the standard k-ε model with wall function to predict the friction factor valid for Reynolds number between 10^5 to 10^7 in the rectangular duct with one side rib-roughened. A method for predicting the friction factor using existing correlations for smooth and rough walls was developed.

A common approach adopted in the numerical modeling of roughness is to relate the roughness effects to an equivalent sand roughness, thereby ignoring any possible dependence of the turbulent flow structure on the specific surface geometry. Zhang et al. [66] proposed a low-Reynolds-number k-ε model to simulate turbulent flow over smooth and rough surfaces by including the equivalent sand roughness k_{eq}^{+} into the damping functions of van Driest [68], and Lam and Bremhorst [69]. The predictions of skin friction coefficient and log-law velocity shift showed good agreement with the experimental measurements of fully developed rough pipe and duct flows of Reynolds number between 5×10^{3} and 5×10^{7} and the equivalent sand roughness k_{eq}^{+} from 0 up to 1000. Foti and Scandura [67] developed a low-Reynolds-number k-ε model for oscillatory flows over smooth and rough surface based on the model of Lam and Bremhorst [69]. The results showed the model is capable of reproducing the wall stresses, velocity profile and boundary layer thickness of steady and oscillatory flows. However, the implementation of this model requires the equivalent sand roughness k_{eq}^{+} which is best determined using measured data. In light of the practical importance of the surface roughness effects in many engineering problems, there is a need to develop mathematical models for RANS-type calculations, which allows for predictive calculations of

such flows.

Objectives of the research

It is proposed herein to develop a new flow physics-based modeling of surface roughness effects for the RANS numerical calculations of high-Reynolds-number turbulent flows over rough walls. The developed roughness modeling will improve the current predictive capability of the roughness effects. The developed predictive capabilities can be applied to advance technologies critical to Navy operations such as laminar/turbulent flow control, drag reduction and noise control.

In the roughness near-wall layer, the fluid flows through the openings in-between the roughness elements. In other words, the flow is essentially being forced to move through spaces that are partially blocked and partially free to go through. A similar scenario can be found in porous medium flows [70], where the fluid flows through pores and openings. Other than the geometric similarities, the two flows are both viscous dominated due to the large wetted area with embedded regions of shear and the local Reynolds number tends to be low. The geometric and the dynamic similarities between these two types of flows are important. It naturally leads to a hypothesis that one can apply the model equations that have been developed for one flow to the other flow; in

this case, from the porous medium flow to surface roughness flow.

The developed model explicitly recognizes the inhomogeneous nature of the medium in the roughness region. The dynamics of the fluid flow is filtered through volume averaging, which gives rise to the Brinkman equation [71] frequently used in the study of flow through porous media. The geometry and the formation of the surface roughness are accounted for through porosity that can be calculated mathematically, and permeability. The proposed exploratory use of the Brinkman equation is innovative, since this widely used approach in porous medium flow calculations has never been applied to the modeling of the rough wall effects on high-Reynolds-number flows.

New flow physics-based modeling approach

Turbulent flows over a permeable wall have been considered in many studies [72-80]. The turbulence transport equations in both porous medium region and homogeneous fluid region were derived by using both volume and time averaging processes [72-77]. Silva and de Lemos [78] numerically investigated the turbulent channel flows with a permeable wall using the turbulence k-ε model with wall function, while DNS was employed in the study of Breugem [79]. Based on the non-local form of the

volume averaged momentum equation, the interface condition developed by Ochoa-Tapia and Whitaker [81,82] can be applied at the boundary between a porous medium and a homogeneous fluid region as a jump condition in the stress and a continuous velocity field. The interface jump condition of the turbulent kinetic energy was proposed in the study of de Lemos and Silva [80]. One unique set of transport equations was applied to both regions. The effects of the Reynolds number, porosity, permeability, and jump coefficient on the mean and turbulence fields were investigated.

The Brinkman equation [71] has long been used in studying the averaged flows through complex porous media numerically [83-90] and experimentally [91-94]. The Brinkman equation is a generalized Darcy's law [70] and can be written as, by neglecting the Forchheimer term at small local Reynolds number

$$\frac{1}{\rho}\langle \nabla P \rangle = \nu \frac{\varepsilon_\beta}{K} \langle \mathbf{u} \rangle + \nu \nabla^2 \langle \mathbf{u} \rangle \qquad (1.2)$$

where $\mathbf{u}$ is fluid velocity in the porous media, and $\langle\ \rangle$ denotes the volume average. In general, the Forchheimer term depends on the local Reynolds number, based on the geometrical parameters of the porous medium, and represents the correction for inertial effects at high

Reynolds number. For small Reynolds number, the inertial effect is negligible, and so is the Forchheimer term. Equation (1.2) accounts for the viscous shear effects, the viscous damping effects, and the pressure gradient effects in the low Reynolds number region in porous media. The solutions of the Brinkman equation represent the averaged flow field in a partially blocked physical space. The Brinkman equation has been used to facilitate the matching of boundary conditions at the interface between the larger pores and the permeable medium [83-90]. The matching boundary conditions at the interface can be the continuity of the fluid velocity and the pressure between the Brinkman equation and the Navier-Stokes equations solutions.

In light of the geometric and the dynamic similarities between the porous medium flow and the surface roughness flow, it is proposed herein to use the Brinkman equation to model the averaged flow in the surface roughness layer of the turbulent boundary layer flow, while the outer free flow region of the turbulent boundary layer will be modeled by the RANS equations. A porous medium model for surface roughness was initially proposed by Shukla [95] in tribology. Tichy [96] applied the model and treated the rough surface as a porous film in the analysis of the magnetic head flying above the rotating disk in a hard-disk drive.

In this study, the development of a modeling framework based on such an assumed similarity is described. Boundary layer types of flows are considered. The flow domain is divided into a rough wall layer where the effects of roughness are modeled and an outer free flow region with fluid only. The fluid dynamics of the averaged flow in the rough wall layer is resolved by using the Brinkman equation, while the RANS equations are employed in the outer free flow region. For the Reynolds stress closure, a two-equation k-ε model and second-order closure have been developed. The model incorporates roughness-related closures to an existing, smooth wall, low-Reynolds-number model [97] as well as a second-order closure [98] and is employed in both the rough wall and the free flow regions. The porosity that appears in the Brinkman equation is determined based on the geometry and the formation of the roughness element. An interface condition [81,82] for the mean velocity and the stresses are applied at the interface between the rough wall and the free flow regions.

CHAPTER II

MATHEMATICAL FORMULATIONS

An incompressible turbulent boundary layer is considered to develop over a surface roughness region as shown in Figure 1. The rough wall layer, over which the turbulent boundary layer develops, is considered thin in comparison with the thickness of the turbulent boundary layer, or $\delta_B << \delta$, and undeformable. The local Reynolds number of the flow in roughness region is small. An interface exists where the fluid flow weaves in between the two flow regimes.

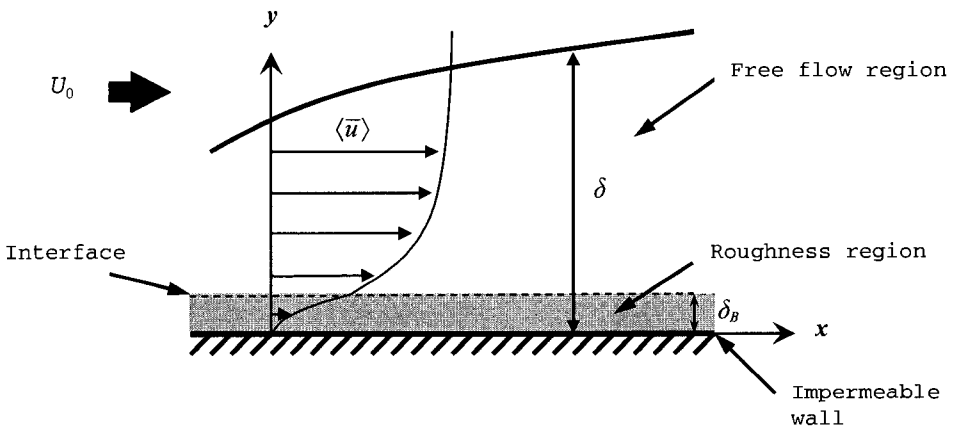

Figure 1. Sketch of the present flow model.

To incorporate the fact that a typical volume of space can be only partially occupied by fluid in the roughness region, the volume average method [99] is used. For a fluid property φ associated with the fluid phase β, as shown in Figure 2, the intrinsic average can be defined as

$$\langle\varphi\rangle^{\beta} = \frac{1}{\Delta V_{\beta}} \int_{\Delta V_{\beta}} \varphi \, dV \tag{2.1}$$

Similarly, the superficial average can be defined as

$$\langle\varphi\rangle = \frac{1}{\Delta V} \int_{\Delta V} \varphi \, dV \tag{2.2}$$

where ΔV_{β} represents volume occupied by the fluid phase in the averaging volume ΔV. The volume fraction of the fluid phase is generally used as a measure of the porosity ε_{β} of the porous medium defined as

$$\varepsilon_{\beta} = \frac{\Delta V_{\beta}}{\Delta V} \tag{2.3}$$

The fluid property φ can be defined as the sum of the intrinsic volume average and a deviation φ'',

$$\varphi = \langle\varphi\rangle^{\beta} + \varphi'' \tag{2.4}$$

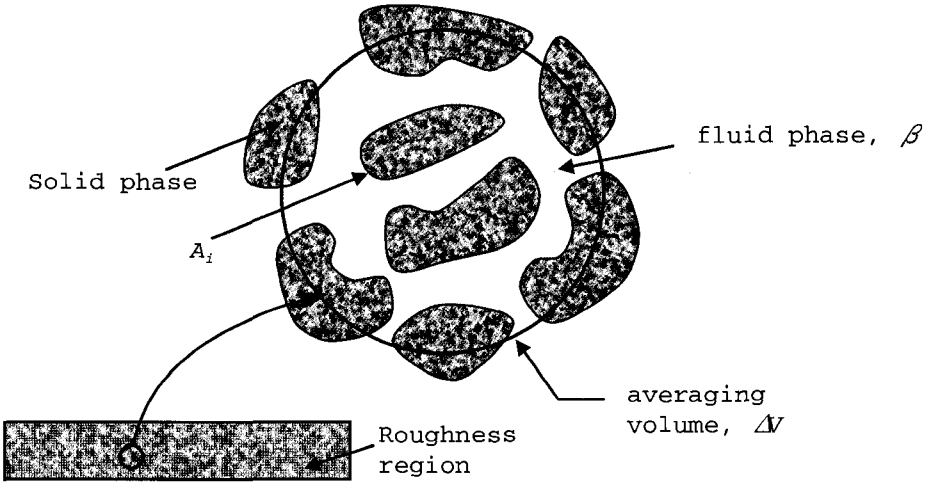

Figure 2. Macroscopic region and local averaging volume.

The time average value of a fluid property φ associated with the fluid is given as

$$\overline{\varphi} = \lim_{T \to \infty} \frac{1}{T} \int_{t_0}^{t_0+T} \varphi \, dt \tag{2.5}$$

where T is the integration time interval. The instantaneous property can be defined as the sum of the time average and the fluctuating component φ',

$$\varphi = \overline{\varphi} + \varphi' \tag{2.6}$$

It is easy to show that $\langle \overline{\varphi} \rangle = \overline{\langle \varphi \rangle}$, $\langle \varphi' \rangle = \langle \varphi \rangle'$, $\overline{\varphi}'' = \overline{\varphi''}$, and

$\varphi'' = \varphi''$ [77].

The volume average theorem [99] can be used to relate the volume average of a spatial derivative to the spatial derivative of the volume average

$$\langle \frac{\partial \varphi}{\partial x_i} \rangle = \frac{\partial \langle \varphi \rangle}{\partial x_i} + \frac{1}{\Delta V} \int_{A_i} n_i \varphi \, dA \tag{2.7}$$

where A_i represents the interface area and n_i is the surface normal vector. From the substitution of $\varphi = 1$ into Eq. (2.7), the following relation can be found for porosity,

$$\frac{\partial \varepsilon_\beta}{\partial x_i} = -\frac{1}{V} \int_{A_i} n_i dA \tag{2.8}$$

For constant porosity ε_β, then we have

$$\frac{1}{V} \int_{A_i} n_i dA = 0 \tag{2.9}$$

Derivation of volume-averaged governing equations

For an incompressible flow in homogeneous porous medium with constant porosity, the volume-averaged Navier-Stokes equations can be derived by applying the volume-average operator, $\langle\ \rangle$, to the Navier-Stokes

equations in the fluid phase

$$\langle \frac{\partial u_i}{\partial x_i} \rangle = 0 \tag{2.10}$$

$$\langle \frac{\partial u_i}{\partial t} \rangle + \langle \frac{\partial u_i u_j}{\partial x_j} \rangle = \langle - \frac{1}{\rho} \frac{\partial P}{\partial x_i} \rangle + \langle \nu \frac{\partial^2 u_i}{\partial x_j^2} \rangle \tag{2.11}$$

Applying the volume average theorem to the continuity equation (2.10) gives

$$\langle \frac{\partial u_i}{\partial x_i} \rangle = \frac{\partial \langle u_i \rangle}{\partial x_i} + \frac{1}{V} \int_{A_i} n_i u_i dA$$

Since solid phase is impermeable, u_i at A_i is 0. Therefore, the volume-averaged continuity equation becomes

$$\frac{\partial \langle u_i \rangle}{\partial x_i} = 0$$

Applying the volume average theorem to the first term in the left-hand side of the momentum equation (2.11), the unsteady term yields

$$\langle \frac{\partial u_i}{\partial t} \rangle = \frac{1}{\Delta V} \int_{\Delta V} \frac{\partial u_i}{\partial t} dV = \frac{\partial}{\partial t} \left\{ \frac{1}{\Delta V} \int_{\Delta V} u_i dV \right\} = \frac{\partial \langle u_i \rangle}{\partial t}$$

Applying the volume average theorem to the second term in the left-hand side of the momentum equation (2.11), the convective term, yields

$$\langle \frac{\partial u_i u_j}{\partial x_j} \rangle = \frac{\partial \langle u_i u_j \rangle}{\partial x_j} + \frac{1}{\Delta V} \int_{A_i} n_i u_i u_j dA = \frac{\partial \langle u_i u_j \rangle}{\partial x_j}$$

Applying the volume average theorem to the first term in the right-hand-side of the momentum equation (2.11), the pressure gradient term, yields

$$\langle - \frac{1}{\rho} \frac{\partial P}{\partial x_i} \rangle = - \frac{1}{\rho} \frac{\partial \langle P \rangle}{\partial x_i} + \frac{1}{\Delta V} \int_{A_i} - n_i \frac{P}{\rho} dA$$

Applying the volume average theorem to the second term in the right-hand-side of the momentum equation (2.11), the diffusion term, yields

$$\begin{aligned} \langle \nu \frac{\partial^2 u_i}{\partial x_j^2} \rangle &= \nu \frac{\partial}{\partial x_j} \langle \frac{\partial u_i}{\partial x_j} \rangle + \frac{1}{\Delta V} \int_{A_i} \nu \frac{\partial u_i}{\partial n} dA \\ &= \nu \frac{\partial^2 \langle u_i \rangle}{\partial x_j^2} + \frac{1}{\Delta V} \int_{A_i} \nu \frac{\partial u_i}{\partial n} dA \end{aligned}$$

Substitution of the above equations into Eqs. (2.10) and (2.11) gives the volume-averaged Navier-Stokes (VANS) equations as follows

$$\frac{\partial \langle u_i \rangle}{\partial x_i} = 0 \tag{2.12}$$

$$\frac{\partial \langle u_i \rangle}{\partial t} + \frac{1}{\varepsilon_\beta} \langle u_j \rangle \frac{\partial \langle u_i \rangle}{\partial x_j} = -\frac{1}{\rho} \frac{\partial \langle P \rangle}{\partial x_i} + \nu \frac{\partial^2 \langle u_i \rangle}{\partial x_j^2} - \frac{\partial \langle u_i'' u_j'' \rangle}{\partial x_j} + \frac{1}{\Delta V} \int_{A_i} \left[- n_i \frac{P}{\rho} + \nu \frac{\partial u_i}{\partial n} \right] dA \tag{2.13}$$

For an incompressible flow in homogeneous porous medium with constant porosity, the VANS equations with intrinsic velocity form can be expressed as follows,

$$\frac{\partial \langle u_i \rangle^\beta}{\partial x_i} = 0 \tag{2.14}$$

$$\frac{\partial \langle u_i \rangle^\beta}{\partial t} + \langle u_j \rangle^\beta \frac{\partial \langle u_i \rangle^\beta}{\partial x_j} = -\frac{1}{\rho} \frac{\partial \langle P \rangle^\beta}{\partial x_i} + \nu \frac{\partial^2 \langle u_i \rangle^\beta}{\partial x_j^2} - \frac{\partial \langle u_i'' u_j'' \rangle^\beta}{\partial x_j} + \frac{1}{\Delta V_\beta} \int_{A_i} \left[- n_i \frac{P}{\rho} + \nu \frac{\partial u_i}{\partial n} \right] dA \tag{2.15}$$

The last two terms in the right-hand-side of Eqs. (2.13) and (2.15) are the hydrodynamic dispersion due to spatial deviations [100] and the drag force that the solid phase exerts on the fluid phase, respectively. Carbonell and Whitaker [101] have shown that for constant porosity, the drag force can be expressed as

$$\frac{1}{\Delta V_\beta}\int_{A_i}\left[-n_i\frac{P}{\rho}+\nu\frac{\partial u_i}{\partial n}\right]dA=\frac{1}{\Delta V_\beta}\int_{A_i}\left[-n_i\frac{P''}{\rho}+\nu\frac{\partial u_i''}{\partial n}\right]dA \quad (2.16)$$

The budget equations for the volume-averaged dispersive stress equations of $\langle u_i''u_j''\rangle$ can be obtained as follows,

$$\begin{aligned}\frac{\partial\langle u_i''u_j''\rangle}{\partial t}+\frac{1}{\varepsilon_\beta}\langle u_k\rangle\frac{\partial\langle u_i''u_j''\rangle}{\partial x_k} &= -\frac{1}{\varepsilon_\beta}\left[\langle u_i''u_k''\rangle\frac{\partial\langle u_j\rangle}{\partial x_k}+\langle u_j''u_k''\rangle\frac{\partial\langle u_i\rangle}{\partial x_k}\right]\\ &-\frac{1}{\rho}\left(\frac{\partial\langle P''u_i''\rangle}{\partial x_j}+\frac{\partial\langle P''u_j''\rangle}{\partial x_i}\right)\\ &-\frac{\partial\langle u_i''u_j''u_k''\rangle}{\partial x_k}+\frac{1}{\rho}\langle P''\left(\frac{\partial u_i''}{\partial x_j}+\frac{\partial u_j''}{\partial x_i}\right)\rangle\\ &+\nu\frac{\partial^2\langle u_i''u_j''\rangle}{\partial x_k^2}-2\nu\langle\frac{\partial u_i''}{\partial x_k}\frac{\partial u_j''}{\partial x_k}\rangle\\ &+\frac{1}{\Delta V}\int_{A_i}\left[-\frac{P''}{\rho}\left(n_ju_i''+n_iu_j''\right)\right]dA\\ &+\frac{1}{\Delta V}\int_{A_i}\left[\nu\left(u_j''\frac{\partial u_i''}{\partial n}+u_i''\frac{\partial u_j''}{\partial n}\right)\right]dA \quad (2.17)\end{aligned}$$

A derivation of Eq. (2-17) is given in Appendix A. The volume-averaged dispersive stress equations, Eq. (2.17), is similar to the conventional time-averaged Reynolds stress equations, except for the last two term in the right-hand-side of Eq. (2.17) which are the form drag contributions generated by the obstacle element [73].

The transport equation for $e=\frac{1}{2}\langle u_i''u_i''\rangle$ can be obtained when inserting $i=j$ in Eq. (2.17) as follows,

$$\frac{\partial e}{\partial t} + \frac{1}{\varepsilon_\beta}\langle u_k\rangle\frac{\partial e}{\partial x_k} = -\frac{1}{\varepsilon_\beta}\langle u_i'' u_k''\rangle\frac{\partial\langle u_i\rangle}{\partial x_k} - \frac{1}{\rho}\frac{\partial\langle P'' u_i''\rangle}{\partial x_i} - \frac{\partial\,\frac{1}{2}\langle u_i'' u_i'' u_k''\rangle}{\partial x_k} + \nu\frac{\partial^2 e}{\partial x_k^2} - \nu\langle\frac{\partial u_i''}{\partial x_j}\frac{\partial u_i''}{\partial x_j}\rangle + \frac{1}{\Delta V}\int_{A_i}\left[-\frac{P''}{\rho}n_i u_i'' + \nu u_i''\frac{\partial u_i''}{\partial n}\right]dA \qquad (2.18)$$

The last term on the right-hand-side of Eq. (2.18) represents the work done by the drag force.

Derivation of time- and volume-averaged governing equations

For a turbulent incompressible flow in homogeneous porous medium with constant porosity, both time- and volume-average operators are employed to obtain the governing equations for modeling the turbulent flow.

Mean flow equations

To derive the time- and volume-averaged governing equations for the mean flow, the time-average operator is applied to the VANS equations, Eqs. (2.12) and (2.13), and the following forms can be obtained

$$\frac{\partial\langle\overline{u}_i\rangle}{\partial x_i} = 0 \qquad (2.19)$$

$$\frac{\partial\langle\overline{u}_i\rangle}{\partial t} + \frac{1}{\varepsilon_\beta}\langle\overline{u}_j\rangle\frac{\partial\langle\overline{u}_i\rangle}{\partial x_j} = -\frac{1}{\rho}\frac{\partial\langle\overline{P}\rangle}{\partial x_i} + \nu\frac{\partial^2\langle\overline{u}_i\rangle}{\partial x_j^2} - \frac{\partial\langle\overline{u_i''u_j''}\rangle}{\partial x_j} - \frac{\partial\langle\overline{u_i'u_j'}\rangle}{\partial x_j} + \frac{1}{\Delta V}\int_{A_i}\left[-n_i\frac{P''}{\rho} + \nu\frac{\partial u_i''}{\partial n}\right]dA \qquad (2.20)$$

The third and fourth terms in the right-hand-side of Eq. (2.20) are the dispersive flux and Reynolds stress terms, respectively. The last term in the right-hand-side of Eq. (2.20) is the time-averaged total drag force per unit volume due to solid particles, composed of both viscous and pressure drags [77].

Turbulence transport equations

It should be noted that applying the time- and volume-average operators in different sequences can lead to different turbulence governing equations [72-78]. Defining the turbulent kinetic energy in a porous medium flow is still an open question. Pedras and de Lemos [102] showed that the turbulent kinetic energy obtained by applying the time-average operator on top of the volume-average operator does not account for all of the turbulent kinetic energy associated with flow. Although there are differences in the turbulence governing equations obtained by using the two different approaches, the same final closure models for these equations can be reached when considering their respective turbulent

kinetic energies, i.e. $k = \frac{1}{2}\langle\overline{u_i' u_i'}\rangle$ and $k = \frac{1}{2}\overline{\langle u_i\rangle' \langle u_i\rangle'}$ [76,77].

In this study, the turbulence transport equations are derived in the manner of the volume-average operator on top of the time-average operator. The volume- and time-averaged Reynolds stress equation is as follows,

$$\begin{aligned}
\frac{\partial\langle\overline{u_i' u_j'}\rangle}{\partial t} + \frac{1}{\varepsilon_\beta}\langle\overline{u}_k\rangle\frac{\partial\langle\overline{u_i' u_j'}\rangle}{\partial x_k} = & \underbrace{-\frac{1}{\varepsilon_\beta}\left(\langle\overline{u_i' u_k'}\rangle\frac{\partial\langle\overline{u}_j\rangle}{\partial x_k} + \langle\overline{u_j' u_k'}\rangle\frac{\partial\langle\overline{u}_i\rangle}{\partial x_k}\right)}_{i} \\
& \underbrace{-\frac{\partial\langle\overline{u_i' u_j' u_k'}\rangle}{\partial x_k}}_{ii} \underbrace{-\frac{1}{\rho}\left(\frac{\partial\langle\overline{P' u_i'}\rangle}{\partial x_j} + \frac{\partial\langle\overline{P' u_j'}\rangle}{\partial x_i}\right)}_{iii} \\
& \underbrace{+\langle\overline{\frac{P'}{\rho}\left(\frac{\partial u_i'}{\partial x_j} + \frac{\partial u_j'}{\partial x_i}\right)}\rangle}_{iv} \underbrace{+\nu\frac{\partial^2\langle\overline{u_i' u_j'}\rangle}{\partial x_k^2}}_{v} \\
& \underbrace{-2\nu\langle\overline{\frac{\partial u_i'}{\partial x_k}\frac{\partial u_j'}{\partial x_k}}\rangle}_{vi} \underbrace{-\langle\overline{u}_k''\frac{\partial\overline{u_i' u_j'}''}{\partial x_k}\rangle}_{vii} \\
& \underbrace{-\left(\langle\overline{u_i' u_k'}''\frac{\partial\overline{u}_j''}{\partial x_k}\rangle + \langle\overline{u_j' u_k'}''\frac{\partial\overline{u}_i''}{\partial x_k}\rangle\right)}_{viii} \\
& \underbrace{+\frac{1}{\Delta V}\int_{A_i}\left[-\overline{\frac{P'}{\rho}\left(u_i' n_j + u_j' n_i\right)}\right]dA}_{ix} \\
& \underbrace{+\frac{1}{\Delta V}\int_{A_i}\left[\nu\left(\overline{u_j'\frac{\partial u_i'}{\partial n} + u_i'\frac{\partial u_j'}{\partial n}}\right)\right]dA}_{x} \qquad (2.21)
\end{aligned}$$

A derivation of Eq. (2.21) is given in Appendix B. Excluding terms *vii* to *x*, the remaining terms are similar

to those in the conventional time-averaged Reynolds stress equation, in which the time-averaged quantities have been replaced by volume- and time-averaged values. Term *vii* represents the local advection of local variations in stress, and term *viii* is the rate of production of local variations in rate of strain against local anomalies in stress [75]. Terms *ix* and *x* are the production of the stress by the correlation between the drag force per unit volume due to solid particles, composed by both viscous and pressure drags.

The transport equation for the turbulent kinetic energy, $k = \frac{1}{2}\langle\overline{u_i' u_i'}\rangle$, can be obtained when inserting $i = j$ in Eq. (2.21) as follows

$$\begin{aligned}\frac{\partial k}{\partial t} + \frac{1}{\varepsilon_\beta}\langle\overline{u}_k\rangle\frac{\partial k}{\partial x_k} = & \underbrace{-\frac{1}{\varepsilon_\beta}\langle\overline{u_i' u_k'}\rangle\frac{\partial\langle\overline{u}_i\rangle}{\partial x_k}}_{i} \underbrace{-\frac{\partial\,\frac{1}{2}\langle\overline{u_i' u_j' u_k'}\rangle}{\partial x_k}}_{ii} \underbrace{-\frac{1}{\rho}\left(\frac{\partial\langle\overline{P' u_k'}\rangle}{\partial x_k}\right)}_{iii} \\ & + \underbrace{\nu\frac{\partial^2 k}{\partial x_k^2}}_{iv} \underbrace{-\nu\langle\overline{\frac{\partial u_i'}{\partial x_k}\frac{\partial u_i'}{\partial x_k}}\rangle}_{v} \\ & \underbrace{-\frac{1}{2}\langle\overline{u}_k''\frac{\partial\overline{u_i' u_i'}''}{\partial x_k}\rangle}_{vi} \underbrace{-\langle\overline{u_i' u_k'}''\frac{\partial\overline{u}_i''}{\partial x_k}\rangle}_{vii} \\ & \underbrace{+\frac{1}{\Delta V}\int_{A_i}\left[-\overline{\frac{P'}{\rho}u_i' n_i + \nu u_i'\frac{\partial u_i'}{\partial n}}\right]dA}_{viii}\end{aligned} \qquad (2.22)$$

Term *vi* in Eq. (2.22) represents the local energy redistribution [73], and term *vii* in Eq. (2.22) is the

local production associated with spatial deviations of flow quantities [77]. Term *viii* in Eq. (2.22) represents the work done by the drag force.

Closure models

Momentum equations

Whitaker [103] studied the closure problem of the drag force, as shown in Eq. (2.16), and proposed the drag force, f_i, has the following form,

$$\begin{aligned} f_i &= \frac{1}{\Delta V_\beta} \int_{A_i} \left[- \frac{P''}{\rho} n_i + \nu \frac{\partial u_i''}{\partial n} \right] dA \\ &= - \nu \mathbf{K}^{-1} \cdot \langle u_i \rangle - \nu \mathbf{K}^{-1} \cdot \mathbf{F} \cdot \langle u_i \rangle \end{aligned} \tag{2.23}$$

Two widely used correlations in porous medium flow studies for the permeability tensor, $\mathbf{K}$, and the Forchheimer tensor, $\mathbf{F}$, can be expressed in the following form [99],

$$\mathbf{K} = \frac{\varepsilon_\beta^{\,3} d_p^{\,2}}{180\left(1 - \varepsilon_\beta\right)^2} \mathbf{I} \tag{2.24}$$

$$\mathbf{F} = \frac{1}{100\left(1 - \varepsilon_\beta\right)} \frac{d_p |\langle \mathbf{u} \rangle|}{\nu} \mathbf{I} \tag{2.25}$$

where d_p is the effective diameter, and $\mathbf{I}$ is the identity matrix. As has been frequently invoked in porous medium

studies, the Forchheimer tensor, Eq. (2.25), is assumed negligible, since the local Reynolds number of the flow in the roughness region is considered small [79]. We assume that the permeability is isotropic, $\mathbf{K} = K\mathbf{I}$, and apply the time-average operator to the drag force. Then we can obtain the drag force for the time-averaged VANS equations as

$$\overline{f_i} = -\frac{\nu}{K} \cdot \langle \overline{u}_i \rangle \tag{2.26}$$

The dispersive stress, $\langle \overline{u_i'' u_j''} \rangle$, is negligible in comparison to the volume-averaged Reynolds stress, $\langle \overline{u_i' u_j'} \rangle$ [75]. Therefore, the time-averaged VANS equations, Eq. (2.20), can be expressed as

$$\frac{\partial \langle \overline{u}_i \rangle}{\partial t} + \frac{1}{\varepsilon_\beta} \langle \overline{u}_j \rangle \frac{\partial \langle \overline{u}_i \rangle}{\partial x_j} = -\frac{1}{\rho} \frac{\partial \langle \overline{P} \rangle}{\partial x_i} + \nu \frac{\partial^2 \langle \overline{u}_i \rangle}{\partial x_j^2} - \frac{\partial \langle \overline{u_i' u_j'} \rangle}{\partial x_j} + \varepsilon_\beta \overline{f_i} \tag{2.27}$$

In the free flow region with homogeneous fluid only, there are no solid obstacles ($\varepsilon_\beta = 1$) and hence the drag force exerted on the flow is zero. In addition, $\langle \overline{u}_i \rangle = \overline{u}_i$ holds in the free flow region [79] and the time-averaged VANS equations reduce to the conventional RANS equations.

In the roughness region, the local Reynolds number of the flow is assumed small, and the effect of the Reynolds stress term and the left-hand side of Eq. (2.27)

can be neglected. Therefore, the time-averaged VANS equations can be simplified to

$$0 = -\frac{1}{\rho}\frac{\partial\langle\overline{P}\rangle}{\partial x_i} + \nu\frac{\partial^2\langle\overline{u}_i\rangle}{\partial x_j^2} - \varepsilon_\beta\overline{f_i} \tag{2.28}$$

which is the time-averaged Brinkman equation [71].

To form a closure model, the effective diameter d_p and the thickness of the roughness region δ_B need to be provided. We propose to relate d_p with the height of physical roughness k_s. This provides a direct link between the physical length scale and that needed for the modeling. The proposed expression satisfies the length scale constraint that d_p is small compared to k_s [99] and has the following form

$$d_p = (1-\varepsilon_\beta)^3\varepsilon_\beta{}^2 k_s \tag{2.29}$$

Similarly, the thickness, or the height, of the roughness region δ_B where the effects of the surface roughness are modeled, should also be related to the height of the actual roughness. In this work, the following form is used.

$$\delta_B = (1-\varepsilon_\beta)\varepsilon_\beta k_s \tag{2.30}$$

Second-order turbulence closure

For a second-order turbulence closure model with constant porosity, we have

$$\frac{\partial\overline{\langle u_i' u_j'\rangle}}{\partial t} + \frac{1}{\varepsilon_\beta}\langle\overline{u}_k\rangle\frac{\partial\overline{\langle u_i' u_j'\rangle}}{\partial x_k} = G_{ij} + \phi_{ij} - \varepsilon_{ij} + d_{ij} + \nu\frac{\partial^2\overline{\langle u_i' u_j'\rangle}}{\partial x_k^2} - F_{ij} \qquad (2.31)$$

Term *i* in Eq. (2.21) is the production term, G_{ij}, and can be solved directly.

$$G_{ij} = -\frac{1}{\varepsilon_\beta}\left(\overline{\langle u_i' u_k'\rangle}\frac{\partial\langle\overline{u}_j\rangle}{\partial x_k} + \overline{\langle u_j' u_k'\rangle}\frac{\partial\langle\overline{u}_i\rangle}{\partial x_k}\right) \qquad (2.32)$$

Term *vi* in Eq. (2.21) is the dissipation rate, and the assumption of local isotropy is adopted,

$$\varepsilon_{ij} = \frac{2}{3}\delta_{ij}\varepsilon \qquad (2.33a)$$

where

$$\varepsilon = \varepsilon_{ii}/2 = \nu\overline{\langle\frac{\partial u_i'}{\partial x_k}\frac{\partial u_i'}{\partial x_k}\rangle} \qquad (2.33b)$$

δ_{ij} is the Kronecker delta function. Terms *ii*, *iii*, and

vii in Eq. (2.21) are modeled as a total turbulent diffusion term using Hanjalic and Launder's [104] form

$$d_{ij} = \frac{\partial}{\partial x_k}\left(c_s \frac{k}{\varepsilon} \langle \overline{u_k' u_l'} \rangle \frac{\partial \langle \overline{u_i' u_j'} \rangle}{\partial x_l} \right) \tag{2.34}$$

Term *iv* in Eq. (2.21) is the pressure strain term, and the modeling of Launder and Shima [98] has been adopted. Four distinct contributions to the pressure strain are described as follows,

$$\phi_{ij} = \phi_{ij1} + \phi_{ij2} + \phi^w_{ij1} + \phi^w_{ij2} \tag{2.35a}$$

$$\phi_{ij1} = -c_1 \varepsilon a_{ij} \tag{2.35b}$$

$$\phi_{ij2} = -c_2 \left(G_{ij} - \tfrac{2}{3} \delta_{ij} G \right) \tag{2.35c}$$

$$\begin{aligned} \phi^w_{ij1} = {} & c^w_1 (\varepsilon/k) \left[\langle \overline{u_k' u_m'} \rangle n_k n_m \delta_{ij} \right. \\ & \left. - (\tfrac{3}{2}) \langle \overline{u_k' u_i'} \rangle n_k n_j - (\tfrac{3}{2}) \langle \overline{u_k' u_j'} \rangle n_k n_i \right] f_\phi \end{aligned} \tag{2.35d}$$

$$\phi^w_{ij2} = c^w_2 \left[\phi_{km2} n_k n_m \delta_{ij} - (\tfrac{3}{2}) \phi_{ik2} n_k n_j - (\tfrac{3}{2}) \phi_{jk2} n_k n_i \right] f_\phi \tag{2.35e}$$

where

$$c_1 = -1 + 2.58 A A_2^{1/4} \left(1 - exp\left[- \left(0.0067 R_t \right)^2 \right] \right) \tag{2.36a}$$

$$c_2 = 0.75A^{1/2} \tag{2.36b}$$

$$c_1^w = -\tfrac{2}{3} c_1 + 1.67 \tag{2.36c}$$

$$c_2^w = max\left[\left(\tfrac{2}{3} c_2 - \tfrac{1}{6}\right) / c_2, 0\right] \tag{2.36d}$$

$$a_{ij} = \left(\langle \overline{u_i' u_j'} \rangle - \tfrac{2}{3} \delta_{ij} k\right) k \tag{2.36e}$$

$$A = \left[1 - 9/8\left(A_2 - A_3\right)\right] \tag{2.36f}$$

$$A_2 = a_{ik} a_{ki} \tag{2.36g}$$

$$A_3 = a_{ik} a_{kj} a_{ji} \tag{2.36h}$$

$$G = \tfrac{1}{2} G_{kk} \tag{2.36i}$$

$$f_\phi = 0.4k^{3/2} / \varepsilon x_2 \tag{2.36j}$$

R_t is the turbulence Reynolds number defined as $k^2 / \varepsilon\nu$, and n_k is the unit vector perpendicular to the wall. Terms *viii* to *x* in Eq. (2.21) are modeled as forcing term [79] based on the assumption of isotropic partition [75].

$$F_{ij} = \frac{\delta_{ij}}{3} \overline{f}_k \langle \overline{u}_k \rangle \tag{2.37}$$

The transport equation for ε is

$$\frac{\partial \varepsilon}{\partial t} + \frac{1}{\varepsilon_\beta} \langle \overline{u}_k \rangle \frac{\partial \varepsilon}{\partial x_k} = \frac{\partial}{\partial x_k} \left[\left(c_\varepsilon \frac{k}{\varepsilon} \langle \overline{u_k' u_l'} \rangle + \nu \delta_{kl} \right) \frac{\partial \varepsilon}{\partial x_l} \right] + (c_{\varepsilon 1} + \psi_1 + \psi_2)(\varepsilon/k) G - c_{\varepsilon 2} (\varepsilon \tilde{\varepsilon}/k) - c_{\varepsilon_3} \frac{\varepsilon}{k} F_{ii} \quad (2.38)$$

where

$$\psi_1 = 2.5A(G / \varepsilon - 1) \quad (2.39a)$$

$$\psi_2 = 0.3(1 - 0.3A_2) \exp\left[- (0.002R_t)^2 \right] \quad (2.39b)$$

$$\tilde{\varepsilon} = \varepsilon - 2\nu \left(\frac{\partial k^{\frac{1}{2}}}{\partial x_2} \right)^2 \quad (2.39c)$$

The forcing term in Eq. (2.38) has been obtained by a simple scaling of the corresponding term in Eq. (2.31). As a result, the coefficient c_{ε_3} is a model constant. It was set at 0.11. In Eq. (2.34), c_s is the model constant, while c_ε, $c_{\varepsilon 1}$, and $c_{\varepsilon 2}$ in Eq. (2.38) are model constants as well. They have values of c_s = 0.11, c_ε = 0.18, $c_{\varepsilon 1}$ = 1.45, and $c_{\varepsilon 2}$ = 1.9.

Two-equation turbulence closure

For a two-equation ($k - \varepsilon$) turbulence closure model

with constant porosity, the low-Reynolds-number turbulence model of Launder and Sharma [97] has been adopted. The transport equation for k is

$$\frac{\partial k}{\partial t} + \frac{1}{\varepsilon_\beta}\langle \overline{u}_j \rangle \frac{\partial k}{\partial x_j} = \frac{\partial}{\partial x_j}\left[\left(\nu + \frac{\nu_{t_{eff}}}{\sigma_k}\right)\frac{\partial k}{\partial x_j}\right] + G - \varepsilon - D - \overline{f}_i \langle \overline{u}_i \rangle \tag{2.40}$$

$$D = 2\nu\left(\frac{\partial \sqrt{k}}{\partial x_2}\right)^2 \tag{2.41}$$

Term *i* in Eq. (2.22) is the production term, and can be solved directly as G in Eq. (2.40) with the Reynolds stress closure of

$$-\overline{\langle u_i' u_j' \rangle} = \nu_{t_{eff}}\left(\frac{\partial \langle \overline{u}_i \rangle}{\partial x_j} + \frac{\partial \langle \overline{u}_j \rangle}{\partial x_i}\right) - \frac{2}{3} k\delta_{ij} \tag{2.42}$$

where

$$\nu_{t_{eff}} = \frac{\nu_t}{\varepsilon_\beta} = \frac{1}{\varepsilon_\beta} C_\mu f_\mu \frac{k^2}{\varepsilon} \tag{2.43}$$

Terms *ii*, *iii*, *iv*, and *vi* in Eq. (2.22) are diffusion terms and appear as the first term in the right-hand-side of Eq. (2.40). Term *v* in Eq. (2.22) is the dissipation rate of the turbulent kinetic energy, ε, as the third term in the right-hand-side of Eq. (2.40). Terms *vii* and *viii* in Eq. (2.22) are modeled as forcing term, which is

the last term in right-hand-side of Eq. (2.40) [79].

The transport equation for ε is

$$\frac{\partial \varepsilon}{\partial t} + \frac{1}{\varepsilon_\beta} \langle \overline{u}_j \rangle \frac{\partial \varepsilon}{\partial x_j} = \frac{\partial}{\partial x_j} \left[\left(\nu + \frac{\nu_{t_{eff}}}{\sigma_\varepsilon} \right) \frac{\partial \varepsilon}{\partial x_j} \right] + C_1 f_1 \frac{\varepsilon}{k} G - C_2 f_2 \frac{\varepsilon^2}{k} + E - C_3 \frac{\varepsilon}{k} \overline{f}_i \langle \overline{u}_i \rangle \tag{2.44}$$

$$E = 2\nu\nu_{t_{eff}} \left(\frac{\partial^2 \langle \overline{u}_2 \rangle}{\partial x_2^2} \right)^2 \tag{2.45}$$

Similarly, the forcing term in Eq. (2.44) has been obtained by a simple scaling of the corresponding term in Eq. (2.40). As a result, the coefficient C_3 is a model constant. It was set at 0.11. The value of the model constants are σ_k = 1.0, σ_ε = 1.3, C_1 = 1.44, C_2 = 1.92, and C_μ = 0.09.

The damping functions f_μ, f_1, and f_2 proposed by Launder and Sharma [97] are,

$$f_\mu = exp\left[-3.4/(1 + R_t/50)^2 \right] \tag{2.46}$$

$$f_1 = 1 \tag{2.47}$$

$$f_2 = 1 - 0.3\, exp\left(-R_t^2 \right) \tag{2.48}$$

In the free flow region with homogeneous fluid only,

there are no solid obstacles ($\varepsilon_\beta = 1$) and hence the drag force exerted on the flow is zero. In addition, $\langle \overline{u}_i \rangle = \overline{u}_i$ holds in the free flow region [79]. The volume- and time-averaged turbulence transport equations for the Reynolds stresses and the turbulent kinetic energy in the free flow fluid region are also recovered to the conventional time-averaged turbulence transport equations.

Interface conditions

For the flow involving a wall roughness and an unobstructed free flow region, an interface is identified between the free flow and the roughness regions. The interface conditions developed by Ochoa-Tapia and Whitaker [81,82] assumed a jump relation for the intrinsic stresses and a continuous superficial velocity across the interface.

Second-order turbulence closure

For a second-order turbulence closure model with constant porosity, the interface conditions [81,82] are adopted for the averaged flow properties and the turbulence model quantities, $\langle \overline{u_i' u_j'} \rangle$ and ε, are assumed continuous.

$$\langle \overline{u} \rangle \big|_{\text{roughness}} = \langle \overline{u} \rangle \big|_{\text{free flow}} = U_I \tag{2.49}$$

$$\frac{\nu}{\varepsilon_\beta}\frac{\partial\langle\overline{u}\rangle}{\partial y}\bigg|_{\text{roughness}} - \nu\frac{\partial\langle\overline{u}\rangle}{\partial y}\bigg|_{\text{free flow}} - \langle\overline{u'v'}\rangle_I\left(\frac{1}{\varepsilon_\beta} - 1\right) = \nu\frac{\beta_t}{\sqrt{K}}\cdot U_I \quad (2.50)$$

$$\langle\overline{v}\rangle\big|_{\text{roughness}} = \langle\overline{v}\rangle\big|_{\text{free flow}} = V_I \quad (2.51)$$

$$\frac{\nu}{\varepsilon_\beta}\frac{\partial\langle\overline{v}\rangle}{\partial y}\bigg|_{\text{roughness}} - \nu\frac{\partial\langle\overline{v}\rangle}{\partial y}\bigg|_{\text{free flow}} - \langle\overline{v'v'}\rangle_I\left(\frac{1}{\varepsilon_\beta} - 1\right) = \nu\frac{\beta_n}{\sqrt{K}}\cdot V_I \quad (2.52)$$

$$1/\varepsilon_\beta \cdot \langle\overline{P}\rangle\big|_{\text{roughness}} = \langle\overline{P}\rangle\big|_{\text{free flow}} \quad (2.53)$$

$$\langle\overline{u_i'u_j'}\rangle\big|_{\text{roughness}} = \langle\overline{u_i'u_j'}\rangle\big|_{\text{free flow}} = \langle\overline{u_i'u_j'}\rangle_I \quad (2.54)$$

$$\varepsilon\big|_{\text{roughness}} = \varepsilon\big|_{\text{free flow}} \quad (2.55)$$

A derivation of interface stress jump conditions, Eqs. (2.50) and (2.52), is given in Appendix C. β_t and β_n are the tangential and normal stress jump parameters, respectively. The value of stress jump parameters might be chosen to accommodate engineering flows over porous media.

Two-equation turbulence closure

For a two-equation ($k-\varepsilon$) turbulence closure model with constant porosity, the interface conditions [78,79,81,82,] are adopted for the averaged flow

properties adopted for the averaged flow properties and the turbulence model quantities, k and ε, are assumed continuous.

$$\langle \overline{u} \rangle \big|_{\text{roughness}} = \langle \overline{u} \rangle \big|_{\text{free flow}} = U_I \tag{2.56}$$

$$\left(\frac{\nu}{\varepsilon_\beta} + \nu_{t_{eff}} \right) \frac{\partial \langle \overline{u} \rangle}{\partial y} \bigg|_{\text{roughness}} - (\nu + \nu_t) \frac{\partial \langle \overline{u} \rangle}{\partial y} \bigg|_{\text{free flow}} = (\nu + \nu_t) \frac{\beta_t}{\sqrt{K}} U_I \tag{2.57}$$

$$\langle \overline{v} \rangle \big|_{\text{roughness}} = \langle \overline{v} \rangle \big|_{\text{free flow}} = V_I \tag{2.58}$$

$$\left(\frac{\nu}{\varepsilon_\beta} + \nu_{t_{eff}} \right) \frac{\partial \langle \overline{v} \rangle}{\partial y} \bigg|_{\text{roughness}} - (\nu + \nu_t) \frac{\partial \langle \overline{v} \rangle}{\partial y} \bigg|_{\text{free flow}} = (\nu + \nu_t) \frac{\beta_n}{2\sqrt{K}} V_I \tag{2.59}$$

$$1 / \varepsilon_\beta \cdot \langle \overline{P} \rangle \big|_{\text{roughness}} = \langle \overline{P} \rangle \big|_{\text{free flow}} \tag{2.60}$$

$$k \big|_{\text{roughness}} = k \big|_{\text{free flow}} \tag{2.61}$$

$$\varepsilon \big|_{\text{roughness}} = \varepsilon \big|_{\text{free flow}} \tag{2.62}$$

β_t and β_n are the tangential and normal stress jump parameters, respectively. The value of stress jump parameters might be chosen to accommodate engineering flows over porous media. The results of de Lemos and Silva [80] showed that a negative tangential stress jump parameter gave results that agreed with the experimental

data for the turbulent kinetic energy at the interface.

In this study, we use β_t = -1 , and β_n = 5. The constants were set based on generally accepted values. They have not been selected nor optimized for the calculations results shown here.

Summary of mathematical formulations

In the current mathematical formulation of the Brinkman equation modeling approach, the model equations are developed based on existing smooth wall turbulence models and roughness-related model parameters are introduced. The parameters are d_p in Eq. (2.29), δ_B in Eq. (2.30), c_{ε_3} in Eq. (2.38), and C_3 in Eq. (2.44).

For the mean flow, the fluid dynamics of the averaged flow is resolved using Eqs. (2.19) and (2.27). The turbulent quantities needed for closures are resolved using Eqs. (2.31) and (2.38) for a second-order turbulence closure, and using Eqs. (2.40) and (2.44) for a two-equation turbulence closure. The interface conditions, Eqs. (2.49)-(2.55) for a second-order turbulence closure and Eqs. (2.56)-(2.62) for a two-equation turbulence closure, enforced the continuity of velocity, pressure, and turbulence properties, and the stress jump conditions at the interface between the roughness and the free flow regions.

CHAPTER III

NUMERICAL METHODS

The numerical methods used in this study utilize the partial transformation approach, with the velocity components expressed in Cartesian coordinates. The appropriate forms of the incompressible dimensionless governing equations with constant porosity in generalized curvilinear coordinates are presented. The governing equations are discretized on a non-staggered mesh using the following techniques: second-order accurate three-point central finite differencing for the divergence operator in the continuity equation and the pressure pressure gradient, viscous, and Reynolds stress terms in the momentum equations; and second-order accurate upwind differencing for the convective terms [105]. A discrete pressure-Poisson equation, designed to avoid the odd-even decoupling inherent in the case of non-staggered grids, is used to enforce the incompressibility constraint [106].

The discrete momentum equations are integrated in time using a four-stage explicit Runge-Kutta scheme. The pressure-velocity equation is solved using the alternate-direction-implicit (ADI) approximate factorization method

to accelerate its convergence, and the Thomas algorithm. The pressure-Poisson equation is transformed into a diffusion-like evolution equation. Convergence acceleration techniques, such as local time stepping and implicit residual smoothing, are used to enhance the error damping properties of the time marching procedure. The turbulence transport equations are discretized in space and integrated in time following a similar procedure to that indicated earlier for the momentum equations for the mean flow. A four-stage Runge-Kutta method is also used to advance the discrete equations in time.

In the following sections, the governing equations in generalized curvilinear coordinates, the spatial and temporal discretization of the governing equations, pressure-velocity coupling algorithm, solutions of the turbulence transport equations, and convergence acceleration techniques are described in turn.

Governing equations

The incompressible time-averaged VANS equations with constant porosity, Eqs. (2.19) and (2.27), are transformed to generalized curvilinear coordinates by invoking the partial transformation, i.e., $x_i \rightarrow \xi^i$, but leaving the mean velocity components $\langle \overline{u}_i \rangle$ in Cartesian coordinates. The transformed governing equations,

nondimensionalized by the fluid density ρ, reference velocity U_R, and reference length L_R, read as follows:

Continuity equation

$$J \frac{\partial}{\partial \xi^i} \left(\frac{1}{J} V^i \right) = 0 \tag{3.1}$$

Momentum equations

$$\frac{\partial \langle \overline{u}_i \rangle}{\partial t} + \frac{1}{\varepsilon_\beta} V^k \frac{\partial \langle \overline{u}_i \rangle}{\partial \xi^k} = - \xi^k_{x_i} \frac{\partial \langle \overline{P} \rangle}{\partial \xi^k} + J \frac{\partial}{\partial \xi^m} \left(\frac{1}{Re} \frac{g^{mn}}{J} \frac{\partial \langle \overline{u}_i \rangle}{\partial \xi^n} \right) - J \frac{\partial}{\partial \xi^m} \left(\frac{1}{J} \xi^m_{x_j} \langle \overline{u_i' u_j'} \rangle \right) + \varepsilon_\beta \overline{f_i} \tag{3.2}$$

$$\overline{f_i} = - \frac{1}{Re \cdot Da} \cdot \langle \overline{u}_i \rangle \tag{3.2a}$$

where Re and Da denote the Reynolds number ($Re = U_R L_R / \nu$) and the Darcy number ($Da = K / L_R^2$), respectively. J, the Jacobian of the geometric transformation, and g^{mn}, the contravariant metric tensor of the geometric transformation, are defined as

$$J = det \begin{vmatrix} \xi^1_{x_1} & \xi^1_{x_2} & \xi^1_{x_3} \\ \xi^2_{x_1} & \xi^2_{x_2} & \xi^2_{x_3} \\ \xi^3_{x_1} & \xi^3_{x_2} & \xi^3_{x_3} \end{vmatrix} = det \begin{vmatrix} x_{1_{\xi^1}} & x_{1_{\xi^2}} & x_{1_{\xi^3}} \\ x_{2_{\xi^1}} & x_{2_{\xi^2}} & x_{2_{\xi^3}} \\ x_{3_{\xi^1}} & x_{3_{\xi^2}} & x_{3_{\xi^3}} \end{vmatrix}^{-1} \tag{3.3a}$$

$$g^{mn} = \xi^m_{x_i}\xi^n_{x_i} \tag{3.3b}$$

$$\xi^k_{x_i} = \frac{\partial \xi^k}{\partial x_i} \tag{3.3c}$$

$$x_{i_{\xi^k}} = \frac{\partial x_i}{\partial \xi^k} \tag{3.3d}$$

V^k are the contravariant components of the mean Cartesian velocity components $\langle \overline{u}_i \rangle$, defined as

$$V^k = \langle \overline{u}_j \rangle \xi^k_{x_j} \tag{3.4}$$

Second-order turbulence closure

The second-order turbulence transport equations, Eqs. (2.31)-(2.39), are transformed to generalized curvilinear coordinates as follows

$$\frac{\partial \langle \overline{u_i' u_j'} \rangle}{\partial t} + \frac{1}{\varepsilon_\beta} V^k \frac{\partial \langle \overline{u_i' u_j'} \rangle}{\partial \xi^k} = G_{ij} + \phi_{ij} - \varepsilon_{ij} + d_{ij} + J \frac{\partial}{\partial \xi^m} \left(\frac{1}{Re} \frac{g^{mn}}{J} \frac{\partial \langle \overline{u_i' u_j'} \rangle}{\partial \xi^n} \right) - F_{ij} \tag{3.5}$$

$$G_{ij} = -\frac{1}{\varepsilon_\beta} \left(\langle \overline{u_i' u_k'} \rangle \xi^m_{x_k} \frac{\partial \langle \overline{u}_j \rangle}{\partial \xi^m} + \langle \overline{u_j' u_k'} \rangle \xi^m_{x_k} \frac{\partial \langle \overline{u}_i \rangle}{\partial \xi^m} \right) \tag{3.5a}$$

$$\phi_{ij} = \phi_{ij1} + \phi_{ij2} + \phi^{w}_{ij1} + \phi^{w}_{ij2} \tag{3.5b}$$

$$\varepsilon_{ij} = \frac{2}{3}\delta_{ij}\varepsilon \tag{3.5c}$$

$$d_{ij} = J\frac{\partial}{\partial\xi^{m}}\left(\frac{1}{J}c_{s}\frac{k}{\varepsilon}\xi^{m}_{x_k}\langle\overline{u_k'u_l'}\rangle\xi^{n}_{x_l}\frac{\partial\langle\overline{u_i'u_j'}\rangle}{\partial\xi^{n}}\right) \tag{3.5d}$$

$$F_{ij} = \frac{\delta_{ij}}{3}\overline{f}_{k}\langle\overline{u}_{k}\rangle \tag{3.5e}$$

$$\begin{aligned}\frac{\partial\varepsilon}{\partial t} + \frac{1}{\varepsilon_{\beta}}V^{k}\frac{\partial\varepsilon}{\partial\xi^{k}} &= J\frac{\partial}{\partial\xi^{m}}\left[\left(\frac{1}{J}c_{\varepsilon}\frac{k}{\varepsilon}\xi^{m}_{x_k}\langle\overline{u_k'u_l'}\rangle\xi^{n}_{x_l} + \frac{1}{Re}\frac{g^{mn}}{J}\right)\frac{\partial\varepsilon}{\partial\xi^{n}}\right] \\ &\quad + \left(c_{\varepsilon 1} + \psi_1 + \psi_2\right)\left(\varepsilon/k\right)G - c_{\varepsilon 2}\left(\varepsilon\tilde{\varepsilon}/k\right) \\ &\quad - c_{\varepsilon_3}\frac{\varepsilon}{k}F_{ii}\end{aligned} \tag{3.6}$$

$$\psi_1 = 2.5A\left(G/\varepsilon - 1\right) \tag{3.6a}$$

$$\psi_2 = 0.3\left(1 - 0.3A_2\right)\exp\left[-\left(0.002R_t\right)^2\right] \tag{3.6b}$$

$$\tilde{\varepsilon} = \varepsilon - \frac{2}{Re}\left(\xi^{m}_{x_2}\frac{\partial k^{\frac{1}{2}}}{\partial\xi^{m}}\right)^{2} \tag{3.6c}$$

Two-equation turbulence closure

The two-equation turbulence transport equations, Eqs. (2.40)-(2.48), are transformed to generalized

curvilinear coordinates as follows

$$\frac{\partial k}{\partial t} + \frac{1}{\varepsilon_\beta} V^j \frac{\partial k}{\partial \xi^j} = J \frac{\partial}{\partial \xi^m}\left[\left(\frac{1}{Re} + \frac{\nu_{t_{eff}}}{\sigma_k}\right) \frac{g^{mn}}{J} \frac{\partial k}{\partial \xi^n}\right] + G - \varepsilon - D - \overline{f}_i \langle \overline{u}_i \rangle \tag{3.7}$$

$$\nu_{t_{eff}} = \frac{\nu_t}{\varepsilon_\beta} = \frac{1}{\varepsilon_\beta} C_\mu f_\mu \frac{k^2}{\varepsilon} \tag{3.7a}$$

$$f_\mu = exp\left[-\, 3.4/\left(1 + R_t/50\right)^2\right] \tag{3.7b}$$

$$G = \frac{1}{2} \nu_{t_{eff}} \left(\frac{\partial \langle \overline{u}_i \rangle}{\partial \xi^k} \xi^k_{x_j} + \frac{\partial \langle \overline{u}_j \rangle}{\partial \xi^k} \xi^k_{x_i} \right)^2 \tag{3.7c}$$

$$D = \frac{2}{Re} \left(\xi^k_{x_2} \frac{\partial \sqrt{k}}{\partial \xi^k} \right)^2 \tag{3.7d}$$

$$\frac{\partial \varepsilon}{\partial t} + \frac{1}{\varepsilon_\beta} V^j \frac{\partial \varepsilon}{\partial \xi^j} = J \frac{\partial}{\partial \xi^m}\left[\left(\frac{1}{Re} + \frac{\nu_{t_{eff}}}{\sigma_\varepsilon}\right) \frac{g^{mn}}{J} \frac{\partial \varepsilon}{\partial \xi^n}\right] + C_1 f_1 \frac{\varepsilon}{k} G - C_2 f_2 \frac{\varepsilon^2}{k} + E - C_3 \frac{\varepsilon}{k} \overline{f}_i \langle \overline{u}_i \rangle \tag{3.8}$$

$$E = \frac{2\nu_{t_{eff}}}{Re} \left[\xi^j_{x_2} \frac{\partial}{\partial \xi^j} \left(\xi^k_{x_2} \frac{\partial \langle \overline{u}_2 \rangle}{\partial \xi^k} \right) \right]^2 \tag{3.8a}$$

$$f_1 = 1 \tag{3.8b}$$

$$f_2 = 1 - 0.3\, exp\left(-\, R_t^{\,2}\right) \tag{3.8c}$$

Spatial discretization of continuity and momentum equations

An implicit finite difference method is employed to solve the three-dimensional governing equations in the generalized curvilinear coordinates. The momentum equations, Eq. (3.2), are discretized in space, on a non-staggered mesh, using second-order finite difference scheme for the pressure gradient, viscous diffusion, and the Reynolds stress terms, and second-order upwind finite differencing for the convective terms. The drag force terms are computed at the mesh points (i,j,k). The upwind differencing of the convective terms eliminates the need for adding artificial dissipation terms, to the right hand side of the momentum equations, to stabilize the numerical algorithm. This is due to the fact that a fixed amount of dissipation is inherent in the upwind differencing.

The finite difference schemes employed for the pressure gradient, where pressure located on mesh points (i,j,k), and viscous diffusion, which calculating velocity components on half mesh points, and the Reynolds stress terms are two-point central finite differencing, and for the convective terms are three-point one-sided finite differencing.

For clarity, we only represent discrete approximations of convective terms, pressure gradient,

viscous diffusion, the Reynolds stress, and drag force terms for all indices with values of 1 in Eq. (3.2). All remaining terms are discretized in a similar fashion.

convective terms:

$$CT\left(\langle \overline{u}_i \rangle\right) = \frac{1}{\varepsilon_\beta} V^m \frac{\partial \langle \overline{u}_i \rangle}{\partial \xi^m} \tag{3.9}$$

$$\frac{1}{\varepsilon_\beta} V^1 \frac{\partial \langle \overline{u}_1 \rangle}{\partial \xi^1} = \frac{1}{\varepsilon_\beta} V^{1+}_{i,j,k} \delta^-_{\xi^1}\left(\langle \overline{u}_1 \rangle\right)_{i,j,k} + \frac{1}{\varepsilon_\beta} V^{1-}_{i,j,k} \delta^+_{\xi^1}\left(\langle \overline{u}_1 \rangle\right)_{i,j,k} \tag{3.10}$$

where

$$V^{i\pm}_{i,j,k} = \frac{1}{2}\left(V^i_{i,j,k} \pm \left|V^i_{i,j,k}\right|\right) \tag{3.11}$$

$$\delta^\pm_{\xi^1}\left(\ \right)_{i,j,k} = \pm \frac{1}{2\Delta\xi^1}\left[-3\left(\ \right)_{i,j,k} + 4\left(\ \right)_{i\pm1,j,k} - \left(\ \right)_{i\pm2,j,k}\right] \tag{3.12}$$

pressure gradient terms:

$$PG_i\left(\langle \overline{P} \rangle\right) = -\xi^m_{x_i} \frac{\partial \langle \overline{P} \rangle}{\partial \xi^m} \tag{3.13}$$

$$-\xi^1_{x_1} \frac{\partial \langle \overline{P} \rangle}{\partial \xi^1} = -\left(\frac{\partial \xi^1}{\partial x_1}\right)_{i,j,k} \delta\xi^1\left(\langle \overline{P} \rangle\right)_{i,j,k} \tag{3.14}$$

where

$$\delta_{\xi^1}( )_{i,j,k} = \frac{1}{2\Delta\xi^1}\left[( )_{i+1,j,k} - ( )_{i-1,j,k}\right] \tag{3.15}$$

viscous diffusion terms:

$$VD\left(\langle\overline{u}_i\rangle\right) = J\,\frac{\partial}{\partial\xi^m}\left(\frac{1}{Re}\,\frac{g^{mn}}{J}\,\frac{\partial\langle\overline{u}_i\rangle}{\partial\xi^n}\right) \tag{3.16}$$

$$J\,\frac{\partial}{\partial\xi^1}\left(\frac{1}{Re}\,\frac{g^{11}}{J}\,\frac{\partial\langle\overline{u}_1\rangle}{\partial\xi^1}\right) = \tilde{\delta}_{\xi^1}\left(\frac{1}{Re}\,\frac{1}{J}\,\frac{\partial\xi^1}{\partial x_1}\,\frac{\partial\xi^1}{\partial x_1}\,\tilde{\delta}_{\xi^1}\left(\langle\overline{u}_1\rangle\right)_{i,j,k}\right)_{i,j,k} \tag{3.17}$$

where

$$\tilde{\delta}_{\xi^1}( )_{i,j,k} = \frac{1}{\Delta\xi^1}\left[( )_{i+\frac{1}{2},j,k} - ( )_{i-\frac{1}{2},j,k}\right] \tag{3.18}$$

Reynolds stress terms:

$$RS\left(\langle\overline{u_i'u_j'}\rangle\right) = -J\,\frac{\partial}{\partial\xi^m}\left(\frac{1}{J}\,\xi^m_{x_j}\langle\overline{u_i'u_j'}\rangle\right) \tag{3.19}$$

$$-J\,\frac{\partial}{\partial\xi^1}\left(\frac{1}{J}\,\xi^1_{x_j}\langle\overline{u_1'u_1'}\rangle\right) = -J\delta_{\xi^1}\left(\frac{1}{J}\,\frac{\partial\xi^1}{\partial x_1}\,\langle\overline{u_1'u_1'}\rangle\right)_{i,j,k} \tag{3.20}$$

drag force terms

$$DF\left(\langle\overline{u}_i\rangle\right) = \varepsilon_\beta\overline{f_i} = -\varepsilon_\beta\,\frac{1}{Re\cdot Da}\cdot\langle\overline{u}_i\rangle \tag{3.21}$$

$$\varepsilon_\beta \overline{f_1} = \varepsilon_\beta \left(- \frac{1}{Re \cdot Da} \cdot \langle \overline{u}_1 \rangle \right)_{i,j,k} \tag{3.22}$$

In all the above equations, the metrics and the Jacobian of the geometric transformation are computed at the mesh points (i,j,k) using two-point central differencing. To compute the metrics and the Jacobian at the half nodes, where they are needed for the discretization of the viscous diffusion terms, a simple averaging procedure is employed.

The continuity equation, Eq. (3.1), is discretized using two-point central differencing. For convenience we defined the discrete divergence operator as follows:

$$DIV(Q_{i,j,k}) = J \left[\delta_{\xi^q} \left(\frac{1}{J} V^q \right)_{i,j,k} \right] \tag{3.23}$$

where $Q = \langle \overline{u}_i \rangle$ is the cartesian velocity components.

Temporal discretization of continuity and momentum equations

The system of the discrete continuity and momentum equations is integrated in time using the explicit four-stage Runge-Kutta scheme [105]. The Runge-Kutta scheme is applied to the system of the governing equations, Eqs. (3.1) and (3.2), as follows (for ℓ = 1, 2, 3, and 4):

$$DIV\left(Q^{\ell}_{i,j,k}\right) = 0 \tag{3.24}$$

$$Q^{\ell}_{i,j,k} = Q^{n}_{i,j,k} - \alpha_{\ell}\Delta t_{i,j,k} RHS^{\ell-1}_{i,j,k} \tag{3.25}$$

$$RHS = CT\left(\langle\overline{u}_i\rangle\right) - VD\left(\langle\overline{u}_i\rangle\right) - PG_i\left(\langle\overline{P}\rangle\right) - RS\left(\langle\overline{u'_i u'_j}\rangle\right) - DF\left(\langle\overline{u}_i\rangle\right) \tag{3.26}$$

In the above equations, the superscript "n" denotes the time step at which the solution is known, while the superscript "ℓ" denotes an intermediate time stage used to advance the solution from time step "n" to next time step "n+1". For example, $Q^{\ell} = Q^{n}$ if $\ell = 0$, and $Q^{n+1} = Q^{\ell}$ when $\ell = 4$. For the explicit four-stage Runge-Kutta scheme, the coefficients of α_{ℓ} are 1/4, 1/3, 1/2 and 1 for $\ell = 1, 2, 3,$ and 4, in sequence. $\Delta t_{i,j,k}$ in Eq. (3.25) is the time increment which, for reasons discuss later on, varies in space (local time stepping). For the sake of convenience, however, in the rest of the analysis the subscript (i,j,k) has been dropped.

Pressure-velocity coupling algorithm

The system of discrete governing equations, Eq. (3.24) and (3.25), can not be integrated in time in their current forms due to the lack of an evolution equation for the pressure field. The discrete momentum equation, Eq. (3.25), however, can be substituted in the discrete

continuity equation, Eq. (3.24), to obtain a Poisson equation for the pressure field at the intermediate stage ℓ-1. However, on a non-staggered mesh, it would yield oscillatory solutions for the pressure field (odd-even decoupling). To overcome this difficulty, it was proposed by Sotiropoulos and Abdallah [106] to derive the discrete pressure equation starting from a modified form of the discrete continuity equation. The discrete continuity equation reads as follows:

$$DIV\left(Q^{\ell}\right) = \gamma J\left(\tilde{L} - L\right)\left(\langle \overline{P} \rangle^{\ell-1}\right) \tag{3.27}$$

where

$$\tilde{L}(\,) = \left[\tilde{\delta}_{\xi^1}\left(\frac{g^{11}}{J}\Delta t\tilde{\delta}_{\xi^1}\right) + \tilde{\delta}_{\xi^2}\left(\frac{g^{22}}{J}\Delta t\tilde{\delta}_{\xi^2}\right) + \tilde{\delta}_{\xi^3}\left(\frac{g^{33}}{J}\Delta t\tilde{\delta}_{\xi^3}\right)\right](\,) \tag{3.28}$$

$$L(\,) = \left[\delta_{\xi^1}\left(\frac{g^{11}}{J}\Delta t\delta_{\xi^1}\right) + \delta_{\xi^2}\left(\frac{g^{22}}{J}\Delta t\delta_{\xi^2}\right) + \delta_{\xi^3}\left(\frac{g^{33}}{J}\Delta t\delta_{\xi^3}\right)\right](\,) \tag{3.29}$$

It should be noted that the source term in the right-hand-side of Eq. (3.27) is necessary to guarantee the smoothness of the computed pressure field [106], and γ is a positive constant used to control the size of the source term.

To derive to discrete pressure equation at the "ℓ"

level by inserting Eq. (3.25) into Eq. (3.24), we have

$$DIV\left[\Delta t \cdot PG_i\left(\langle \overline{P} \rangle^{\ell-1}\right)\right] = \frac{1}{\alpha_\ell} DIV\left(Q^\ell\right) - \sigma^{\ell-1} \qquad (3.30)$$

$$\sigma^{\ell-1} = DIV\left(\Delta t \cdot RHS^{\ell-1}\right) - DIV\left[\Delta t \cdot PG_i\left(\langle \overline{P} \rangle^{\ell-1}\right)\right] \qquad (3.31)$$

The left-hand-side of Eq. (3.30) can be decomposed into two components,

$$DIV\left[\Delta t \cdot PG_i\left(\langle \overline{P} \rangle^{\ell-1}\right)\right] = J\left[L\left(\langle \overline{P} \rangle^{\ell-1}\right) + N\left(\langle \overline{P} \rangle^{\ell-1}\right)\right] \qquad (3.32)$$

where

$$N(\,) = \left\{\delta_{\xi^1}\left[\frac{\Delta t}{J}\left(g^{12}\delta_{\xi^2} + g^{13}\delta_{\xi^3}\right)\right] + \delta_{\xi^2}\left[\frac{\Delta t}{J}\left(g^{12}\delta_{\xi^1} + g^{23}\delta_{\xi^3}\right)\right] + \delta_{\xi^3}\left[\frac{\Delta t}{J}\left(g^{13}\delta_{\xi^1} + g^{23}\delta_{\xi^2}\right)\right]\right\}(\,) \qquad (3.33)$$

By incorporating the discrete momentum equation, Eq. (3.30), into the discrete continuity equation, Eq. (3.27), the discrete pressure equation has the following form,

$$J\left[(1-\gamma)L\left(\langle \overline{P} \rangle^{\ell-1}\right) + \gamma\tilde{L}\left(\langle \overline{P} \rangle^{\ell-1}\right) + N\left(\langle \overline{P} \rangle^{\ell-1}\right)\right] = \frac{1}{\alpha_\ell} DIV\left(Q^\ell\right) - \sigma^{\ell-1} \qquad (3.34)$$

The positive constant γ is introduced to control the size

of the source term and minimize the error in the satisfaction of the discrete continuity equation. The values of γ between 0.01 and 0.1 are sufficient to eliminate the odd-even decoupling for the pressure field [106].

In order to accelerate the convergence of the pressure equation as well as that of the global time marching procedure, Eq. (3.34) is solved using the ADI method. For that reason, a time derivative of the pressure is introduced in Eq. (3.34) transforming the pressure-Poisson equation into a diffusion-like evolution equation:

$$-\varpi \frac{\partial \langle \overline{P} \rangle}{\partial t} + J\left[(1-\gamma)L\left(\langle \overline{P} \rangle^{\ell-1}\right) + \gamma \tilde{L}\left(\langle \overline{P} \rangle^{\ell-1}\right) + N\left(\langle \overline{P} \rangle^{\ell-1}\right)\right] = \frac{1}{\alpha_\ell} DIV\left(Q^\ell\right) - \sigma^{\ell-1} \tag{3.35}$$

where ϖ is a positive preconditioning constant introduced to accelerate the convergence to steady state as discussed in a later paragraph. Incorporating the first-order accurate Euler implicit temporal linearization scheme, we have

$$\langle \overline{P} \rangle^{\ell-1} = \langle \overline{P} \rangle^{\ell-2} + \Delta \langle \overline{P} \rangle \tag{3.36}$$

Substituting Eq. (3.36) into Eq. (3.35), we can obtain

$$\Delta\langle\overline{P}\rangle - \frac{\Delta t}{\varpi}\gamma J\tilde{L}\left(\Delta\langle\overline{P}\rangle\right) = -\frac{\Delta t}{\varpi} PRHS \qquad (3.37)$$

where

$$PRHS = \gamma J\left[L\left(\langle\overline{P}\rangle^{\ell-1}\right) - \tilde{L}\left(\langle\overline{P}\rangle^{\ell-2}\right)\right] + DIV\left(\frac{Q^{\ell}}{\alpha_{\ell}} - \Delta t \cdot RHS^{\ell-1}\right) \qquad (3.38)$$

Sotiropoulos and Abdallah [105] suggested to update the pressure in the first term of the right-hand-side of Eq. (3.38) only at the first stage of the four-stage Runge-Kutta scheme in order to save computational effort and time. Therefore, the pressure at time step "*n*" is used to calculate the first term of the right-hand-side of Eq. (3.38) in the four-stage Runge-Kutta scheme for the next time step "*n*+1" solutions. Application of the ADI approximate factorization method to Eq. (3.37) gives:

$$\left\{\left[1 - \frac{\Delta t}{\varpi} J\tilde{\delta}_{\xi^1}\left(\frac{g^{11}}{J}\Delta t\tilde{\delta}_{\xi^1}\right)\right]\left[1 - \frac{\Delta t}{\varpi} J\tilde{\delta}_{\xi^2}\left(\frac{g^{22}}{J}\Delta t\tilde{\delta}_{\xi^2}\right)\right]\left[1 - \frac{\Delta t}{\varpi} J\tilde{\delta}_{\xi^3}\left(\frac{g^{33}}{J}\Delta t\tilde{\delta}_{\xi^3}\right)\right]\right\}\Delta\langle\overline{P}\rangle = -\frac{\Delta t}{\varpi} PRHS \qquad (3.39)$$

Equation (3.39) is solved, in three consecutive sweeps, using the Thomas algorithm. The Thomas algorithm can be vectorized by solving simultaneously for all the points

on a plane perpendicular to the current sweep direction. Values of the preconditioning constant ϖ of the order of 0.5 have been used in all the calculations reported in this study. This allows the pressure equation to operate with an effective time step one order of magnitude higher than the momentum equations, and results in significant convergence acceleration of the overall time marching procedure.

Solutions of the turbulence transport equations

The turbulence transport equations of a second-order closure, Eqs. (3.5) and (3.6), and a two-equation closure, Eqs. (3.7) and (3.8), are discretized in space, on a non-staggered mesh, and integrated in time following a similar procedure to that indicated earlier for the momentum equations for the mean flow. The convective terms are discretized using second-order upwind differencing, and the rest of the terms are using second-order accurate central finite differences. A four-stage Runge-Kutta method is also used to advance the discrete equations in time as follows,

$$Q_T^{\ell} = Q_T^n - \alpha_{\ell}\Delta t RHS_T^{\ell-1} \qquad (3.40)$$

Q_T represents turbulent quantities ($\langle\overline{u_i'u_j'}\rangle$, k, and ε) in turbulence transport equations, Eqs. (3.5)-(3.8). RHS_T

contains convective terms minus the sum of all the terms in the right-hand-side of turbulence transport equations, Eqs. (3.5)-(3.8), respectively.

Convergence acceleration techniques

The convergence rate of the time marching procedure is enhanced by employing the local time-stepping technique along with implicit residual smoothing. The time increment is computed and stored for every node as follows [107]:

$$\Delta t_{i,j,k} = min\left(\Delta t^m, \Delta t^v\right) \tag{3.41}$$

where

$$\Delta t^m = CFL \cdot min\left(\sqrt{g_{11}}, \sqrt{g_{22}}, \sqrt{g_{33}}\right) \tag{3.41a}$$

$$\Delta t^v = \frac{\Omega}{\left(\frac{1}{Re} + 0.09\,\frac{k^2}{\varepsilon}\right)\left(g_{11} + g_{22} + g_{33}\right)} \tag{3.41b}$$

$$g_{mn} = \frac{\partial x_k}{\partial \xi^m}\,\frac{\partial x_k}{\partial \xi^n} \tag{3.41c}$$

In the above equations, CFL and Ω denote the Courant-Friedrich-Lewis number (hyperbolic stability criterion) and the von Neumann number (parabolic stability

criterion), respectively. The *CFL* number, used herein, is an approximately constant, since it is based only on the local length scales of the computational grid. Although an exact *CFL* number should involve the local velocity scales as well, we chose to use this approximate formulation in order to avoid the calculation of Δt^m at every new iteration level. This purely geometric variation of Δt^m has been found adequate on highly stretched meshes [105]. Typically, the parabolic stability constraint dominates only in the near-wall region where the grid spacing, the velocity and the eddy viscosity approach zero. Sufficiently far from the wall, however, the hyperbolic stability criterion dictates the choice of a stable time increment. In the present calculations, the selection of the local time increment based on both the hyperbolic and parabolic stability criteria (Eq. (3.41)) was found necessary for stability only for Reynolds numbers of the order of 10^6 or greater. At lower Reynolds numbers, the hyperbolic stability criterion was sufficient for obtaining converged solutions.

Jameson [108] adopted the implicit residual smoothing scheme [109] to accelerate the convergence of the four-stage Runge-Kutta scheme. In the present study, the implicit residual smoothing is only applied to the right-hand-side of the discrete momentum equations, Eq.

(3.25), and the residual calculated in Eq. (3.26) is smoothed by the constant coefficient implicit operator to define a new residual:

$$\left(1 - \omega_1 \delta_{\xi^1 \xi^1}\right)\left(1 - \omega_2 \delta_{\xi^2 \xi^2}\right)\left(1 - \omega_3 \delta_{\xi^3 \xi^3}\right)\overline{RHS}^{\ell} = RHS^{\ell} \qquad (3.42)$$

where

$$\delta_{\xi^m \xi^n}( )_{i,j,k} = \frac{( )_{i+1,j,k} - 2( )_{i,j,k} + ( )_{i-1,j,k}}{\Delta\xi^m \Delta\xi^n} \qquad (3.43)$$

The constants ω_1, ω_2, and ω_3 are smoothing parameters with the order of one and the values can be chosen differently for each spatial direction. Equation (3.42) is solved using the Thomas algorithm and the smoothed residual, $\overline{RHS}^{\ell}$, replaces the residual, RHS^{ℓ}, in Eq. (3.25). The residual smoothing is applied at every stage of the Runge-Kutta scheme. The implementation of the implicit residual smoothing in the four-stage Runge-Kutta procedure allows the use of higher *CFL* numbers and consequently leads to a significant acceleration of the convergence rate [105].

The smoothing coefficients in Eq. (3.42) are constant in each spatial direction and, therefore, one can expect this formulation to be optimal for grids that are not highly stretched. For further acceleration of the

convergence rate, Martinelli [110] proposed a formulation for the two-dimensional compressible Navier-Stokes equations where the smoothing coefficients in Eq. (3.42) are functions of characteristic wave speed. The idea behind Martinelli's suggestion is that, since the minimum local grid spacing dictates the maximum allowable local time step for stable calculations, more smoothing should be applied in the direction of that minimum spacing. If the same smoothing is applied in the other spatial directions—where the grid spacing is coarser and the time step, as computed by Eq. (3.42), is much smaller than the local stability limit—the damping properties of the scheme are impaired. Martinelli's formulation was extended to three-dimensions by Radiespiel et al. [110] and Liu and Jameson [111]. In the present study a formulation similar to that of Liu and Jameson is adopted as follows:

$$\omega_1 = max\left\{0, \frac{1}{4}\left[\left(\frac{CFL}{CFL^*}\frac{1}{1 + r_{12} + r_{13}}\right)^2 - 1\right]\right\} \qquad (3.44a)$$

$$\omega_2 = max\left\{0, \frac{1}{4}\left[\left(\frac{CFL}{CFL^*}\frac{1}{1 + r_{21} + r_{23}}\right)^2 - 1\right]\right\} \qquad (3.44b)$$

$$\omega_3 = max\left\{0, \frac{1}{4}\left[\left(\frac{CFL}{CFL^*}\frac{1}{1 + r_{31} + r_{32}}\right)^2 - 1\right]\right\} \qquad (3.44c)$$

$$r_{i,j} = \sqrt{\frac{g_{ii}}{g_{jj}}} \tag{3.44d}$$

In the above equations, *CFL** denotes the *CFL* number of the unsmoothed scheme while *CFL* denotes the desirable *CFL* number. It can be easily seen that, for non-equal grid spacing, larger smoothing will be applied in the direction of smaller spacing, while for uniform grid the three smoothing coefficients are equal. In addition, these equations involve only geometric quantities and, consequently, the smoothing coefficients need to be computed only once at the beginning of the calculation.

Summary of numerical algorithm

We can now summarize the solution procedure.

Step 1. Read/generate mesh.

Step 2. Calculate metrics using Eq. (3.3), and time step using Eq. (3.41).

Step 3. Initialize flow variables.

Step 4. Calculate the artificial mass source term for the pressure equation (the first term in the right-hand-side of Eq. (3.38)) using the currently known pressure field. To save computational effort and time, the artificial mass source term is frozen in all subsequent Runge-Kutta stages.

Step 5. Advance in time using four-Stage Runge-Kutta scheme for ℓ = 1 to 4:

(a). Solve the turbulence transport equations using Eq. (3.40).

(b). Solve the discreted momentum equation, Eq. (3.25), and compute the right-hand-side of the pressure equation as given by Eq. (3.38).

(c). Solve the pressure equation, Eq. (3.39), to obtain the pressure field at the ℓ-1 stage. Since, the steady state solution is of interest, only one ADI iteration is performed on the pressure.

(d). Compute the velocity field at the ℓ stage using Eq. (3.25) and return to step (a).

Step 6. Update solutions from time step n to n+1.

Step 7. Repeat step 4 to 6 until convergence is reached.

CHAPTER IV

ASSESSMENT OF TWO LOW-REYNOLDS-NUMBER $k - \varepsilon$ MODELS IN TURBULENT BOUNDARY LAYERS WITH SURFACE ROUGHNESS

The low-Reynolds-number $k - \varepsilon$ models of Zhang et al. [66] and Foti and Scandura [67] are applied in this chapter. The roughness modeling terms in both models involve only the equivalent sand roughness and contain no model coefficients that depend on the roughness geometry. The model of Zhang et al. [66] has been shown to predict well the rough wall log-law mean velocity profiles and the wall shear stress in rough pipes and channels. However, results for turbulence properties have not been reported and the model has not been applied to turbulent boundary layer flows over rough plates. The model of Foti and Scandura [67] has been validated for oscillatory flows over a wavy sea bed. Their model has not been applied to other types of rough surfaces.

In this paper, the two roughness models are applied to turbulent flows in rough circular pipes, in rough rectangular channels, and over rough flat plates. The results of these calculations, and their comparisons with the corresponding measured data, are presented and discussed. We focus on the k-type surface roughness since

both models have been calibrated with measurements for k-type surface roughness. The performance of these two models is first evaluated by calculating the turbulent flows in these geometries with smooth walls and comparing the results with the corresponding measurements and DNS data [113-115]. The fully developed turbulent rough pipe and rough channel flows are then calculated, and the numerical results are compared with the experimental data. For the turbulent boundary layers over flat plates, different types of surface roughness, including uniform spheres [17], sandpaper [18], and mesh screen [13,18], are numerically studied and the results compared with the corresponding experimental data.

In the following sections, the details of turbulence models and numerical methods used in this chapter are presented. These are followed by a Results and discussion section, where the simulation results obtained are presented, compared, and discussed.

Turbulence models

The nondimensional, incompressible forms of the transport equations for k and ε for the two low-Reynolds-number $k-\varepsilon$ models studied can be written in a generalized curvilinear coordinates system as follows:

$$\frac{\partial k}{\partial t} + V^j \frac{\partial k}{\partial \xi^j} = J \frac{\partial}{\partial \xi^j} \left\{ \left(\frac{1}{Re} + \frac{\nu_t}{\sigma_k} \right) \frac{g^{jp}}{J} \frac{\partial k}{\partial \xi^p} \right\} + G - \varepsilon \quad (4.1)$$

$$\frac{\partial \varepsilon}{\partial t} + V^j \frac{\partial \varepsilon}{\partial \xi^j} = J \frac{\partial}{\partial \xi^j} \left\{ \left(\frac{1}{Re} + \frac{\nu_t}{\sigma_\varepsilon} \right) \frac{g^{jp}}{J} \frac{\partial \varepsilon}{\partial \xi^p} \right\} + C_1 f_1 \frac{\varepsilon}{k} G - C_2 f_2 \frac{\varepsilon^2}{k} \quad (4.2)$$

$$\nu_t = C_\mu f_\mu \frac{k^2}{\varepsilon} \quad (4.3)$$

V^j are the contravariant components of the mean Cartesian velocity components $\overline{u}_k$, defined as

$$V^j = \overline{u}_k \xi^j_{x_k} \quad (4.4)$$

The first terms on the right-hand-side of Eq. (4.1) and Eq. (4.2) are the diffusion terms, while the last two terms represent production and dissipation terms. The production term G can be expressed as follows:

$$G = \frac{1}{2} \nu_t \left(\frac{\partial \overline{u}_i}{\partial \xi^k} \xi^k_{x_j} + \frac{\partial \overline{u}_j}{\partial \xi^k} \xi^k_{x_i} \right)^2 \quad (4.5)$$

σ_k, σ_ε, C_1, C_2, and C_μ are model constants. For both models, the values of these model constants are the same as those used in the standard k-ε model. That is, σ_k = 1.0, σ_ε = 1.3, C_1 = 1.44, C_2 = 1.92, and C_μ = 0.09.

The difference between the two models appears mainly in the form of the damping functions. The damping functions f_μ, f_1, and f_2 proposed by Zhang et al. [66] are described as follows:

$$f_\mu = 1 - exp\left[-\left(y^+ / 42\right)^2\right] + f_{\mu,s} \tag{4.6}$$

$$f_{\mu,s} = g_1\left(k_{eq}^+\right) exp\left(-25y^+ / k_{eq}^+\right) \tag{4.7}$$

$$f_1 = 1 + g_2\left(k_{eq}^+\right)\left[9.2 / \left(1 + y^+\right)\right]^6 \tag{4.8}$$

$$f_2 = 1 - exp\left(-R_t^2\right) \tag{4.9}$$

For smooth wall, $g_1(k_{eq}^+) = 0$, and $g_2(k_{eq}^+) = 1$. For rough wall, the extent of the viscous region is reduced due to the enhanced turbulent mixing. This roughness effect is achieved in Zhang et al. [66] by including an additional term $f_{\mu,s}$ to the formulation of the model damping function f_μ with a positive-definite roughness modeling function $g_1(k_{eq}^+)$. It was also argued that the value of f_1 for rough wall modeling should be lower than that used for smooth wall modeling in the near wall region due to the reduced production of the rate of dissipation ε. Therefore, a second roughness modeling function $g_2(k_{eq}^+)$ is used. $g_2(k_{eq}^+) = 1$ for smooth wall ($k_{eq}^+ = 0$) and decreases with increasing k_{eq}^+. The expressions of the roughness modeling

functions are

$$g_1\left(k_{eq}^{+}\right) = \sqrt{k_{eq}^{+} / 200} \tag{4.10}$$

$$g_2\left(k_{eq}^{+}\right) = exp\left[-1 / \left(0.1 + 1 / k_{eq}^{+}\right)\right] \tag{4.11}$$

For the low-Reynolds-number k-ε model of Foti and Scandura [67], the damping functions have the following forms,

$$f_\mu = \left[1 - exp\left(-0.0160 R_k\right)\right]^2 \left(1 + 20.5 / R_t\right) + f_{\mu,s} \tag{4.12}$$

$$f_{\mu,s} = S\left\{1.0 - tanh\left[0.15\left(y^{+} - 5.0S\right) / S\right]\right\} \tag{4.13}$$

$$f_1 = 1 + \left(0.05 / f_\mu\right)^3 \tag{4.14}$$

$$f_2 = 1 - exp\left(-R_t^2\right) / \left(1 + 0.01 k_{eq}^{+}\right) \tag{4.15}$$

where $R_k = k^{1/2} y / \nu$, and S is a function of the equivalent sand roughness k_{eq}^{+}. The value of S is determined through a calibration with experimental data [116]. Similar to the model of Zhang et al. [66], the modification to damping function f_μ is to obtain the effect of increased turbulent mixing near the rough wall. The damping function f_2 is modified to further decrease the sink terms in the dissipation rate equation.

In general, both of the models studied here adapt the forms of the damping functions found in existing low-Reynolds-number $k-\varepsilon$ models developed for smooth wall by including roughness correction functions. The roughness effects are modeled through the use of the equivalent sand roughness k_{eq}^{+} and are not shape-dependent. For the cases here, the equivalent sand roughness are provided by their corresponding experimental studies.

Numerical details

The three-dimensional incompressible dimensionless RANS equations in the generalized curvilinear coordinates are discretized in space, on a non-staggered mesh using second-order finite difference approximations, and advanced in time using a four-stage Runge-Kutta scheme following a similar procedure described in Chapter III.

The *CFL* number used in these computations is 1.5 for the k and ε equations. For all the results shown here, the residuals defined by the summation of differences between the current and the previous iterations were reduced by at least four orders of magnitude.

Computational domains

In this study, the axisymmetric solutions for pipe flows and two-dimensional solutions for channels and flat plates are sought. The computational domain for the fully

developed turbulent smooth and rough pipe flows extends 150 pipe diameters downstream and only a quarter of the pipe was simulated. For the fully developed turbulent smooth and rough channel flows, the domain extends 150 channel heights downstream and only a half of the channel was simulated. For the turbulent boundary layers over smooth and rough plates, the value of y^+ for the first grid point away from the wall is less than 0.1 and a hyperbolic tangent stretching function has been used in the wall-normal direction with grid clustered in the near wall region.

Boundary conditions

The boundary conditions were specified as follows. The inlet boundary conditions for the fully developed turbulent smooth pipe and smooth channel flows are assumed uniform for all variables, where $\overline{u} = 1$, $\overline{v} = 0$, $k = \varepsilon = 10^{-6}$. For the smooth flat plates, the Blasius solution has been used at the inlet with uniform profiles of $k = 0.013$ and $\varepsilon = 7$ [117]. The smooth wall solutions thus obtained are then used to initialize the corresponding rough wall calculations. On the symmetry boundaries, the mirror-image reflections for the grid and the flow variables are used for the fully developed turbulent smooth and rough pipe, and channel flows. For all cases, the exit boundary condition is imposed by

assuming zero streamwise diffusion. At the outer boundary of the flat plate, the turbulent boundary layer assumes the corresponding free stream conditions. The wall boundary condition is zero value for the three velocity components and the turbulent kinetic energy, while $\varepsilon = 1/Re(\partial^2 k/\partial y^2)$. However, the second-order derivative does not always guarantee positive value for the dissipation rate of turbulent kinetic energy at the wall. It has been proposed to employ $\varepsilon = 2/Re(k_1/y_1^2)$ as an approximation to the value of ε at the wall [118], where the subscript 1 denotes the nearest grid point from the wall.

Grid independence study

For the pipe flows, the numerical grid in the radial direction is generated by using a hyperbolic stretching function. The grid clusters near the inlet and is stretched using a hyperbolic stretching function toward the exit in the streamwise direction. A grid independence study for smooth pipe flow has been performed, and the results are shown in Figure 3. Figure 3 shows the calculated log-law velocity profiles by using both the model of Zhang et al. [66] (denoted as ZH) and the model of Foti and Scandura [67] (denoted as FS) with grids of 91×61, 55×61, and 55×81, in the streamwise and the wall-normal directions, respectively. The Reynolds number, based on the pipe diameter, is 40,000. The experimental

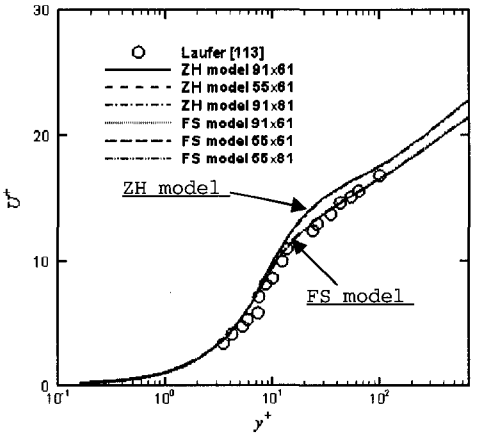

Figure 3. Grid independence study for flat plates with grid refinement in the streamwise direction.

data of Laufer [113] are also included for comparison. The computed profiles using the different grids basically collapse for both the ZH and the FS models, indicating the turbulent flow solutions being grid independent. The 55×61 grid is used in all the pipe flow solutions presented here. The same grid size is also found to provide grid independent solutions for channel flows.

For the flat plate boundary flows, Figure 4 shows the results of the grid independent study using both models with various grid numbers in the streamwise and wall-normal directions. The grid sizes vary widely between 71×150 and 281×150 (Figure 4(a)), and between 141×150 and 141×180 (Figure 4(b)). Figure 4(a) shows the surface skin friction distributions, which are known to

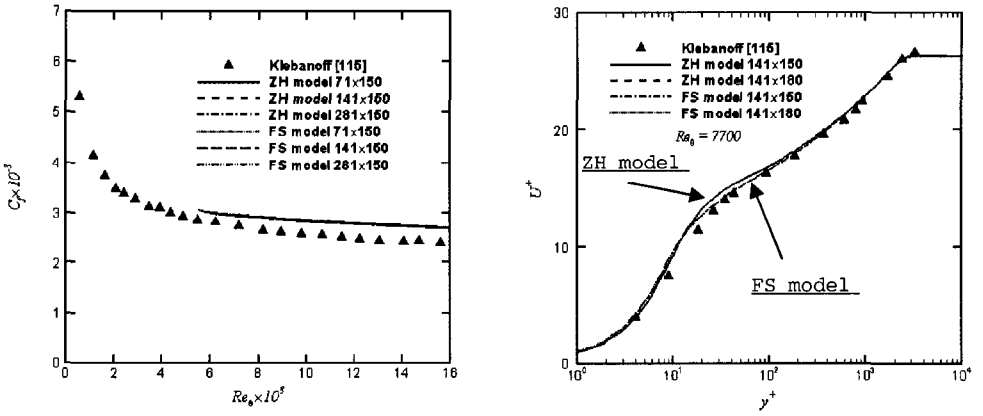

(a) (b)

Figure 4. Grid independence study for flat plates with grid refinement in the (a) streamwise direction; (b) wall-normal direction.

be sensitive to numerical grids, and Figure 4(b) shows the computed mean velocity profiles. The results show that, similar to what has been observed in the pipe flow grid independency study, the numerical code can achieve grid-independent solutions for the flat plate turbulent boundary layer. The turbulent flat plate boundary layer flow results presented have been obtained by using the 141×150 grid.

Results and discussion

The results of calculations are reported in three sections. The first part presents the results of the application of the two turbulence models to flows in smooth geometries, including pipes, channels, and flat

plates. The computational results are compared with measurements and DNS data. The second part compares the computational results for the fully developed rough pipe and rough channel flows with the corresponding experimental data. The last part presents numerical investigation of the turbulent boundary layers over flat plates with different types of surface roughness, including uniform spheres, sandpaper, and mesh. The computational results for the skin friction coefficients, the log-law velocity profiles, and the turbulence profiles are presented and compared with the available measurements.

Smooth pipe and channel flows, and flat plate turbulent boundary layers

The performance of the ZH and the FS models with zero roughness height was evaluated by simulating the fully developed turbulent flows in smooth pipes, in smooth channels, and over smooth flat plates. The FS model with zero roughness height degenerates to the low-Reynolds-number $k-\varepsilon$ model of Lam and Bremhorst [69], while the ZH model with zero roughness height does not reduce to any existing low-Reynolds-number $k-\varepsilon$ models. As shown previously in Figure 3, both models predict well the log-law mean velocity in the sublayer and outer layer comparing to experimental data [113]. The present ZH

model result has been verified with that in Zhang et al. [66] and both results show that the ZH model seems to overpredict in the buffer layer by a maximum of 8%, comparing with the measurements. Figure 5, which compares the computed and the measured turbulent kinetic energy profiles, shows that both models overpredict the peak of the turbulent kinetic energy near the wall, yet capture the trends of the experimental data.

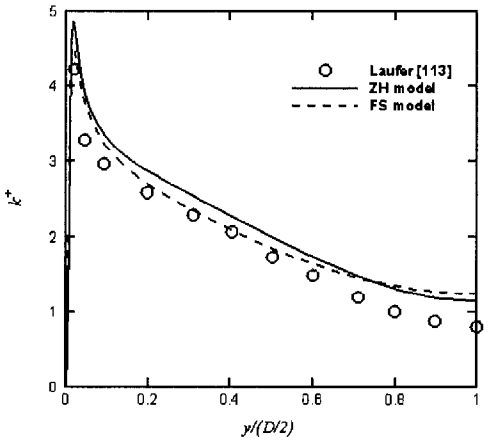

Figure 5. Comparisons of the turbulent kinetic energy in smooth pipe flows.

The computational results for smooth channel flows have been compared with the DNS data [114] at a Reynolds number, based on channel height, of 13,750 and the results are shown in Figure 6. Both models predict nicely the log-law velocity in the sublayer and outer layer, while the ZH model slightly overpredicts in the buffer

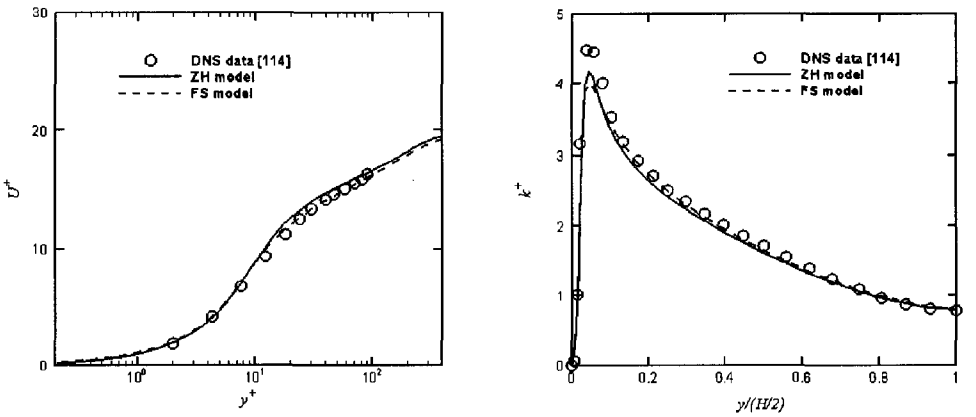

Figure 6. Comparisons of (a) the log-law velocity and (b) the turbulent kinetic energy in smooth channel flows.

layer comparing with the DNS data. The predictions of the turbulent kinetic energy from both models are in good agreement with the DNS data, with a slight underprediction of the peak turbulent kinetic energy near the wall.

The turbulent boundary layer flows over smooth plates were also simulated to assess the performance of both models, and the experimental results of Klebanoff [115] for Re_θ = 7700 are used here for comparison. As shown previously in Figure 4(a), the calculated skin friction coefficients are in good agreement with the experimental data. The computed log-law velocity profiles as shown in Figure 4(b) from both models also agree well with the measurements in the sublayer and outer layer,

while the ZH model slightly overpredicts the velocity in the buffer layer comparing with the experimental data. The results of the turbulent kinetic energy, and the Reynolds shear stress across the boundary layer are shown in Figure 7. The computational results of the turbulent kinetic energy from both models overpredict the peak of the turbulent kinetic energy near the wall, yet broadly follow the trend of the experimental data. It is also shown in Figure 7(b) that both models predict well the Reynolds shear stress in the inner region of y/δ < 0.2, and generally follow the trend of the experimental data in the outer region of y/δ > 0.2.

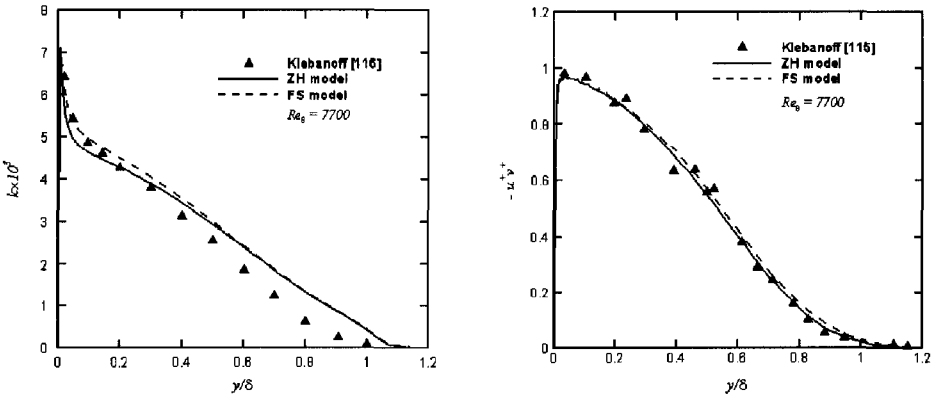

Figure 7. Comparisons of (a) the turbulent kinetic energy and (b) the Reynolds shear stress in flat plate turbulent boundary layers.

Rough pipe and channel flows

For the fully developed turbulent flows in rough

pipes, the comparisons of the calculated roughness function ΔU^+ with the experimental measurements of Prandtl and Schlichting [3], and Colebrook and White [4] in terms of k_{eq}^+ are shown in Figure 8. In the current calculations, the roughness function ΔU^+ is determined by

$$\begin{aligned} \Delta U^+ &= \left(\sqrt{2 / C_f}\right)_{smooth} - \left(\sqrt{2 / C_f}\right)_{rough} \\ &= \left(U_e / u_\tau\right)_{smooth} - \left(U_e / u_\tau\right)_{rough} \end{aligned} \qquad (4.16)$$

It can be observed that the ZH model underpredicts the roughness functions ΔU^+ more significantly than that of the FS model. The maximum difference between the predictions and the measurements is 40% for the ZH model, compared with 12% for the FS model.

The ZH and the FS models were also assessed by

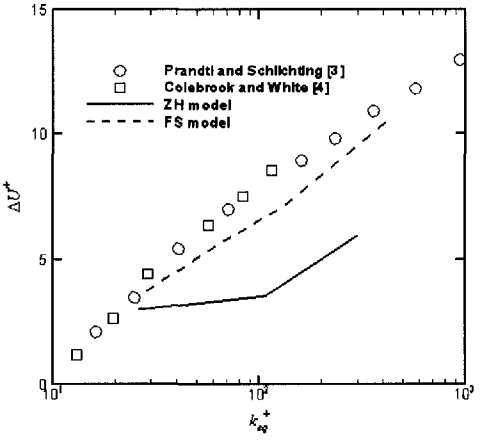

Figure 8. Comparisons of the roughness functions at various roughness heights in rough pipe flows.

simulating the fully developed turbulent rough channel flows measured by Zhang [119] and Bakken et al. [19]. Zhang [119] carried out an experimental study of turbulent flow in a rectangular channel with aspect ratio b/H = 5.5, which is covered with 100 grit sandpaper of k_{eq}/H = 0.0061 at a Reynolds number, based on channel height, of 70,909. Bakken et al. [19] measured turbulent channel flows covered with two different rough surfaces, including rod of k_s/H = 0.017 and mesh of k_s/H = 0.015. A range of Reynolds numbers, based on channel height, between 12,000 and 136,000 has been investigated. The results of Bakken et al. [19] show that in the fully rough regime ($k_{eq}^+ > 70$), the ratio k_{eq}/k_s is about 7.8 and 3.3 for the rod and mesh roughness, respectively, indicating a much stronger roughness effect for the rod roughness than for the mesh surface. The computational results of the log-law velocity comparing with the experimental measurements of Zhang [119] at k_{eq}^+ = 26.6 are presented in Figure 9. It can be observed that both models have predicted the correct slope, but slightly underpredict the roughness function ΔU^+ (about 7% from the experimental data).

The computational results corresponding to the experiments of Bakken et al. [19] with a Reynolds number, based on channel height, of 60,000 with rod roughness of k_{eq}^+ = 834.6, are given in Figure 10. For the log-law

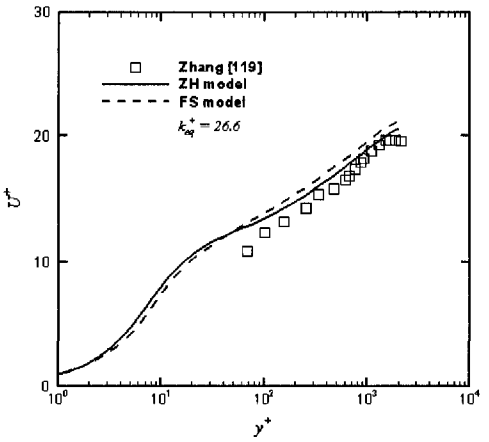

Figure 9. Comparisons of the log-law velocity in rough channel flows with roughness of sandpaper.

velocity profile (Figure 10(a)), both models predict the correct slope, but underpredict the roughness function ΔU^+. It can be also found that the ZH model provides fairly good predictions in the log-law velocity at low roughness k_{eq}^+, yet fails to predict the log-law velocity at high roughness k_{eq}^+. The computational results and the measured data for the Reynolds shear stress are compared in Figure 10(b). It is shown that the computed profiles for rod roughness from the ZH and the FS models collapse to the experimental data in the outer region for $y/(H/2) > 0.2$, which is consistent with the wall similarity hypothesis of Townsend [22]. In the inner region of $y/(H/2) < 0.2$, the peak level of the measured Reynolds shear stress profile is lower than the predictions. The

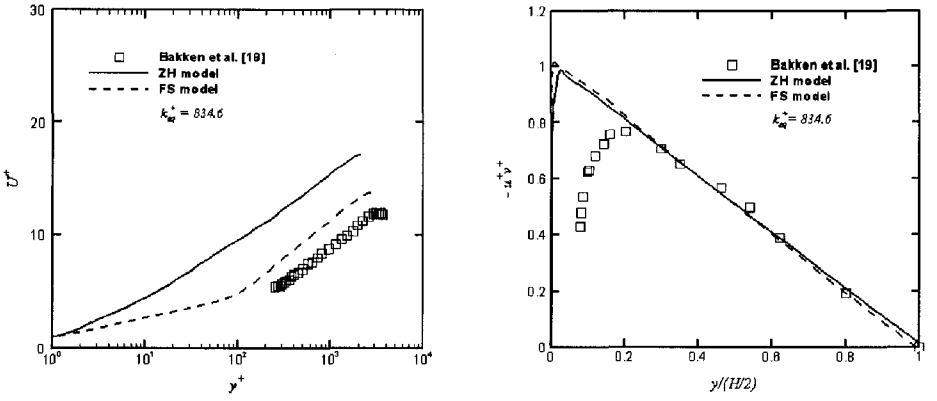

Figure 10. Comparisons of (a) the log-law velocity and (b) the Reynolds shear stress in rough channel flows with rod roughness.

reduced peak Reynolds shear stress has been attributed to the local flow acceleration ahead of and above the rod roughness [19].

The comparisons of the roughness function ΔU^+ with the experimental measurements of Prandtl and Schlichting [3] for a wide range of roughness k_{eq}^+ for the fully developed turbulent rough channel flows are presented in Figure 11. The FS model captures well the trend of the roughness function variation with the roughness height. However, it underpredicts the roughness function itself. The underprediction of roughness function for the ZH model is significant with a maximum of 38% for higher k_{eq}^+, compared with about 11% for that by the FS model. The ZH model provides good predictions of the log-law velocity

for low roughness of $k_{eq}^{+} < 30$. Note that the difference between the smooth and rough wall ZH model lies in the roughness modeling functions $g_1(k_{eq}^{+})$ and $g_2(k_{eq}^{+})$. For cases of smooth wall, $g_1(k_{eq}^{+}) = 0$ and $g_2(k_{eq}^{+}) = 1$.

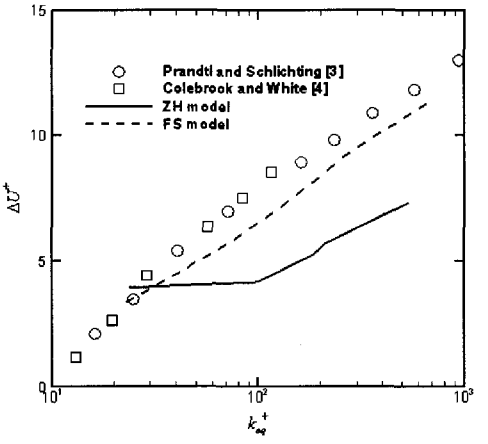

Figure 11. Comparisons of the roughness functions for a wide range of roughness height in rough channel flows.

Boundary layers over rough flat plates

The turbulent boundary layers over flat plates with different k-type surface roughness, including mesh [13,18], packed uniform spheres [17], and sandpaper [18], with the roughness k_{eq}^{+} of 340, 138, and 100, respectively, were simulated. These experiments are chosen because the measurements were made in the fully rough regime with moderate roughness k_{eq}^{+} for several different types of surface roughness.

The comparisons of the computed results with those of Antonia and Krogstad [13], which has been conducted at a Reynolds number, based on the plate length, of 4.62×10^6 with a mesh screen of k_s = 1.38 *mm* (k_{eq} = 4.96 *mm*) and k_{eq}^+ = 340 are provided in Figure 12. The experimental data were measured at Re_θ = 12,800. It is shown in Figure 12(a)

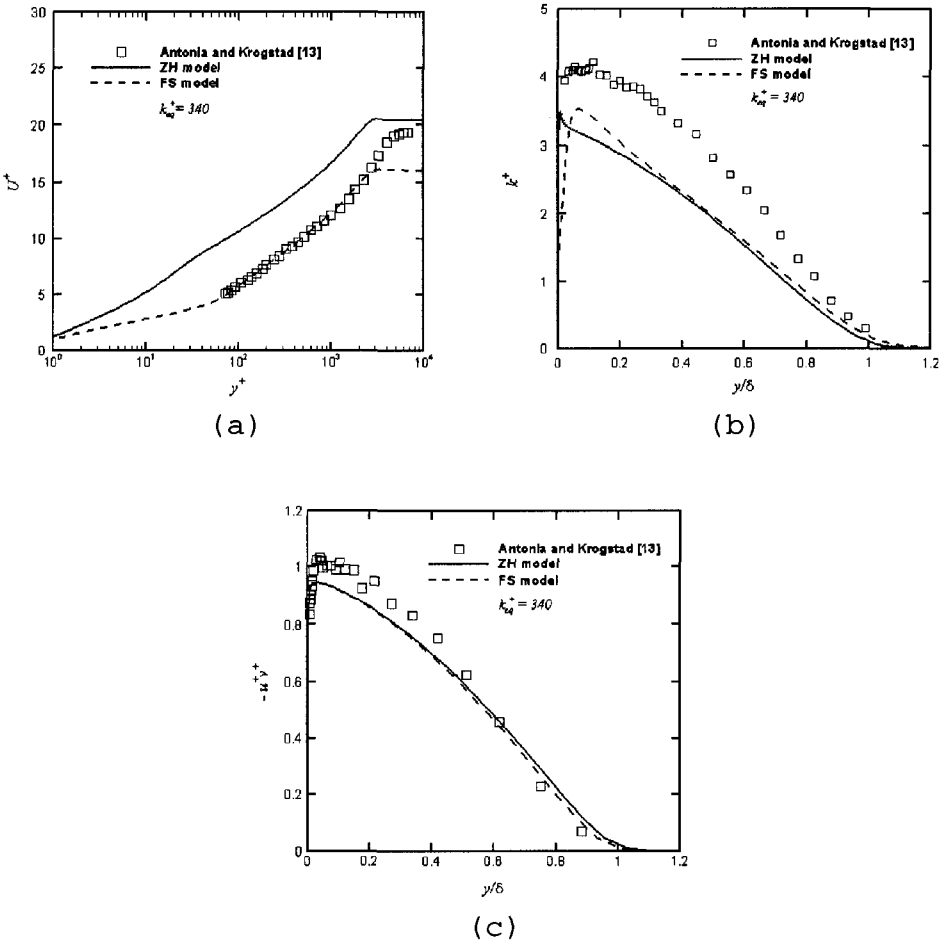

Figure 12. Comparisons of (a) the log-law velocity, (b) the turbulent kinetic energy and (c) the Reynolds shear stress at Re_θ = 12,800 in turbulent boundary layer with surface roughness of mesh screen.

that the log-law velocity profiles predicted from the FS model collapse to the experimental data for $y^+ < 2500$. The ZH model has predicted the correct slope, but it underpredicts the roughness function ΔU^+ by about 45% compared to the experimental data. The computed turbulent kinetic energy and the Reynolds shear stress are compared with the experimental measurements and the comparisons are shown in Figure 12(b) and Figure 12(c), respectively. Figure 12(b) shows that the computed profiles of k from both models behave similarly for $y/\delta > 0.3$. However, neither model predicts the turbulent kinetic energy distribution in the boundary layer. It is shown in Figure 12(c) that the predictions of the Reynolds shear stress from both models are in good agreement with the experimental data in the outer region for $y/\delta > 0.5$, and generally follow the trend of the experimental data.

The second rough wall turbulent boundary layer that has been calculated corresponds to that of Schultz and Flack [17] at a Reynolds number, based on the plate length, of 4.9×10^6 with the roughness of packed uniform spheres of $k_s = k_{eq} = 0.96 \pm 0.04$ *mm* and $k_{eq}^+ = 138$. The experimental study of Schultz and Flack [17] is among the few available experimental measurements that provide the skin friction coefficient data. The computational results of the ZH and the FS models for the skin friction coefficient are compared and the results are presented in

Figure 13. In the experimental study, the skin friction coefficient has been calculated using the total stress method,

$$C_f = \frac{2}{U_e^2}\left[\nu \frac{\partial \overline{u}}{\partial y} - \overline{u'v'}\right] \qquad (4.17)$$

while in the current calculations, the skin friction coefficient is determined directly from the wall shear stress. That is

$$C_f = 2(u_\tau / U_e)^2 \qquad (4.18)$$

It can be observed from Figure 13 that the FS model overpredicts the skin friction coefficient by about 10%

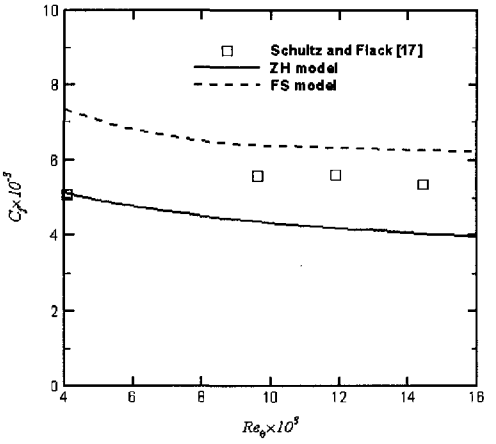

Figure 13. Predictions of the skin friction coefficients in turbulent boundary layer with surface roughness of uniform spheres.

compared to the experimental data, and the ZH model underpredicts the skin friction coefficient about 18%. The profiles of the log-law velocity and the Reynolds shear stress at Re_θ = 9620 are compared in Figure 14. For the mean velocity, the simulation results of the FS model are in a good agreement with the experimental data in the log-law region, while the ZH model predicts the correct slope yet underpredicts the roughness function by about 42%. The predictions of the Reynolds shear stress from both models are in good agreement with the experimental data except for the inner region of y/δ < 0.2.

The last set of comparisons for the turbulent boundary layers over rough flat plates is with that of Flack et al. [18]. The experimental measurements were

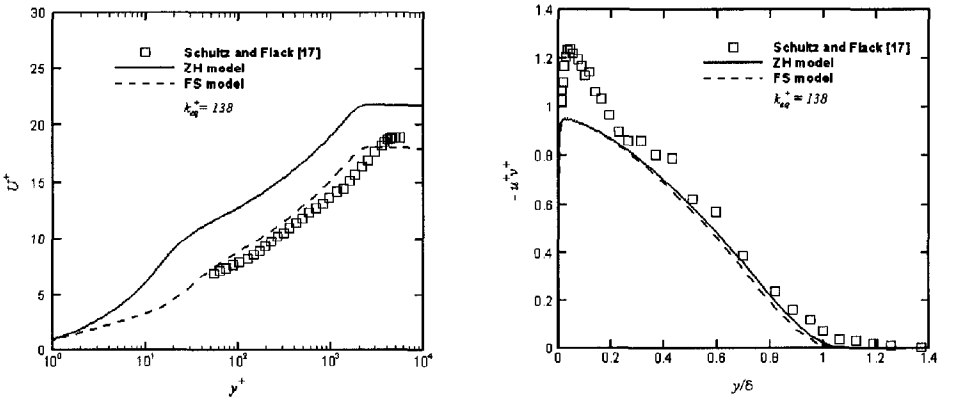

(a) (b)

Figure 14. Comparisons of (a) the log-law velocity and (b) the Reynolds shear stress at Re_θ = 9620 in turbulent boundary layer with surface roughness of uniform spheres.

carried out with two types of surface roughness. They include sandpaper of k_s = 0.69 *mm* (k_{eq} = 0.515 *mm*, k_{eq}^+ = 100) and mesh of k_s = 0.32 *mm* (k_{eq} = 0.69 *mm*, k_{eq}^+ = 138) at a Reynolds number, based on the plate length, of 5.1×10^6. The computational results for the mean velocity and the Reynolds shear stress, comparing with the experimental measurements over sandpaper roughness at Re_θ = 14,340, are shown in Figure 15. The mean velocity profile predicted by the FS model collapses with the experimental data for $y^+ < 2500$. The ZH model predicts the correct slope, yet underpredicts the roughness function by 40% comparing to the experimental data. It is shown in Figure 15(b) that the predictions of the Reynolds shear stress from both models are in good agreement with the

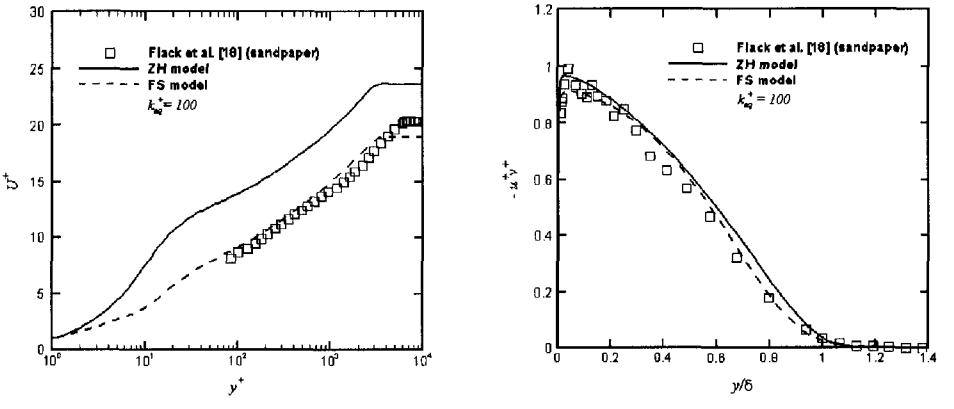

Figure 15. Comparisons of (a) the log-law velocity and (b) the Reynolds shear stress at Re_θ = 14,340 in turbulent boundary layer with surface roughness of sandpaper.

experimental data across the boundary layer. For the mesh roughness and Re_θ = 14,120, Figure 16 shows the computed log-law velocity and the Reynolds shear stress and their comparisons with the experimental measurements. The comparisons show the overall trends being very similar to the case with the sandpaper roughness (Figure 15).

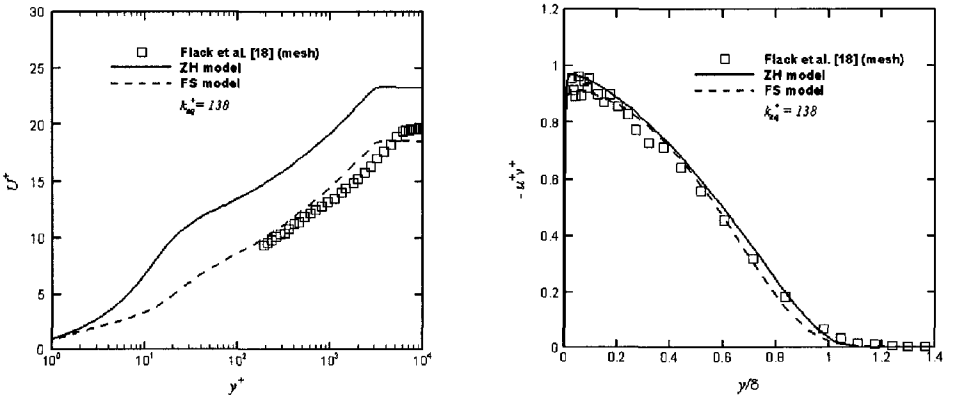

Figure 16. Comparisons of (a) the log-law velocity and (b) the Reynolds shear stress at Re_θ = 14,120 in turbulent boundary layer with surface roughness of mesh.

The predicted profiles of the Reynolds shear stress using the ZH and the FS models are similar with peak value around 1.0 at about y/δ = 0.05, and both models describe the Reynolds shear stress reasonably well across the boundary layer. The computational results of the Reynolds shear stress obtained by using both models also appear to support the wall similarity hypothesis of Townsend [22]. The FS model reproduces better the log-law

velocity profiles. Neither model predicts the correct U^+ at the free stream.

Since both models were developed by modifying the damping functions of the existing low-Reynolds-number $k-\varepsilon$ models by including the correlated roughness effect through the use of the equivalent sand roughness, we investigated the effect of roughness damping functions $f_{\mu,s}$ in Eq. (4.7) and Eq. (4.13) for the range of the roughness k_{eq}^+ used in this study. The comparisons of the two roughness damping functions $f_{\mu,s}$ at $y^+ = 0$ are presented in Figure 17. It can be observed that as the roughness k_{eq}^+ increases, the roughness damping functions $f_{\mu,s}$ at $y^+ = 0$ for both models increase as well. The difference between the two damping functions $f_{\mu,s}$ at $y^+ = 0$ is not significant for roughness k_{eq}^+ less than 30. For

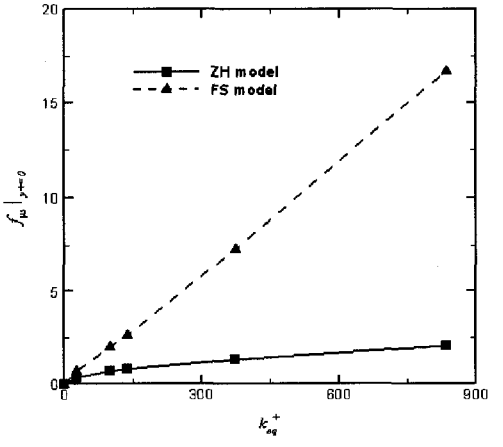

Figure 17. Comparisons of the two roughness damping functions at the wall.

large roughness k_{eq}^{+}, the values of the wall damping function for both models increase, with the FS model being significantly higher than that for the ZH model. In other words, the ZH model is providing less of an effect of the enhanced turbulent mixing due to roughness than that by the FS model, especially for large roughness k_{eq}^{+}. This may have caused the observed underprediciton of the roughness function for cases with high roughness.

Concluding remarks

The performance of two rough wall low-Reynolds-number $k-\varepsilon$ models has been assessed by simulating the fully developed turbulent flow in rough pipes, rough channels and over rough plates with the equivalent sand roughness k_{eq}^{+} ranging from 26.6 to 834.6. The predictions of the two models are examined against the published experimental measurements. The following remarks can be made based on the results comparing with the data.

(1) The model calculations of the fully developed turbulent flows in smooth pipes, smooth channels, and over smooth flat plates agree well with the experimental measurements and the DNS data.

(2) The FS model predicts reasonably well the log-law mean velocity profiles and the roughness function for all of the flows calculated. The predictions of the ZH model of the log-law mean velocity and the roughness

function are satisfactory for low roughness height of k_{eq}^{+} < 30.

(3) For both models, the predicted Reynolds shear stress profiles with the equivalent sand roughness k_{eq}^{+} ranging from 100 to 834.6 agree with the experimental data, except for the inner region $y/(H/2)$ < 0.2 of Bakken et al. [19] (channel flow) and the inner region y/δ <0.2 of Schultz and Flack [17] (flat plate boundary layer).

(4) Both models predict less satisfactorily the skin friction coefficient and the turbulent kinetic energy in the turbulent boundary layers over rough walls.

(5) The ZH model does not accurately predict the roughness function at higher roughness k_{eq}^{+}, which, when compared with the FS model, may have been caused by the insufficient amount of increase of the damping functions f_{μ} in the near rough wall region.

The results in this chapter, which examines only flows with simple geometries, suggest that there is a need for roughness modeling that can consistently predict the effect of roughness on not only the mean flow, but also the turbulence quantities in the RANS framework. Modeling may be developed that includes consideration of the interactions of the flow structures and roughness. Such physics-based modeling approaches may lead to more consistent and reliable predictions of turbulent flows over roughness.

CHAPTER V

A NEW TWO-EQUATION CLOSURE FOR TURBULENT FLOWS OVER ROUGH WALLS USING THE BRINKMAN EQUATION

In this chapter, a new modeling approach for the wall roughness effect is presented and turbulent boundary layer types of flows are considered. This new physics-based roughness model explicitly recognizes the inhomogeneous nature of the media, i.e. solid and fluid, in the roughness region. The dynamics of the fluid flow is filtered through volume averaging, which gives rise to the Brinkman equation frequently used in the study of flow through porous media. The geometry and the formation of the surface roughness are accounted for through porosity, that can be calculated mathematically, and permeability. The proposed exploratory use of the Brinkman equation [71] is innovative, since this widely used approach in porous medium flow calculations has never been applied to the modeling of the rough wall effects on high-Reynolds-number flows.

The flow domain is divided into a rough wall layer where the effects of roughness are modeled and an outer free flow region with fluid only. The fluid dynamics of the averaged flow in the rough wall layer is resolved by using the Brinkman equation, while the RANS equations are

employed in the outer free flow region. For the Reynolds stress closure, a two-equation $k-\varepsilon$ model has been developed. The model incorporates roughness-related closures to an existing, smooth wall, low-Reynolds-number model [97] and is employed in both the rough wall and the free flow regions. The porosity that appears in the Brinkman equation is determined based on the geometry and the formation of the roughness element. An interface condition [81,82] for the mean velocity and the stresses are applied at the interface between the rough wall and the free flow regions.

The implementation of the baseline low-Reynolds-number $k-\varepsilon$ model of Launder and Sharma [97] is first evaluated by comparing the calculated fully developed turbulent smooth channel flows and smooth wall turbulent boundary layers with DNS data [114] and experimental measurements [115]. The proposed new rough wall layer modeling using the Brinkman equation is then examined by simulating fully developed turbulent channel and boundary layer flows over different types of roughness. They include the turbulent rough channel flows with the square rod and the mesh roughness measured by Bakken et al. [19] and rough wall turbulent boundary layers with surface roughness of woven mesh [13,20], cylinder [43], square rod [27], and perforated plate [16]. These cases have been used to assess the present model, as the roughness

geometries are well-defined and the flows are considered fully rough based on the reported roughness Reynolds number k_s^+. The calculated results of the skin friction coefficient, the mean flow velocity, the roughness function, the Reynolds shear stress, and the turbulent kinetic energy, are compared with the corresponding experimental measurements.

In the following sections, the details of governing equations and the numerical methods used in this chapter are presented. These are followed by a section where the simulation results of the new rough wall layer modeling using the Brinkman equation are presented

Governing equations

The nondimensional, incompressible forms of time- and volume-averaged governing equations for the mean flow, Eqs. (3.1) and (3.2), and turbulent quantities, Eqs. (3.7) and (3.8), in a generalized curvilinear coordinates system for three different flow regions, as shown in Figure 1, are described as follows:

Free flow region

In the free flow region with homogeneous fluid, the dimensionless time- and volume-averaged governing equations for the mean flow can be written as

$$J \frac{\partial}{\partial \xi^i} \left(\frac{1}{J} V^i \right) = 0 \tag{5.1}$$

$$\frac{\partial \langle \overline{u}_i \rangle}{\partial t} + V^j \frac{\partial \langle \overline{u}_i \rangle}{\partial \xi^j} = -\xi^j_{x_i} \frac{\partial \langle \overline{P} \rangle}{\partial \xi^j} + J \frac{\partial}{\partial \xi^m} \left[\left(\frac{1}{Re} + \nu_t \right) \frac{g^{mn}}{J} \frac{\partial \langle \overline{u}_i \rangle}{\partial \xi^n} \right] \tag{5.2}$$

where Re, the Reynolds number, is defined as $U_0 L/\nu$ for boundary layer flows and $U_b H/\nu$ for channel flows. J, the Jacobian of the geometric transformation, and g^{mn}, the contravariant metric tensor of the geometric transformation, are defined in Eq. (3.3). V^j are the contravariant components of the mean Cartesian velocity components $\langle \overline{u}_i \rangle$ defined in Eq. (3.4).

The turbulent kinetic energy k and the dissipation rate of the turbulent kinetic energy ε are given as

$$k = \tfrac{1}{2} \langle \overline{u_i' u_i'} \rangle \tag{5.3}$$

$$\varepsilon = \frac{1}{Re} \langle \overline{\frac{\partial u_i'}{\partial x_j} \frac{\partial u_i'}{\partial x_j}} \rangle \tag{5.4}$$

The transport equations [97] for k and ε are

$$\frac{\partial k}{\partial t} + V^j \frac{\partial k}{\partial \xi^j} = J \frac{\partial}{\partial \xi^m} \left[\left(\frac{1}{Re} + \frac{\nu_t}{\sigma_k} \right) \frac{g^{mn}}{J} \frac{\partial k}{\partial \xi^n} \right] + G - \varepsilon - D \tag{5.5}$$

$$\frac{\partial \varepsilon}{\partial t} + V^j \frac{\partial \varepsilon}{\partial \xi^j} = J \frac{\partial}{\partial \xi^m}\left[\left(\frac{1}{Re} + \frac{\nu_t}{\sigma_\varepsilon}\right)\frac{g^{mn}}{J}\frac{\partial \varepsilon}{\partial \xi^n}\right] + C_1 f_1 \frac{\varepsilon}{k} G - C_2 f_2 \frac{\varepsilon^2}{k} + E \tag{5.6}$$

$$\nu_t = C_\mu f_\mu \frac{k^2}{\varepsilon} \tag{5.7}$$

$$D = \frac{2}{Re}\left(\xi^j_{x_2} \frac{\partial \sqrt{k}}{\partial \xi^j}\right)^2 \tag{5.8}$$

$$E = \frac{2\nu_t}{Re}\left[\xi^j_{x_2} \frac{\partial}{\partial \xi^j}\left(\xi^p_{x_2} \frac{\partial \langle \overline{u}_2 \rangle}{\partial \xi^p}\right)\right]^2 \tag{5.9}$$

The production term G in Eqs. (5.5) and (5.6) can be expressed as

$$G = \frac{1}{2}\nu_t\left(\frac{\partial \langle \overline{u}_i \rangle}{\partial \xi^k}\xi^k_{x_j} + \frac{\partial \langle \overline{u}_j \rangle}{\partial \xi^k}\xi^k_{x_i}\right)^2 \tag{5.10}$$

The value of the model constants are $\sigma_k = 1.0$, $\sigma_\varepsilon = 1.3$, $C_1 = 1.44$, $C_2 = 1.92$, and $C_\mu = 0.09$.

The damping functions f_μ, f_1, and f_2 proposed by Launder and Sharma [97] are,

$$f_\mu = exp\left[-3.4/\left(1 + R_t/50\right)^2\right] \tag{5.11}$$

$$f_1 = 1 \tag{5.12}$$

$$f_2 = 1 - 0.3\exp\left(-R_t^2\right) \tag{5.13}$$

Roughness region

In the surface roughness region with thickness δ_B, the analytical solution of the Brinkman equation, as shown in Eq. (2.28), for a boundary layer flow with constant porosity can be found [79]

$$\langle\overline{u}\rangle = \left(U_I - U_d\right)\cdot\exp\left[\sqrt{\varepsilon_\beta / Da}\cdot\left(y - \delta_B\right)\right] + U_d \tag{5.14}$$

$$\begin{aligned}\langle\overline{v}\rangle &= \sqrt{Da / \varepsilon_\beta}\cdot\frac{\partial\left(U_I - U_d\right)}{\partial x}\cdot\left\{1 - \exp\left[\sqrt{\varepsilon_\beta / Da}\cdot\left(y - \delta_B\right)\right]\right\} \\ &= -\frac{\partial U_d}{\partial x}\cdot\left(y - \delta_B\right) - V_I\end{aligned} \tag{5.15}$$

$$U_d = -Re\,Da\cdot\frac{d\langle\overline{P}\rangle}{\partial x} \tag{5.16}$$

where Da, the Darcy number, is defined as K/L^2 for boundary layer flows and K/H^2 for channel flows. Therefore, in the roughness region, the streamwise flow component decays exponentially toward the impermeable lower wall. U_I and V_I are the slip velocity components in the streamwise and the wall-normal directions,

respectively. The slip velocity at the interface will be determined by coupling with the free flow region solutions via the interface conditions that will be discussed later.

The dimensionless transport equations for k and ε for the disturbances in the roughness region with constant porosity and permeability are

$$\frac{\partial k}{\partial t} + \frac{1}{\varepsilon_\beta} V^j \frac{\partial k}{\partial \xi^j} = J \frac{\partial}{\partial \xi^m}\left[\left(\frac{1}{Re} + \frac{\nu_{t_{eff}}}{\sigma_k}\right) \frac{g^{mn}}{J} \frac{\partial k}{\partial \xi^n}\right] + \frac{1}{\varepsilon_\beta} G - \varepsilon - D - \overline{f}_i \langle \overline{u}_i \rangle \tag{5.17}$$

$$\frac{\partial \varepsilon}{\partial t} + \frac{1}{\varepsilon_\beta} V^j \frac{\partial \varepsilon}{\partial \xi^j} = J \frac{\partial}{\partial \xi^m}\left[\left(\frac{1}{Re} + \frac{\nu_{t_{eff}}}{\sigma_\varepsilon}\right) \frac{g^{mn}}{J} \frac{\partial \varepsilon}{\partial \xi^n}\right] + \frac{1}{\varepsilon_\beta} C_1 f_1 \frac{\varepsilon}{k} G - C_2 f_2 \frac{\varepsilon^2}{k} + E - C_3 \frac{\varepsilon}{k} \overline{f}_i \langle \overline{u}_i \rangle \tag{5.18}$$

$$\overline{f}_i = -\frac{1}{Re \cdot Da} \langle \overline{u}_i \rangle \tag{5.19}$$

$$\nu_{t_{eff}} = \frac{1}{\varepsilon_\beta} C_\mu f_\mu \frac{k^2}{\varepsilon} \tag{5.20}$$

Except for the drag force $\overline{f}_i$ related terms, the model equations are the same as that used in the free flow region. The drag force $\overline{f}_i$ has its origin in the volume-average Navier-Stokes equations [103]. As has been frequently invoked in porous medium studies, the

Forchheimer tensor [103] is assumed negligible, since the local Reynolds number of the flow in the roughness region is considered small [79]. The last term on the right-hand-side of Eq. (5.17) represents the work done by the drag force. The drag force term in Eq. (5.18) has been obtained by a simple scaling of the corresponding term in Eq. (5.17). As a result, the coefficient C_3 is a model constant. It was set at 0.11.

For the permeability K, a widely used correlation [99] in porous medium flow studies is employed. The resulting Darcy number Da can be written as

$$Da = \frac{\varepsilon_\beta{}^3 d_p{}^2}{180(1 - \varepsilon_\beta)^2} \tag{5.21}$$

Interface

For the flow involving a wall roughness and an unobstructed free flow region, an interface is identified between the free flow and the roughness regions. The interface conditions developed by Ochoa-Tapia and Whitaker [81,82] assumed a jump relation for the intrinsic stresses and a continuous superficial velocity across the interface. The interface conditions described in Chapter II are given as follows,

$$\langle \overline{u} \rangle \Big|_{\text{roughness}} = \langle \overline{u} \rangle \Big|_{\text{free flow}} = U_I \tag{5.22}$$

$$\left(\frac{1}{\varepsilon_\beta \, Re} + \nu_{t_{eff}} \right) \frac{\partial \langle \overline{u} \rangle}{\partial y} \Bigg|_{\text{roughness}} - \left(\frac{1}{Re} + \nu_t \right) \frac{\partial \langle \overline{u} \rangle}{\partial y} \Bigg|_{\text{free flow}}$$
$$= \left(\frac{1}{Re} + \nu_t \right) \frac{\beta_t}{\sqrt{K}} \cdot U_I \tag{5.23}$$

$$\langle \overline{v} \rangle \Big|_{\text{roughness}} = \langle \overline{v} \rangle \Big|_{\text{free flow}} = V_I \tag{5.24}$$

$$\left(\frac{1}{\varepsilon_\beta \, Re} + \nu_{t_{eff}} \right) \frac{\partial \langle \overline{v} \rangle}{\partial y} \Bigg|_{\text{roughness}} - \left(\frac{1}{Re} + \nu_t \right) \frac{\partial \langle \overline{v} \rangle}{\partial y} \Bigg|_{\text{free flow}}$$
$$= \left(\frac{1}{Re} + \nu_t \right) \frac{\beta_t}{2\sqrt{K}} \cdot U_I \tag{5.25}$$

$$1 / \varepsilon_\beta \cdot \langle \overline{P} \rangle \Big|_{\text{roughness}} = \langle \overline{P} \rangle \Big|_{\text{free flow}} \tag{5.26}$$

$$k \Big|_{\text{roughness}} = k \Big|_{\text{free flow}} \tag{5.27}$$

$$\varepsilon \Big|_{\text{roughness}} = \varepsilon \Big|_{\text{free flow}} \tag{5.28}$$

β_t and β_n are the tangential and normal stress jump parameters, respectively. The value of stress jump parameters might be chosen to accommodate engineering flows over porous media. The results of de Lemos and Silva [80] showed that a negative tangential stress jump parameter gave results that agreed with the experimental data for the turbulent kinetic energy at the interface.

In this research, we use β_t = -1, and β_n = 5. The constants were set based on generally accepted values. They have not been selected nor optimized for the calculations results shown here.

To form a closure model, the proposed expressions for the effective diameter parameter d_p and the thickness of the roughness region δ_B described in Chapter II are

$$d_p = (1 - \varepsilon_\beta)^3 \varepsilon_\beta^{\,2} k_s \tag{5.29}$$

$$\delta_B = (1 - \varepsilon_\beta)\varepsilon_\beta k_s \tag{5.30}$$

For all the cases presented in this chapter, the correlation gives the heights of the modeled roughness regions that are lower than that of the log-law layers. This conforms with the use of the Brinkman equation in the modeled roughness region in the present modeling framework.

In summary, in the current $k - \varepsilon$ formulation of the Brinkman equation modeling approach, the model equations are developed based on an existing smooth wall turbulence model and roughness-related model parameters are introduced. The parameters are C_3 in Eq. (5.18), d_p in Eq. (5.29), and δ_B in Eq. (5.30). For the present model, the flow domain is divided into a roughness region where the

effects of roughness are modeled and a free flow region with fluid only, as shown in Figure 1. The fluid dynamics of the averaged flow in the roughness region is determined using Eqs. (5.14) and (5.15), and the turbulent quantities needed for closure are resolved using Eqs. (5.17) and (5.18). The mean flow and turbulent characteristics in the free flow region are resolved using Eqs. (5.1) and (5.2), and Eqs. (5.5) and (5.6), respectively. The interface conditions, Eqs. (5.22)-(5.28) enforced the continuity of velocity, pressure, and turbulence properties, and the stress jump condition at the interface between the roughness and the free flow regions. The interface slip velocities thus obtained are then used to determine the averaged flow (Eqs. (5.14) and (5.15)) in the roughness region for next iteration.

Numerical details

The three-dimensional incompressible dimensionless time- and volume-averaged governing equations in the generalized curvilinear coordinates are discretized in space, on a non-staggered mesh using second-order finite difference approximations, and advanced in time using a four-stage Runge-Kutta scheme following a similar procedure described in Chapter III.

The mean flow and the turbulence modeling equations are solved in a weakly coupled manner. The *CFL* number

used in these computations is 1.5 for both the k and ε equations. The numerical solution process was regarded as converged with four to five orders-of-magnitude decrease of residuals.

Computational domains

In this chapter, two-dimensional solutions for channel and flat plate flows are sought. The computational domain corresponding to the fully developed turbulent smooth and rough channel flows extends 150 channel heights downstream. The flows are assumed symmetric along the centerline. For the turbulent boundary layers over smooth and rough plates, the computational domain extends one plate length downstream. For all the cases calculated, the resulting thickness of the modeled roughness region δ_B are below the log-law region ($\delta_B^+ < 30$).

Boundary conditions

The boundary conditions were specified as follows. The inlet boundary conditions for the fully developed turbulent smooth channel flows are assumed uniform for all variables, where $\langle\overline{u}\rangle = 1$, $\langle\overline{v}\rangle = 0$, $k = \varepsilon = 10^{-6}$. For the smooth flat plates, the Blasius solution has been used at the inlet with uniform profiles of $k = 0.013$ and

ε = 7 [117]. The smooth wall solutions thus obtained are then used to initialize the corresponding rough wall calculations. As for the symmetry boundaries, the mirror-image reflections for the grid and the flow variables are used for the fully developed turbulent smooth and rough channel flows. For all cases, the exit boundary condition is imposed by assuming zero streamwise diffusion. At the outer boundary of the flat plate, the turbulent boundary layer assumes the corresponding free stream conditions. The wall boundary condition is zero value for all variables, that is $\langle\overline{u}\rangle = \langle\overline{v}\rangle = k = \varepsilon = 0$.

Grid independence study

For the channel flows, the numerical grid in the wall-normal direction is generated by using a hyperbolic stretching function. The grid clusters near the inlet and is stretched using a hyperbolic stretching function toward the exit in the streamwise direction. A grid independence study for smooth channel flow has been performed, and the results are shown in Figure 18. Figure 18 shows the calculated log-law velocity profiles by using the present rough wall layer modeling with zero roughness region thickness ($\delta_B = 0$) on grids of 91×141, 55×141, and 55×181, in the streamwise and the wall-normal directions, respectively. The Reynolds number, based on

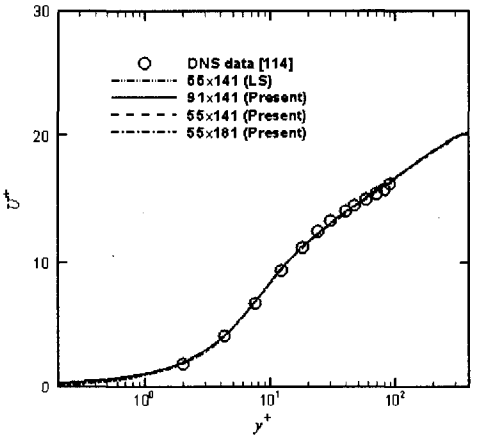

Figure 18. Grid independence study for channel flows with grid refinement in the wall-normal direction.

the channel height, is 13,750. The DNS data [114] are also included for comparison. Note that, for smooth wall, the present model naturally reduces to the baseline model of Launder and Sharma [97] (LS). The computed profiles using the different grids collapse, indicating the turbulent flow solutions being grid independent. The 55×141 grid is used in all the channel flow solutions presented here.

For the flat plate boundary flows, a hyperbolic tangent stretching function has been used in the wall-normal direction with grid clustered in the near wall region. The value of y^+ for the first grid point away from the wall is less than 0.1. The grid clusters near the inlet and is stretched using a hyperbolic stretching

function toward the exit in the streamwise direction. Figure 19 shows the results of the surface skin friction distributions, which are known to be sensitive to numerical grids, and the computed mean velocity profiles. The grid sizes vary between 71×150 and 281×150 (Figure 19(a)), and between 141×150 and 141×180 (Figure 19(b)). The results show that the numerical code achieves grid-independent solutions for the flat plate turbulent boundary layer. The turbulent flat plate boundary layer flow results presented have been obtained by using the 141×150 grid.

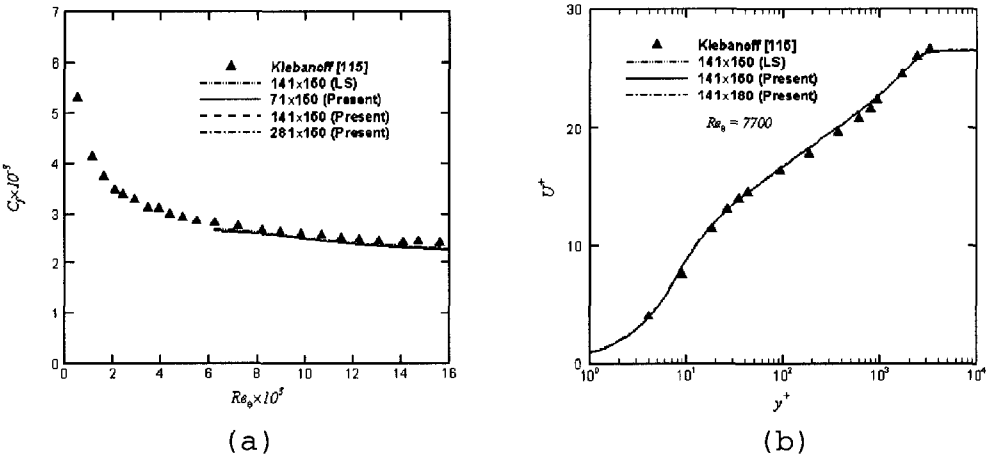

Figure 19. Grid independence study for flat plates with grid refinement in the (a) streamwise direction; (b) wall-normal direction.

Results and discussion

The results are reported and discussed in three

sections. The first section presents the calculation results of the present model with zero roughness region thickness (δ_B = 0) in fully developed turbulent smooth channel flows and smooth wall turbulent boundary layers, and their comparisons with the corresponding DNS data and experimental measurements. Results for fully developed rough channel flows and turbulent boundary layers over different types of surface roughness are presented in the second and the third sections, respectively. The results shown include the skin friction coefficient, the roughness function variation, the mean velocity, and turbulent quantity profiles. Where appropriate, the results are also compared with those from the model of Foti and Scandura [67] shown in Chapter IV.

Smooth channel flows and smooth wall turbulent boundary layers

For the fully developed turbulent smooth channel flows, the computational results are compared with the DNS data [114] at a Reynolds number, based on the channel height, of 13,750. As was mentioned earlier, in this case, the present low-Reynolds-number $k-\varepsilon$ model naturally reduces to that of the LS model. The comparisons of the log-law velocity and the turbulent kinetic energy are shown in Figure 18 and Figure 20, respectively. It is shown in Figure 18 that the predicted

log-law velocity profile collapses with that of the LS model and agrees well with data. The calculated turbulent kinetic energy, as shown in Figure 20, agrees well with that from the LS model.

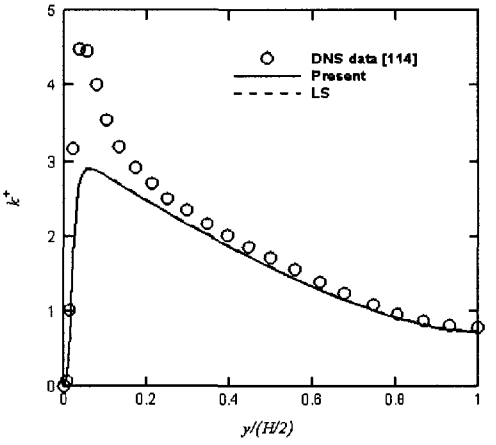

Figure 20. Comparisons of the turbulent kinetic energy in smooth channel flows.

The turbulent boundary layer flow over a smooth plate is also calculated. The experimental results of Klebanoff [115] for Re_θ = 7700 are used here for comparison. As shown previously in Figure 19(a), the calculated skin friction coefficients are in a good agreement with the experimental data. The computed log-law velocity profiles shown in Figure 19(b) also agree well with the data in the sublayer and outer layer. The results of the turbulent kinetic energy and the Reynolds shear stress across the boundary layer are shown in Figure 21. The present results agree well with that

obtained by using the LS model.

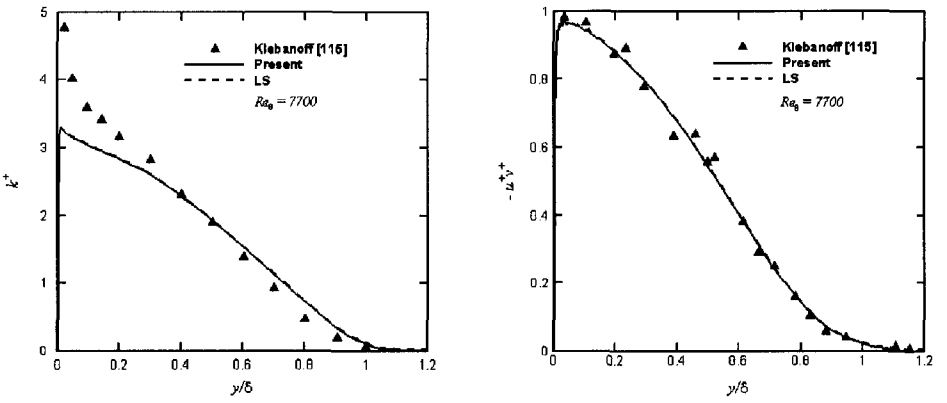

Figure 21. Comparisons of (a) the turbulent kinetic energy and (b) the Reynolds shear stress in flat plate turbulent boundary layers.

Rough channel flows

The fully developed rough channel flows of Bakken et al. [19] are calculated. Two different rough surfaces (Figure 22), i.e., mesh roughness of $k_s^+ = 83$ ($k_{eq}^+ = 273.9$) and square rod roughness of $k_s^+ = 107$ ($k_{eq}^+ = 834.6$), were

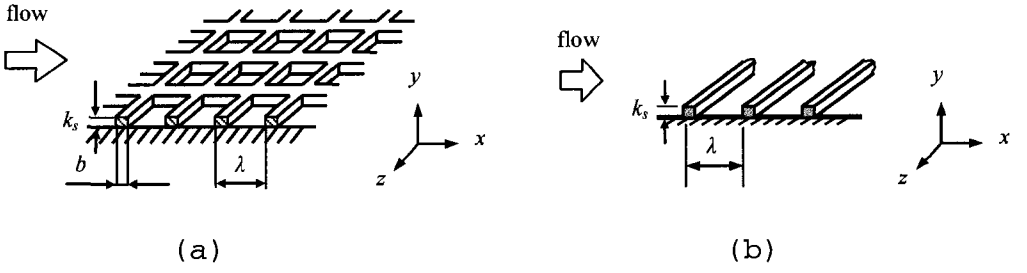

Figure 22. Sketch of surface roughness. (a) mesh; (b) square rod.

examined. The Reynolds numbers, based on the channel height, are 62,000 and 60,000 for the mesh and the square rod roughness, respectively. The porosity is calculated based on the volumetric characteristics of the roughness. The total stress method is used to determine the friction velocity u_τ. This method evaluates the sum of the viscous and the turbulent shear stresses in the overlap and inner layer of the boundary layer. That is,

$$u_\tau = \left[\frac{1}{Re} \frac{\partial \langle \overline{u} \rangle}{\partial y} - \langle \overline{u'v'} \rangle \right]^{1/2} \tag{5.31}$$

The calculated distribution of the log-law velocity, the Reynolds shear stress, and the turbulent kinetic energy across the channel are shown.

Mesh Roughness: Bakken et al. [19]

For the type of mesh roughness shown in Figure 22(a), the porosity can be readily calculated with a given square pattern center spacing λ and width b,

$$\varepsilon_\beta = \frac{\Delta V_\beta}{\Delta V} = \frac{(\lambda - b) \cdot (\lambda - b) \cdot k_s}{\lambda \cdot \lambda \cdot k_s} = \left[1 - \frac{b}{\lambda} \right]^2 \tag{5.32}$$

For Bakken et al. [19], $k_s = 0.015H$, $\lambda = 0.12H$, and $b = 0.02H$. The resulting porosity and Darcy number are 0.694

and 8.498×10^{-10}, respectively. The computed log-law velocity and the Reynolds shear stress, comparing with the numerical predictions from Foti and Scandura [67] (FS), and the measurements, are shown in Figure 23. Figure 23(a) shows that the present model predicts well the log-law velocity profile. The FS model predicts the correct slope, but underpredicts the roughness function ΔU^+. Figure 23(b) shows that the calculated Reynolds shear stress profiles from both models agree with the experimental data in the outer region of $y/(H/2) > 0.2$. In the inner region of $y/(H/2) < 0.2$, the peak level of the measured Reynolds shear stress profile is lower than the predictions. The reduced peak Reynolds shear stress has been attributed to the local flow acceleration ahead of and above the mesh roughness [19]. In the current

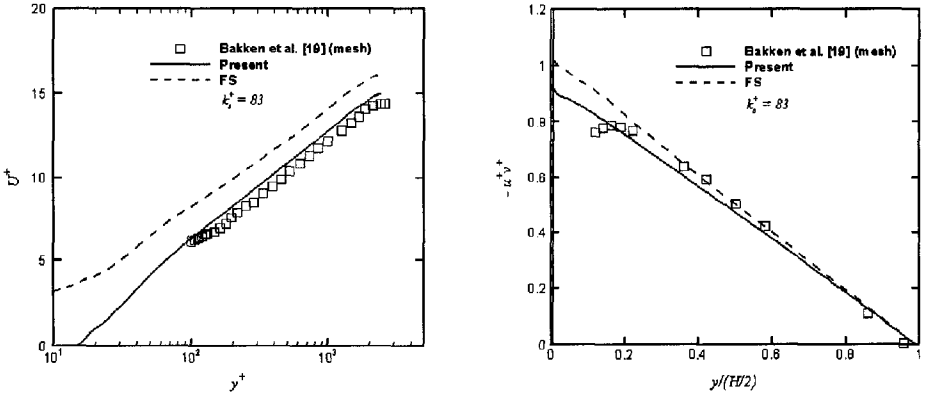

(a) (b)

Figure 23. Comparisons of (a) the log-law velocity and (b) the Reynolds shear stress in rough channel flows with mesh roughness.

$$\Delta U^{+} = \left(\sqrt{2 / C_f}\right)_{smooth} - \left(\sqrt{2 / C_f}\right)_{rough} \qquad (5.33)$$

and the skin friction coefficient from the present model is calculated using the following expression in the overlap and inner layer,

$$C_f = 2\left[\frac{1}{Re}\frac{\partial\langle\overline{u}\rangle}{\partial y} - \langle\overline{u'v'}\rangle\right] \qquad (5.34)$$

Square Rod Roughness: Bakken et al.[19]

For the square rod roughness shown in Figure 22(b), the porosity can be readily calculated with a given center-to-center spacing λ,

$$\varepsilon_\beta = \frac{\Delta V_\beta}{\Delta V} = \frac{\left(\lambda \cdot k_s - k_s \cdot k_s\right)}{\lambda \cdot k_s} = 1 - \frac{k_s}{\lambda} \qquad (5.35)$$

where $k_s = 0.017H$, and $\lambda = 0.136H$ for Bakken et al. [19]. The resulting porosity and Darcy number are 0.875 and 1.539×10^{-10}, respectively. Figure 24 shows calculated profiles of the log-law velocity, the Reynolds shear stress and the turbulent kinetic energy, comparing with the numerical predictions from the FS model and the measurements. It can be observed from Figure 24(a) that the log-law velocity profile predicted by the present model agrees well with the experimental data. The FS

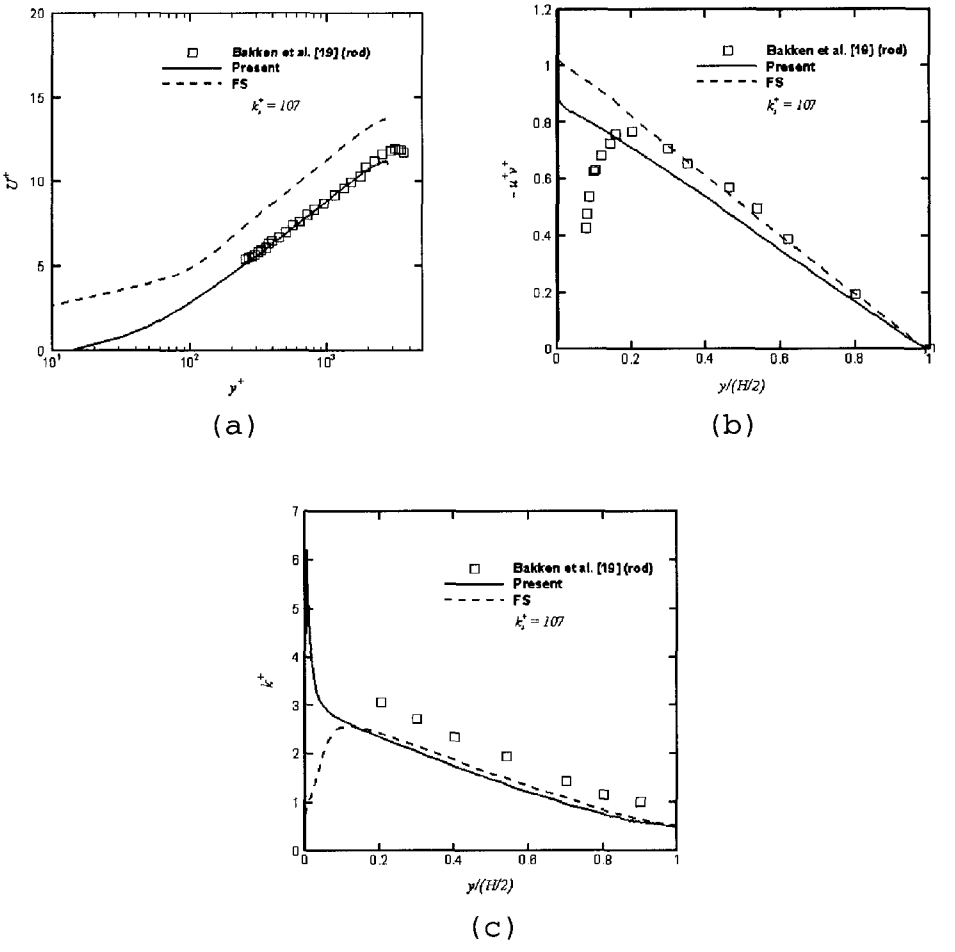

Figure 24. Comparisons of (a) the log-law velocity, (b) the Reynolds shear stress and (c) the turbulent kinetic energy in rough channel flows with square rod roughness.

model predicts the correct slope, yet it underpredicts the roughness function ΔU^+. It is shown in Figure 24(b) that the Reynolds shear stress profile calculated by using the FS model agrees better with the data than that from the present model for the outer region of $y/(H/2) >$ 0.2. It can be observed from Figure 24(c) that both

models underpredict the turbulent kinetic energy as reported by the experimental data.

Turbulent boundary layers over rough plates

The turbulent boundary layers over flat plate with different types of surface roughness were calculated. They include woven mesh [13,20], cylinder [43], square rod [27], and perforated plate [16]. The roughness Reynolds number k_s^+ ranges between 94.6 and 150. Based on the geometry of the roughness elements and their formations provided by the corresponding experimental measurements, the porosity ε_β for these different types of surface roughness vary from 0.398 to 0.898. Comparisons of the log-law velocity, the Reynolds shear stress, and the turbulent kinetic energy across the turbulent boundary layers are shown.

Woven Mesh Roughness: Antonia and Krogstad [13]

For the woven mesh roughness of k_s = 1.38 *mm* and k_s^+ = 94.6 (k_{eq}^+ = 340) shown in Figure 25, the porosity is calculated with the given square pattern center spacing λ and wire diameter d_w using the following formulation,

$$\varepsilon_\beta = \frac{\Delta V_\beta}{\Delta V} = \frac{\left[\lambda \cdot \lambda \cdot k_s - 2\left(\pi \cdot d_w^{\,2} / 4 \cdot \lambda\right)\right]}{\lambda \cdot \lambda \cdot k_s} = 1 - \frac{\pi \cdot d_w^{\,2} / 2}{\lambda \cdot k_s} \qquad (5.36)$$

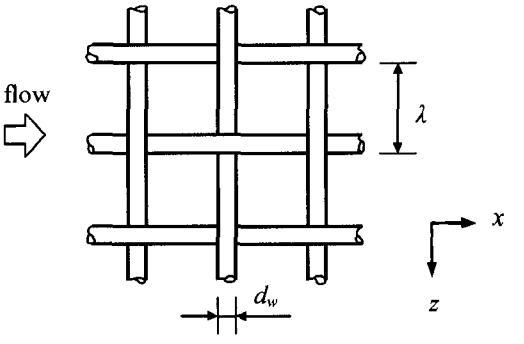

Figure 25. Sketch of woven mesh roughness.

where λ = 3.18 *mm*, and d_w = 0.69 *mm* for Antonia and Krogstad [13]. The resulting porosity ε_β = 0.83 and *Da* = 6.30×10^{-13}. The experiment study was conducted at a Reynolds number, based on the plate length, of 4.62×10^{6}, and the data were measured at Re_θ = 12,800.

The comparison results of the calculated log-law velocity, the Reynolds shear stress, and the turbulent kinetic energy with those by using the FS model and the experimental measurements are provided in Figure 26. It is shown in Figure 26(a) that the results of the present model agree satisfactorily with the experimental data in the log-law and the outer layer regions. The difference in the skin friction coefficient between the present calculations and the measurements is about 4.5%, compared to about 15% for that by the FS model. The Reynolds shear stress profiles calculated by both models agree with the

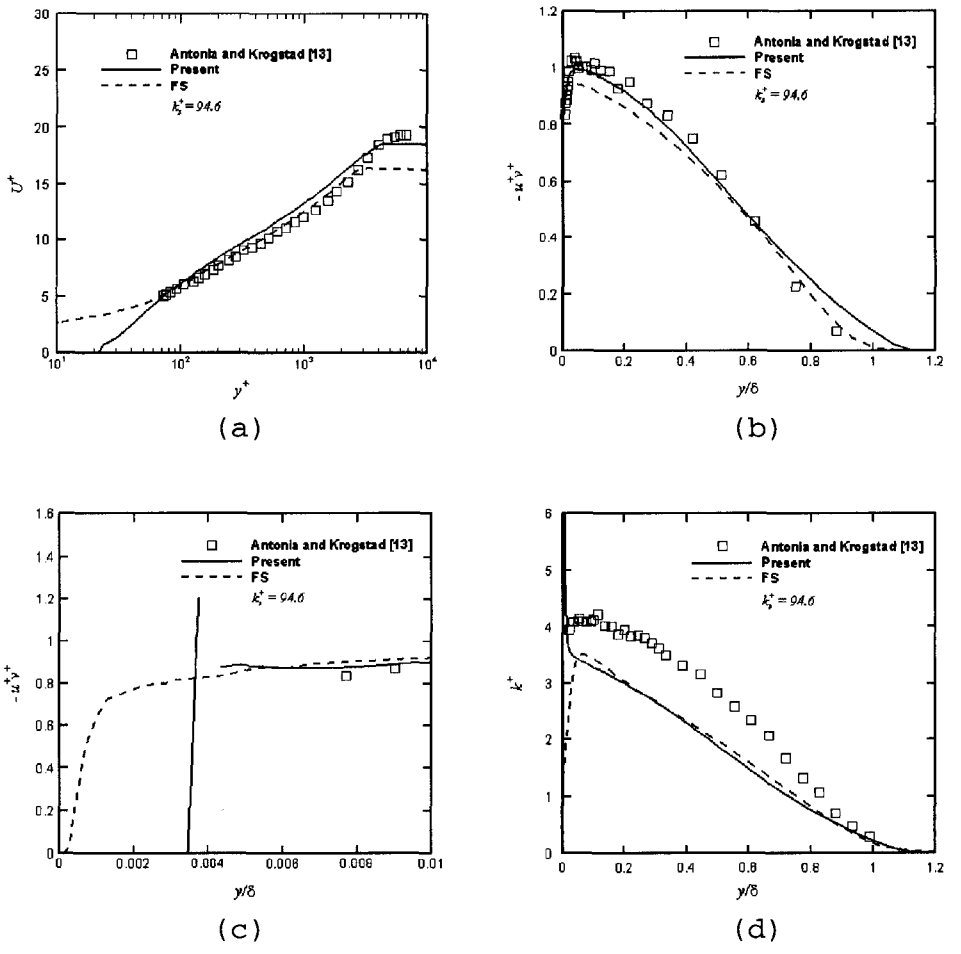

Figure 26. Comparisons of (a) the log-law velocity, (b) the Reynolds shear stress, (c) a close-up of the Reynolds shear stress and (d) the turbulent kinetic energy at Re_θ = 12,800 in turbulent boundary layer with surface roughness of mesh screen.

experimental data, and broadly follow the trend of the experimental data as shown in Figure 26(b). The present model employed an interface condition [81,82] that characterizes the slip velocity at the top of the modeled

roughness region by a jump of the velocity gradient across the interface. This results in a discontinuity of the Reynolds shear stress at the interface. Figure 26(c) shows a close-up of the Reynolds shear stress distribution in the near wall roughness region. The modeled interface is located at y/δ = 0.004, and the calculated streamwise slip velocity is U^* = 0.48. Except for nearing the interface, the present model describes a much reduced turbulent momentum transport in the modeled roughness layer, compared to that using the FS model, which essentially maintains the same level of the Reynolds stress in the roughness region. Turbulent fluctuations are mostly dampened in the roughness region. It is reasonable to expect that this damping effect, as is reflected in the present model results, lessens near the interface where the flow motion is far less restricted. It is shown in Figure 26(d) that both models less satisfactorily predict the turbulent kinetic energy across the boundary layer.

Woven Mesh Roughness: Flack et al. [20]

For the woven mesh roughness of k_s = 1.40 *mm* and k_s^+ = 150 (k_{eq}^+ = 370), similar to that shown in Figure 25, the porosity is calculated using Eq. (5.36) with λ/d_w = 4.58 [20]. The resulting porosity ε_β = 0.829 and *Da* = 8.943×10^{-13}. The experimental study of Flack et al. [20]

was conducted at a Reynolds number, based on the plate length, of 2.7×10^6, and the data were measured at Re_θ = 9110. The computed mean velocity and the Reynolds shear stress are shown in Figure 27. It can be observed from Figure 27(a) that the mean velocity profiles predicted by both models agree well with the experimental data in the log-law region. The present model provides the better prediction in the outer region than that of the FS model. It is shown in Figure 27(b) that the simulation results of both models show that the Reynolds shear stress profiles generally follow the trend of the experimental data and are in good agreement with the data across the turbulent boundary layer.

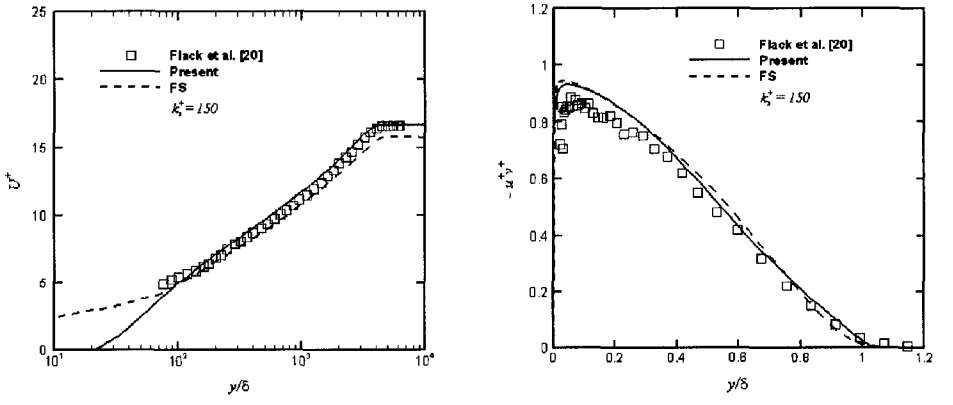

Figure 27. Comparisons of (a) the log-law velocity and (b) the Reynolds shear stress at Re_θ = 9110 in turbulent boundary layer with surface roughness of woven mesh.

Cylinder Roughness: George and Simpson [43]

For the cylinder roughness of k_s = 1.52 *mm* and k_s^+ = 128 shown in Figure 28, the porosity can be calculated using square pattern center spacing λ and cylinder diameter d_c as

$$\varepsilon_\beta = \frac{\Delta V_\beta}{\Delta V} = \frac{\left[\lambda \cdot \lambda \cdot k_s - \pi \cdot d_c^{\,2} / 4 \cdot k_s\right]}{\lambda \cdot \lambda \cdot k_s} = 1 - \frac{\pi \cdot d_c^{\,2} / 4}{\lambda^2} \qquad (5.37)$$

For λ = 5.486 *mm* and d_c = 1.98 *mm* [43], the resulting porosity ε_β = 0.898 and *Da* = 7.853×10^{-14}. The experimental study of George and Simpson [43] was conducted at a Reynolds number, based on the plate length, of 4.82×10^{6}, and the data were measured at the half spacing λ location directly behind the cylinder. The FS model was not carried out for comparison, since the equivalent sand

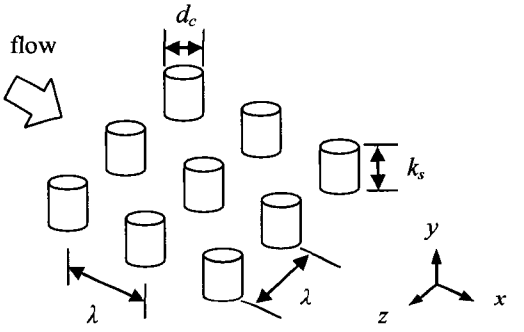

Figure 28. Sketch of cylinder roughness.

roughness k_{eq}^{+}, which is a FS model parameter, was not provided in George and Simpson [43].

It is shown in Figure 29(a) that the simulation results of the present model agree with the experimental data in the log-law region at Re_θ = 13,789. The

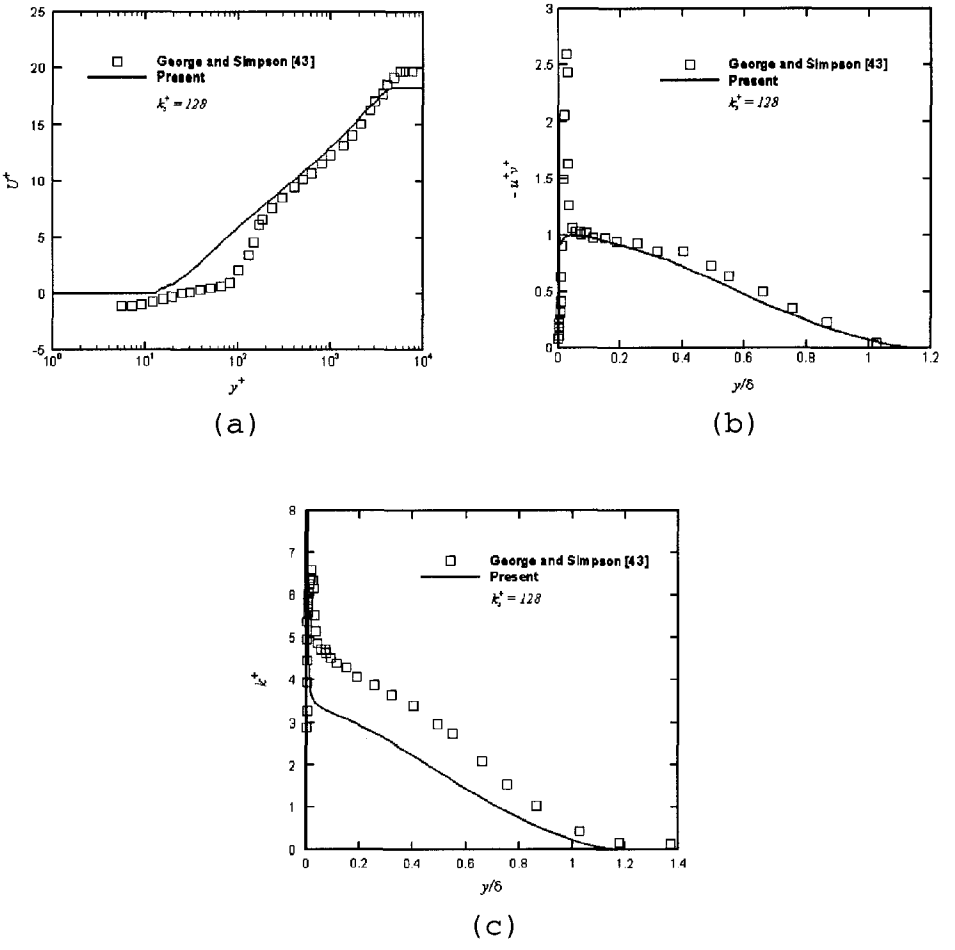

Figure 29. Comparisons of (a) the log-law velocity, (b) the Reynolds shear stress and (c) the turbulent kinetic energy at Re_θ = 13,789 in turbulent boundary layer with surface roughness of circular cylinders.

calculated free stream U^+ is slightly lower than the measurement. As the data were taken directly behind a cylinder roughness, a small reverse flow region is measured. The computed Reynolds shear stress and the turbulent kinetic energy are shown in Figure 29(b) and Figure 29(c), respectively. It can be observed from Figure 29(b) that the predicted Reynolds shear stress profile agrees well with the experimental data in the region where $y/\delta > 0.1$. For the turbulent kinetic energy as shown in Figure 29(c), the calculated distribution is less satisfactorily. The measured Reynolds shear stress and turbulent kinetic energy profiles show enhanced peaks near the top of the cylinder roughness. Arguably the shear-production mechanism associated with the flow around a roughness element is generally captured in the present modeling approach in an (volume) average manner.

Square Rod Roughness: Keirsbulck et al. [27]

For the square rod roughness of k_s = 3 *mm* and k_s^+ = 150, similar to that shown in Figure 22(b), the porosity is calculated using Eq. (5.35) with λ = 10 *mm* [27]. The resulting porosity ε_β = 0.7 and *Da* = 1.334×10^{-12}. The experimental study of Keirsbulck et al. [27] was conducted at a Reynolds number, based on the plate length, of 3.94×10^6, and the data were measured at Re_θ = 8549. The FS model was not carried out for comparison,

since the required equivalent sand roughness k_{eq}^{+} was not provided in Keirsbulck et a1. [27].

The computed mean velocity and the Reynolds shear stress are shown in Figure 30. The mean velocity profile predicted by the present model agrees well with the experimental data in the log-law layer region and in the outer layer region. The predicted Reynolds shear stress profile from the present model is in a good agreement with the experimental data for the region of y/δ > 0.6. The measured peak Reynolds shear stress level is lower than that calculated and decreases at a faster rate toward the wall than reported for other types of roughness in boundary layers [13,20,43].

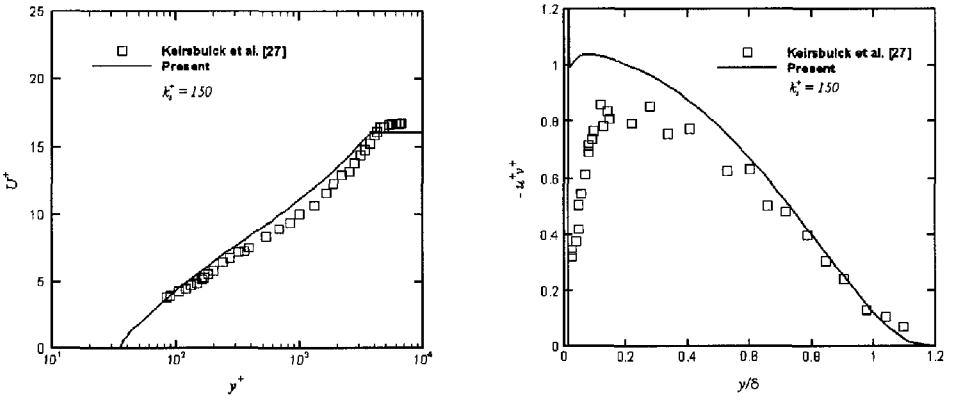

Figure 30. Comparisons of (a) the log-law velocity and (b) the Reynolds shear stress at Re_θ = 8549 in turbulent boundary layer with surface roughness of square rods.

Perforated Plate Roughness: Bergstrom et al. [16]

For the perforated plate roughness of k_s = 0.9 mm and k_s^+ = 122 (k_{eq}^+ = 149) as shown in Figure 31, the porosity can be calculated using the square pattern center spacing λ and the circular hole diameter d_h as

$$\varepsilon_\beta = \frac{\Delta V_\beta}{\Delta V} = \frac{\pi \cdot d_h^{\,2} / 4 \cdot k_s}{\lambda \cdot \lambda \cdot k_s} = \frac{\pi \cdot d_h^{\,2} / 4}{\lambda^2} \qquad (5.38)$$

where λ = 2.81 *mm* and d_h = 2 *mm* [16]. The resulting porosity ε_β = 0.398 and *Da* = 3.3487×10^{-13}. The experiment was conducted at a Reynolds number, based on the plate length, of 4.44×10^6, and is among the few available experimental measurements that provide the streamwise variation of skin friction coefficient. For the experimental study [16], the skin friction coefficient is calculated using Eq. (5.34), which is also used in the present model to determine the skin friction coefficient. The skin friction coefficient for the FS model is

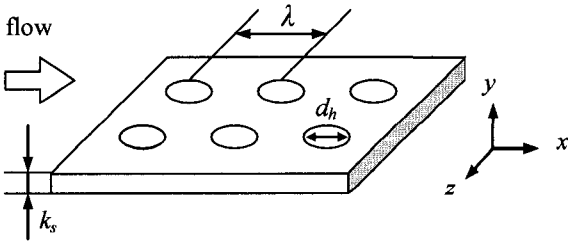

Figure 31. Sketch of perforated plate.

determined directly from the wall shear stress.

The computed streamwise development of the skin friction coefficients are presented in Figure 32. The present model predicts well the skin friction coefficient changes in the streamwise direction. For example, the differences between the predictions and measurements are about 4% for the present model at Re_θ = 11,460, and is about 19% for the FS model. The profiles of the log-law velocity at Re_θ = 11,460 are compared in Figure 33. It is shown that the predictions from the present model agree well with the experimental data in the log-law and the outer layer regions. The predicted profile from the FS model collapses to the experimental data in the log layer but diverges from the data in the outer layer.

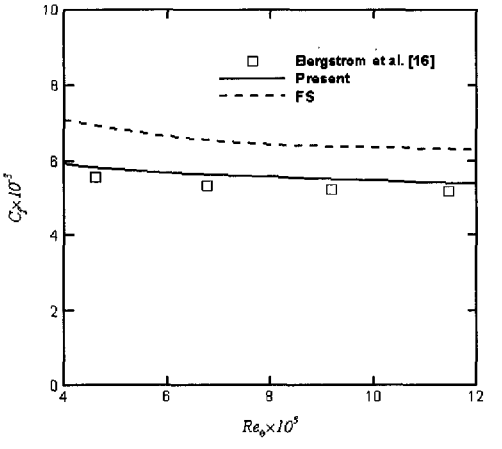

Figure 32. Predictions of the skin friction coefficients in turbulent boundary layer with surface roughness of perforated plate.

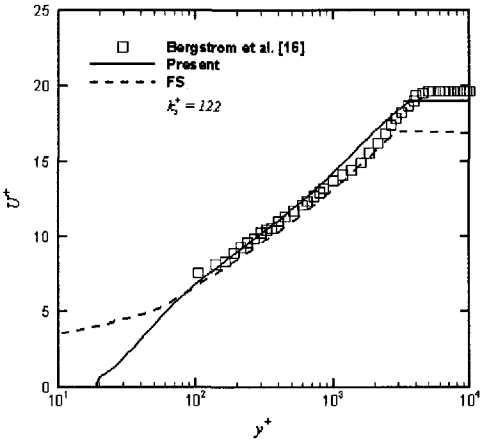

Figure 33. Comparisons of the log-law velocity at Re_θ = 11,460 in turbulent boundary layer with surface roughness of perforated plate.

In the above, the present model results for seven different rough-wall cases have been shown. The results were compared individually with those reported in the corresponding experimental studies. To provide an overall comparison, in Figure 34, the calculated roughness functions for all of these different cases are plotted versus their equivalent sand roughness k_{eq}^+ and compared with Prandtl and Schlichting [3]. The roughness functions predicted by the present model agree well with Prandtl and Schlichting [3] over the entire range of k_{eq}^+ calculated. In addition, in the region where the k_{eq}^+ for the rough channel flows overlaps with that for the rough boundary layers, the predictions consistently agree with

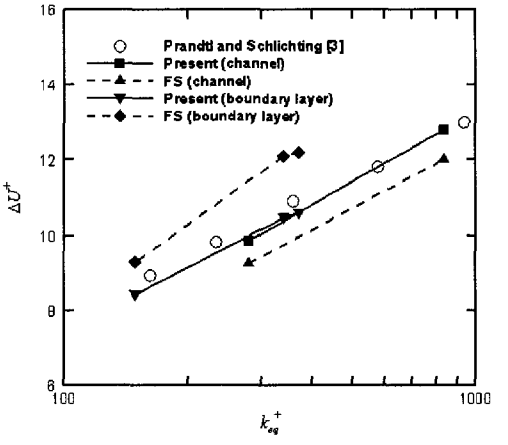

Figure 34. Comparisons of the roughness functions in terms of equivalent sand roughness heights.

Prandtl and Schlichting [3]. This is an encouraging observation for the present modeling approach as, unlike the FS model, k_{eq}^+ is not a model parameter in the present model formulation. It indicates that the present modeling approach that accounts explicitly for the geometry and the formation of the roughness element can lead to more consistent and reliable predictions of the mean flow.

Concluding remarks

A new flow physics-based surface roughness model is developed for the RANS numerical calculations of the high-Reynolds-number turbulent flows over rough walls. For the mean flow in the roughness region, the volume average method is used and the proposed modeling

framework results in the Brinkman equation. The porosity ε_β used in the Brinkman equation is obtained based on the geometry and the formation of the surface roughness. For the closure of the turbulent quantities, a low-Reynolds-number two-equation model was developed using a baseline, smooth wall turbulence model of Launder and Sharma [97]. The developed model is examined by simulating fully developed turbulent rough channel flows for the mesh and the square rod roughness measured by Bakken et al. [19] with the roughness Reynolds number k_s^+ of 83 and 107, respectively. Rough wall turbulent boundary layers with surface roughness of woven mesh [13,20], cylinder [43], square rod [27], and perforated plate [16] with the roughness Reynolds number k_s^+ ranging between 94.6 and 150 are also studied. The values of the porosity ε_β for these different types of surface roughness vary from 0.398 to 0.898. Based on the results reported, for the different roughness, we found that

(1) the present model predicts well the skin friction coefficient, the log-law mean velocity, and the roughness function for the calculated fully developed turbulent rough channel flows and the rough wall turbulent boundary layers over different types of surface roughness;

(2) the predicted Reynolds shear stress profiles generally agree well with the experimental data, except

for the square rod roughness of Bakken et al. [19] (channel flow) and Keirsbulck et al. [27] (boundary layer flow);

(3) the calculated turbulent kinetic energy agrees less satisfactorily with experimental measurements of Bakken et al. [19] in turbulent rough channel flows, and Antonia and Krogstad [13] and George and Simpson [43] in turbulent boundary layers over rough walls.

The proposed roughness modeling approach takes into account explicitly the effect of the formation and the topographical characteristics of the roughness and resolves the fluid dynamics of the averaged flow in the roughness region using the Brinkman equation. The results show that for the case presented, the new physics-based modeling approach can lead to a consistent and reliable modeling of the mean flow for a wide range of roughness type. A two-equation formulation has been adopted for turbulence modeling in the current implementation. In principle, other forms of turbulence closure modeling, for example: second-order Reynolds stress models, can also be adopted to the proposed rough wall layer modeling framework.

CHAPTER VI

A NEW SECOND-ORDER CLOSURE FOR TURBULENT FLOWS OVER ROUGH WALLS USING THE BRINKMAN EQUATION

In this chapter, a second-order Reynolds stress model [98] is adopted to the proposed rough wall layer modeling approach, that has a consistent and reliable modeling of the mean flow for a wide range of roughness type with a two-equation turbulence closure. The implementation of the baseline second-order Reynolds stress model of Launder and Shima [98] is first evaluated by comparing the calculated fully developed turbulent smooth channel flows and smooth wall turbulent boundary layers with DNS data [114] and experimental measurements [115]. A new second-order closure for the rough wall layer modeling using the Brinkman equation is then examined by simulating fully developed turbulent channel and boundary layer flows over different types of roughness. They include the turbulent rough channel flows with the square rod and the mesh roughness measured by Bakken et al. [19] and rough wall turbulent boundary layers with surface roughness of woven mesh [13,20], cylinder [43], square rod [27], and perforated plate [16]. These cases have been used to assess the present model, as the roughness geometries are well-defined and

the flows are considered fully rough based on the reported roughness Reynolds number k_s^+. The calculated results of the skin friction coefficient, the mean flow velocity, the roughness function, the Reynolds stresses, and the turbulent kinetic energy, are compared with the corresponding experimental measurements.

In the following sections, the details of governing equations and the numerical methods used in this chapter are presented. These are followed by a section where the simulation results of a new second-order closure for the rough wall layer modeling using the Brinkman equation are presented.

Governing equations

The nondimensional, incompressible forms of time- and volume-averaged governing equations for the mean flow, Eqs. (3.1) and (3.2), and turbulent quantities, Eqs. (3.5) and (3.6), in a generalized curvilinear coordinates system for three different flow regions, as shown in Figure 1, are described as follows:

Free flow region

In the free flow region with homogeneous fluid, the dimensionless time- and volume-averaged governing equations for the mean flow can be written as

$$J \frac{\partial}{\partial \xi^i} \left(\frac{1}{J} V^i \right) = 0 \tag{6.1}$$

$$\frac{\partial \langle \overline{u}_i \rangle}{\partial t} + V^k \frac{\partial \langle \overline{u}_i \rangle}{\partial \xi^k} = - \xi^k_{x_i} \frac{\partial \langle \overline{P} \rangle}{\partial \xi^k} + J \frac{\partial}{\partial \xi^m} \left(\frac{1}{Re} \frac{g^{mn}}{J} \frac{\partial \langle \overline{u}_i \rangle}{\partial \xi^n} \right) - J \frac{\partial}{\partial \xi^m} \left(\frac{1}{J} \xi^m_{x_j} \langle \overline{u_i' u_j'} \rangle \right) \tag{6.2}$$

where Re, the Reynolds number, is defined as $U_0 L/\nu$ for boundary layer flows and $U_b H/\nu$ for channel flows. J, the Jacobian of the geometric transformation, and g^{mn}, the contravariant metric tensor of the geometric transformation, are defined in Eq. (3.3). V^k are the contravariant components of the mean Cartesian velocity components $\langle \overline{u}_i \rangle$ defined in Eq. (3.4). The first, second, and third terms on the right-hand-side of Eq. (6.2) are the pressure gradient term, the diffusion term, and the Reynolds stress term, respectively.

The transport equations [98] for $\langle \overline{u_i' u_j'} \rangle$ and ε are

$$\frac{\partial \langle \overline{u_i' u_j'} \rangle}{\partial t} + V^k \frac{\partial \langle \overline{u_i' u_j'} \rangle}{\partial \xi^k} = J \frac{\partial}{\partial \xi^m} \left[\left(\frac{1}{J} c_s \frac{k}{\varepsilon} \xi^m_{x_k} \langle \overline{u_k' u_l'} \rangle \xi^n_{x_l} + \frac{1}{Re} \frac{g^{mn}}{J} \right) \frac{\partial \langle \overline{u_i' u_j'} \rangle}{\partial \xi^n} \right] + G_{ij} - \varepsilon_{ij} + \phi_{ij} \tag{6.3}$$

$$\frac{\partial \varepsilon}{\partial t} + V^k \frac{\partial \varepsilon}{\partial \xi^k} = J \frac{\partial}{\partial \xi^m} \left[\left(\frac{1}{J} c_\varepsilon \frac{k}{\varepsilon} \xi^m_{x_k} \langle \overline{u_k' u_l'} \rangle \xi^n_{x_l} + \frac{1}{Re} \frac{g^{mn}}{J} \right) \frac{\partial \varepsilon}{\partial \xi^n} \right] + (c_{\varepsilon 1} + \psi_1 + \psi_2) \left(\varepsilon / k \right) G - c_{\varepsilon 2} \left(\varepsilon \tilde{\varepsilon} / k \right) \tag{6.4}$$

The turbulent kinetic energy k and the dissipation rate of the turbulent kinetic energy ε are given as

$$k = \tfrac{1}{2} \langle \overline{u_i' u_i'} \rangle \tag{6.5}$$

$$\varepsilon = \frac{1}{Re} \langle \overline{\frac{\partial u_i'}{\partial x_j} \frac{\partial u_i'}{\partial x_j}} \rangle \tag{6.6}$$

The first term on the right-hand-side of Eq. (6.3) and Eq. (6.4) are total turbulent diffusion associated with velocity and pressure fluctuations and viscous diffusion terms, while the second and third terms represent production and dissipation terms, respectively. The production term in Eq. (6.3) can be expressed as follows:

$$G_{ij} = -\left(\langle \overline{u_i' u_k'} \rangle \xi^m_{x_k} \frac{\partial \langle \overline{u}_j \rangle}{\partial \xi^m} + \langle \overline{u_j' u_k'} \rangle \xi^m_{x_k} \frac{\partial \langle \overline{u}_i \rangle}{\partial \xi^m} \right) \tag{6.7}$$

The dissipation term in Eq. (6.3) has the form as

$$\varepsilon_{ij} = \frac{2}{3} \delta_{ij} \varepsilon \tag{6.8}$$

The last term on the right-hand-side of Eq. (6.3) represents the pressure strain term containing four distinct contributions [98]

$$\phi_{ij} = \phi_{ij1} + \phi_{ij2} + \phi^{w}_{ij1} + \phi^{w}_{ij2} \tag{6.9}$$

$$\phi_{ij1} = -c_1 \varepsilon a_{ij} \tag{6.9a}$$

$$\phi_{ij2} = -c_2 \left(G_{ij} - \tfrac{2}{3} \delta_{ij} G \right) \tag{6.9b}$$

$$\begin{aligned} \phi^{w}_{ij1} = \; & c^{w}_1 (\varepsilon/k) \Big[\langle \overline{u'_k u'_m} \rangle n_k n_m \delta_{ij} \\ & - (\tfrac{3}{2}) \langle \overline{u'_k u'_i} \rangle n_k n_j - (\tfrac{3}{2}) \langle \overline{u'_k u'_j} \rangle n_k n_i \Big] f_\phi \end{aligned} \tag{6.9c}$$

$$\phi^{w}_{ij2} = c^{w}_2 \left[\phi_{km2} n_k n_m \delta_{ij} - (\tfrac{3}{2}) \phi_{ik2} n_k n_j - (\tfrac{3}{2}) \phi_{jk2} n_k n_i \right] f_\phi \tag{6.9d}$$

where the forms of coefficients are

$$c_1 = -1 + 2.58 A A_2^{1/4} \left(1 - exp\left[- (0.0067 R_t)^2 \right] \right) \tag{6.10}$$

$$c_2 = 0.75 A^{1/2} \tag{6.11}$$

$$c^{w}_1 = - \tfrac{2}{3} c_1 + 1.67 \tag{6.12}$$

$$c^{w}_2 = max\left[\left(\tfrac{2}{3} c_2 - \tfrac{1}{6} \right) / c_2 , 0 \right] \tag{6.13}$$

$$a_{ij} = \left(\langle \overline{u'_i u'_j} \rangle - \tfrac{2}{3} \delta_{ij} k \right) k \tag{6.14}$$

$$A = \left[1 - 9/8 (A_2 - A_3) \right] \tag{6.15}$$

$$A_2 = a_{jk} a_{ki} \tag{6.16}$$

$$A_3 = a_{ik}a_{kj}a_{ji} \tag{6.17}$$

$$G = \tfrac{1}{2}G_{kk} \tag{6.18}$$

$$f_\phi = 0.4k^{3/2}/\varepsilon x_2 \tag{6.19}$$

R_t is the turbulence Reynolds number defined as $k^2/\varepsilon\nu$, and n_k is the unit vector perpendicular to the wall. The complete forms for production and dissipation terms in Eq. (6.4) can be expressed as follows:

$$\psi_1 = 2.5A(G/\varepsilon - 1) \tag{6.20}$$

$$\psi_2 = 0.3(1 - 0.3A_2)\exp\left[-(0.002R_t)^2\right] \tag{6.21}$$

$$\tilde{\varepsilon} = \varepsilon - \frac{2}{Re}\left(\xi^m_{x_2}\frac{\partial k^{\frac{1}{2}}}{\partial \xi^m}\right)^2 \tag{6.22}$$

In Eq. (6.3), c_s is the model constant, while c_ε, $c_{\varepsilon 1}$, and $c_{\varepsilon 2}$ in Eq. (6.4) are model constants as well. They have values of c_s = 0.11, c_ε = 0.18, $c_{\varepsilon 1}$ = 1.45, and $c_{\varepsilon 2}$ = 1.9.

Roughness region

In the surface roughness region with thickness δ_B, the analytical solution of the Brinkman equation, as

shown in Eq. (2.28), for a boundary layer flow with constant porosity can be found [79]

$$\langle \overline{u} \rangle = \left(U_I - U_d\right) \cdot \exp\left[\sqrt{\varepsilon_\beta / Da} \cdot \left(y - \delta_B\right)\right] + U_d \tag{6.23}$$

$$\begin{aligned} \langle \overline{v} \rangle &= \sqrt{Da / \varepsilon_\beta} \cdot \frac{\partial\left(U_I - U_d\right)}{\partial x} \cdot \left\{1 - \exp\left[\sqrt{\varepsilon_\beta / Da} \cdot \left(y - \delta_B\right)\right]\right\} \\ &= -\frac{\partial U_d}{\partial x} \cdot \left(y - \delta_B\right) - V_I \end{aligned} \tag{6.24}$$

$$U_d = -Re\, Da \cdot \frac{d\langle \overline{P} \rangle}{\partial x} \tag{6.25}$$

where Da, the Darcy number, is defined as K/L^2 for boundary layer flows and K/H^2 for channel flows. Therefore, in the roughness region, the streamwise flow component decays exponentially toward the impermeable lower wall. U_I and V_I are the slip velocity components in the streamwise and the wall-normal directions, respectively. The slip velocity at the interface will be determined by coupling with the free flow region solutions via the interface conditions that will be discussed later.

The dimensionless transport equations for $\langle \overline{u_i' u_j'} \rangle$ and ε in the roughness region with constant porosity and permeability are

$$\frac{\partial\overline{\langle u_i' u_j'\rangle}}{\partial t} + \frac{1}{\varepsilon_\beta} V^k \frac{\partial\overline{\langle u_i' u_j'\rangle}}{\partial \xi^k} = J \frac{\partial}{\partial \xi^m}\left[\left(\frac{1}{J} c_s \frac{k}{\varepsilon} \xi^m_{x_k} \overline{\langle u_k' u_l'\rangle} \xi^n_{x_l} + \frac{1}{Re}\frac{g^{mn}}{J}\right)\frac{\partial\overline{\langle u_i' u_j'\rangle}}{\partial \xi^n}\right] + \frac{1}{\varepsilon_\beta} G_{ij} - \varepsilon_{ij} + \phi_{ij} - F_{ij} \tag{6.26}$$

$$\frac{\partial \varepsilon}{\partial t} + \frac{1}{\varepsilon_\beta} V^k \frac{\partial \varepsilon}{\partial \xi^k} = J \frac{\partial}{\partial \xi^m}\left[\left(\frac{1}{J} c_\varepsilon \frac{k}{\varepsilon} \xi^m_{x_k} \overline{\langle u_k' u_l'\rangle} \xi^n_{x_l} + \frac{1}{Re}\frac{g^{mn}}{J}\right)\frac{\partial \varepsilon}{\partial \xi^n}\right] + (c_{\varepsilon 1} + \psi_1 + \psi_2)\left(\varepsilon/k\right) G - c_{\varepsilon 2}\left(\varepsilon\tilde{\varepsilon}/k\right) - c_{\varepsilon_3} \frac{\varepsilon}{k} F_{ii} \tag{6.27}$$

$$F_{ij} = \frac{\delta_{ij}}{3} \overline{f}_k \langle \overline{u}_k \rangle \tag{6.28}$$

$$\overline{f}_k = -\frac{1}{Re \cdot Da} \langle \overline{u}_k \rangle \tag{6.29}$$

The drag force term F_{ij} in Eq. (6.26) is modeled based on the assumption of isotropic partition [75]. The drag force term in Eq. (6.27) has been obtained by a simple scaling of the corresponding term in Eq. (6.26). As a result, the coefficient c_{ε_3} is a model constant. It was set at 0.11.

For the permeability K, a widely used correlation [99] in porous medium flow studies is employed. The resulting Darcy number Da can be written as

$$Da = \frac{\varepsilon_\beta^{\,3} d_p^{\,2}}{180(1-\varepsilon_\beta)^2} \tag{6.30}$$

Interface

For the flow involving a wall roughness and an unobstructed free flow region, an interface is identified between the free flow and the roughness regions. The interface conditions for the proposed new rough wall layer modeling using the Brinkman equation with a second-order turbulence closure described in Chapter II are

$$\langle \overline{u} \rangle\big|_{\text{roughness}} = \langle \overline{u} \rangle\big|_{\text{free flow}} = U_I \tag{6.31}$$

$$\frac{1}{\varepsilon_\beta\, Re}\frac{\partial \langle \overline{u} \rangle}{\partial y}\bigg|_{\text{roughness}} - \frac{1}{Re}\frac{\partial \langle \overline{u} \rangle}{\partial y}\bigg|_{\text{free flow}} - \langle \overline{u'v'} \rangle_I \left(\frac{1}{\varepsilon_\beta} - 1\right) = \frac{1}{Re}\frac{\beta_t}{\sqrt{K}} \cdot U_I \tag{6.32}$$

$$\langle \overline{v} \rangle\big|_{\text{roughness}} = \langle \overline{v} \rangle\big|_{\text{free flow}} = V_I \tag{6.33}$$

$$\frac{1}{\varepsilon_\beta \cdot Re}\frac{\partial \langle \overline{v} \rangle}{\partial y}\bigg|_{\text{roughness}} - \frac{1}{Re}\frac{\partial \langle \overline{v} \rangle}{\partial y}\bigg|_{\text{free flow}} - \langle \overline{v'v'} \rangle_I \left(\frac{1}{\varepsilon_\beta} - 1\right) = \frac{1}{Re}\frac{\beta_n}{\sqrt{K}} \cdot V_I \tag{6.34}$$

$$1 / \varepsilon_\beta \cdot \langle \overline{P} \rangle\big|_{\text{roughness}} = \langle \overline{P} \rangle\big|_{\text{free flow}} \tag{6.35}$$

$$\langle \overline{u_i' u_j'} \rangle \Big|_{\text{roughness}} = \langle \overline{u_i' u_j'} \rangle \Big|_{\text{free flow}} = \langle \overline{u_i' u_j'} \rangle_I \tag{6.36}$$

$$\varepsilon \Big|_{\text{roughness}} = \varepsilon \Big|_{\text{free flow}} \tag{6.37}$$

β_t and β_n are the tangential and normal stress jump parameters, respectively. The value of stress jump parameters might be chosen to accommodate engineering flows over porous media. In this research, we use β_t = -1, and β_n = 5. The constants were set based on generally accepted values. They have not been selected nor optimized for the calculations results shown here.

To form a closure model, the proposed expressions for the effective diameter parameter d_p and the thickness of the roughness region δ_B described in Chapter II are

$$d_p = (1 - \varepsilon_\beta)^3 \varepsilon_\beta^{\,2} k_s \tag{6.38}$$

$$\delta_B = (1 - \varepsilon_\beta) \varepsilon_\beta k_s \tag{6.39}$$

For all the cases presented in this chapter, the correlation gives the heights of the modeled roughness regions that are lower than that of the log-law layers. This conforms with the use of the Brinkman equation in the modeled roughness region in the present modeling

framework.

In summary, in the current second-order turbulence closure formulation of the Brinkman equation modeling approach, the model equations are developed based on an existing smooth wall turbulence model and roughness-related model parameters are introduced. The parameters are C_3 in Eq. (6.27), d_p in Eq. (6.38), and δ_B in Eq. (6.39). For the present model, the flow domain is divided into a roughness region where the effects of roughness are modeled and a free flow region with fluid only, as shown in Figure 1. The fluid dynamics of the averaged flow in the roughness region is determined using Eqs. (6.23) and (6.24), and the turbulent quantities needed for closure are resolved using Eqs. (6.26) and (6.27). The mean flow and turbulent characteristics in the free flow region are resolved using Eqs. (6.1) and (6.2), and Eqs. (6.3) and (6.4), respectively. The interface conditions, Eqs. (6.31)-(6.37) enforced the continuity of velocity, pressure, and turbulence properties, and the stress jump condition at the interface between the roughness and the free flow regions. The interface slip velocities thus obtained are then used to determine the averaged flow (Eqs. (6.23) and (6.24)) in the roughness region for next iteration.

Numerical details

The three-dimensional incompressible dimensionless time- and volume-averaged governing equations in the generalized curvilinear coordinates are discretized in space, on a non-staggered mesh using second-order finite difference approximations, and advanced in time using a four-stage Runge-Kutta scheme following a similar procedure described in Chapter III.

The mean flow and the turbulence modeling equations are solved in a weakly coupled manner. The *CFL* number used in these computations is 1.2 for both $\langle \overline{u_i' u_j'} \rangle$ and ε equations. The numerical solution process was regarded as converged with four to five orders-of-magnitude decrease of residuals.

Computational domains

In this chapter, two-dimensional solutions for channels and flat plates are sought. The computational domain corresponding to the fully developed turbulent smooth and rough channel flows extends 150 channel heights downstream, and the flows are assumed symmetric along the centerline. The mesh is the same as that used in Chapter V, and the numerical grid consists of 55×141 grid nodes in the streamwise and the wall-normal directions, respectively. For the turbulent boundary

layers over smooth and rough plates, the computational domain extends one plate length downstream. The mesh is stretched using the same method as that described in Chapter V, and the numerical grid of 141×150 in the streamwise and vertical directions, respectively, was chosen based on the results of a grid independence study as shown in Chapter V. For all the cases calculated, the resulting thickness of the modeled roughness region δ_B are below the log-law region ($\delta_B^+ < 30$).

Boundary conditions

The boundary conditions were specified as follows. The inlet boundary conditions for the fully developed turbulent smooth channel flows are assumed uniform for all variables, where $\langle\overline{u}\rangle = 1$, $\langle\overline{v}\rangle = 0$, $\langle\overline{u_i'u_j'}\rangle = \varepsilon = 10^{-6}$. For the smooth flat plates, the Blasius solution has been used at the inlet with uniform profiles of $\langle\overline{u_i'u_j'}\rangle = 0.001$ and $\varepsilon = 1.25$. The smooth wall solutions thus obtained are then used to initialize the corresponding rough wall calculations. As for the symmetry boundaries, the mirror-image reflections for the grid and the flow variables are used for the fully developed turbulent smooth and rough channel flows. For all cases, the exit boundary condition is imposed by assuming zero streamwise diffusion. At the outer boundary of the flat plate, the turbulent boundary layer assumes the corresponding free stream conditions.

The wall boundary condition is zero value for the velocity and the Reynolds stress components, that is $\langle \overline{u} \rangle = \langle \overline{v} \rangle = \langle \overline{u_i' u_j'} \rangle = 0$, while $\varepsilon = 2/Re(\partial k^{1/2}/\partial y)^2$ [98].

Results and discussion

The results are reported and discussed in three sections. The first section presents the calculation results of the Reynolds stress model (RSM) of the present modeling approach with zero roughness region thickness ($\delta_B = 0$) in fully developed turbulent smooth channel flows and smooth wall turbulent boundary layers, and their comparisons with the corresponding DNS data [114] and experimental measurements [115]. Results for fully developed rough channel flows and turbulent boundary layers over different types of surface roughness are presented in the second and the third sections, respectively. The results shown include the skin friction coefficient, the roughness function variation, the mean velocity, and turbulent quantity profiles. The results are also compared with previous solutions shown in Chapter V obtained by using the two-equation model (TEM).

Smooth channel flows and smooth wall turbulent boundary layers

For the fully developed turbulent smooth channel flows, the computational results are compared with the

DNS data [114] at a Reynolds number, based on the channel height, of 13,750. Note that, for smooth wall, the present RSM naturally reduces to the baseline model of Launder and Shima [98]. The comparisons of the log-law velocity, the turbulent kinetic energy, and the Reynolds shear stress are shown in Figure 35. It is shown in Figure 35(a) that the predicted log-law velocity profile

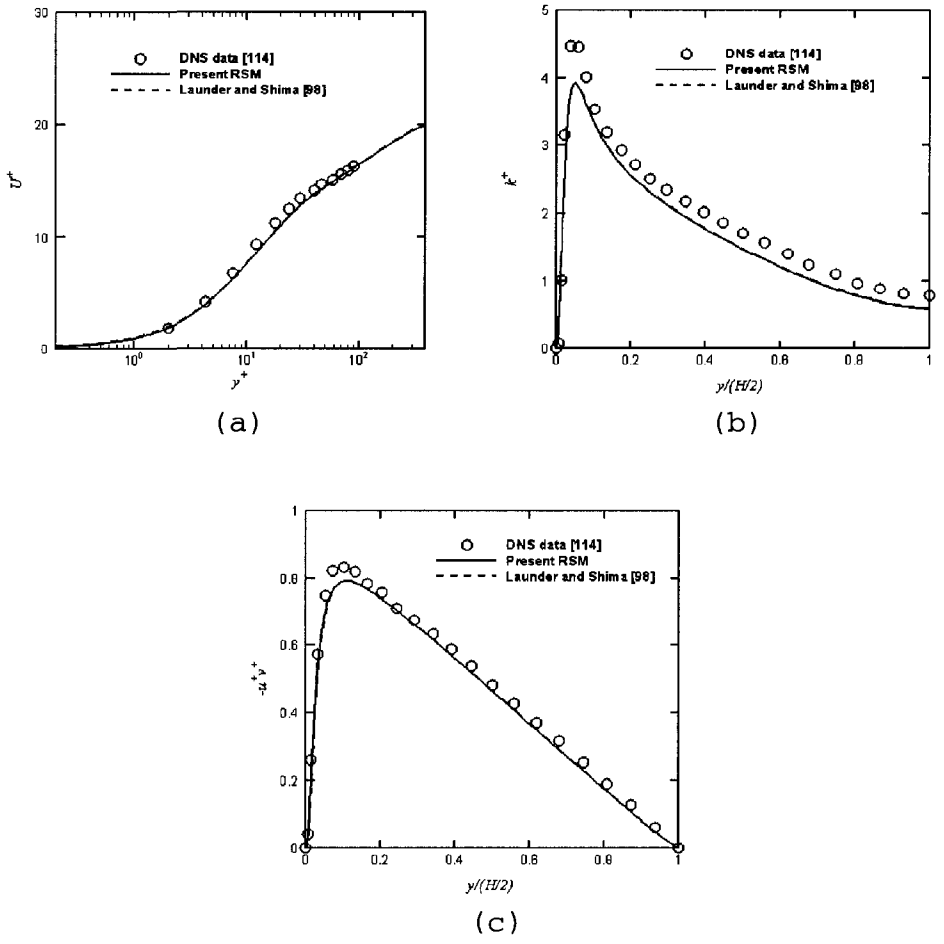

Figure 35. Comparisons of (a) the log-law velocity, (b) the turbulent kinetic energy and (c) the Reynolds shear stress in smooth channel flows.

collapses to that of the model of Launder and Shima [98], and agrees well with data. The calculated profiles of the turbulent kinetic energy (Figure 35(b)) and the Reynolds shear stress (Figure 35(c)) agree well with those from model of Launder and Shima [98].

The turbulent boundary layer flow over a smooth plate is also calculated. The experimental results of Klebanoff [115] for Re_θ = 7700 are used here for comparison. Figure 36(a) shows that the calculated skin friction coefficients are in good agreement with the experimental data. The computed log-law velocity profiles shown in Figure 36(b) also agree well with the data in the sublayer and outer layer. The computational results of the turbulent intensities and the Reynolds shear stress across the boundary layer are shown in Figure 36(c) and Figure 36(d), respectively. The turbulent intensity profiles broadly follow the trends of the experimental data, with u^+ reaching a maximum around 2.5 in close agreement with experimental measurements. The velocity fluctuations normal to the wall are much smaller, with v^+ reaching a flat maximum value well beyond the edge of the viscosity-affected region. The computational results of the Reynolds shear stress from the present RSM has been verified with that of Launder and Shima [98], and both results lie above the experimental data over much of the boundary layer.

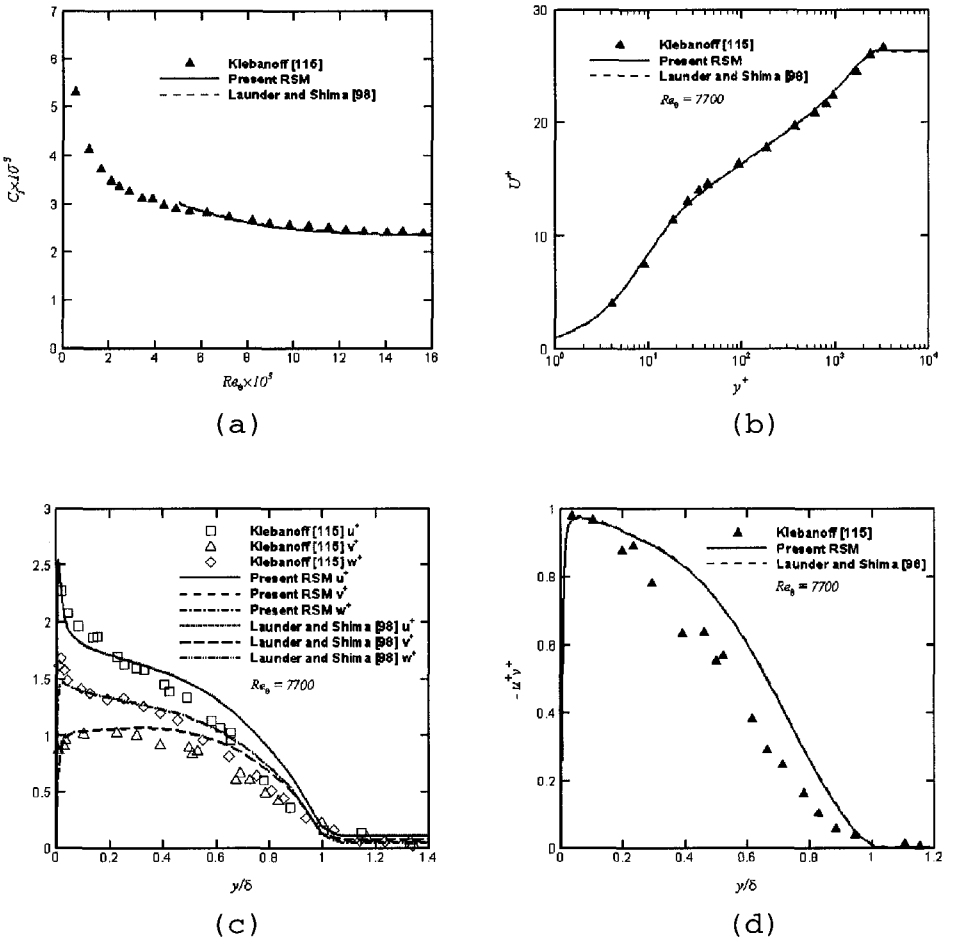

Figure 36. Comparisons of (a) the skin friction coefficient (b) the log-law velocity (c) the turbulence intensities and (d) the Reynolds shear stress in a smooth wall turbulent boundary layer.

Rough channel flows

The fully developed rough channel flows of Bakken et al. [19] are calculated. Two different rough surfaces (Figure 22), i.e., square rod roughness of $k_s^+ = 107$ ($k_{eq}^+ = 834.6$) and mesh roughness of $k_s^+ = 83$ ($k_{eq}^+ = 273.9$), were

examined. The Reynolds numbers, based on the channel height, are 60,000 and 62,000 for the square rod and the mesh roughness, respectively. The porosity is calculated based on the volumetric characteristics of the roughness. The total stress method is used to determine the friction velocity u_τ, as shown in Eq. (5.31). The calculated distribution of the log-law velocity, the Reynolds stresses, and the turbulent kinetic energy across the channel are shown.

Square Rod Roughness: Bakken et al.[19]

For the square rod roughness shown in Figure 22(b), the porosity is calculated using Eq. (5.35) with k_s = $0.017H$ and λ = $0.136H$ [19]. The resulting porosity and Darcy number are 0.875 and 1.539×10^{-10}, respectively. Figure 37 shows calculated profiles of the log-law velocity, the Reynolds stresses and the turbulent kinetic energy, comparing with the numerical predictions from the present TEM, and the measurements. It can be observed from Figure 37(a) that the log-law velocity profiles predicted from both models have good agreement with the experimental data. It is shown in Figure 37(b) that the predictions of v^{+2} and w^{+2} from the present RSM agree well with the experimental data for the outer region of $y/(H/2) > 0.2$. The present RSM underpredicts u^{+2} comparing to the experimental data for outer region of $y/(H/2)$ >

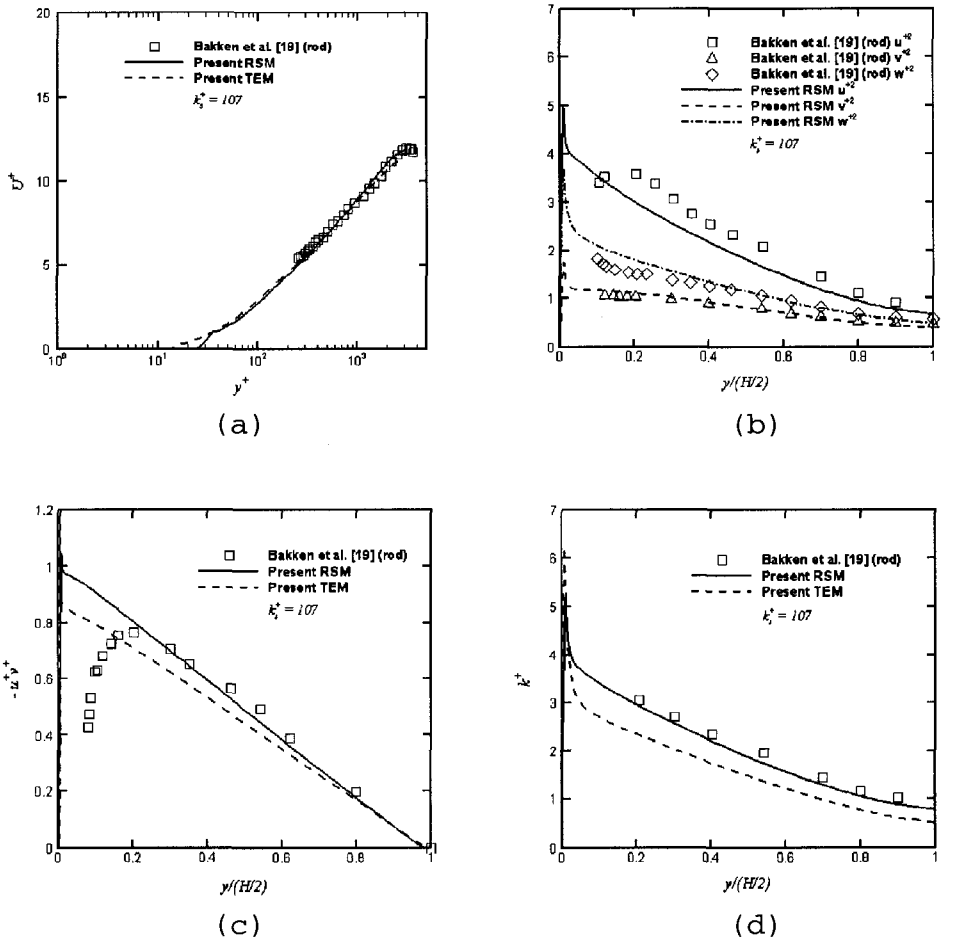

Figure 37. Comparisons of (a) the log-law velocity (b) the Reynolds normal stresses (c) the Reynolds shear stress and (d) the turbulence kinetic energy in rough channel flows with square rod roughness.

0.2, yet broadly follow the trend of the data. The computational results corresponding to the Reynolds shear stress and the turbulent kinetic energy comparing with the numerical predictions from the present TEM and experimental measurements are shown in Figure 37(c) and

Figure 37(d), respectively. It can be observed from Figure 37(c) that the predicted Reynolds shear stress profile from the present RSM agrees better than that from the present TEM for the outer region of $y/(H/2) > 0.2$. In the inner region of $y/(H/2) < 0.2$, the peak level of the measured Reynolds shear stress profile is lower than the predictions. The reduced peak Reynolds shear stress has been attributed to the local flow acceleration ahead of and above the rod roughness [19]. It is shown in Figure 37(d) that the predictions of the turbulent kinetic energy from the present RSM agree with the data, while the present TEM underpredicts the turbulent kinetic energy for the outer region of $y/(H/2) > 0.2$.

Mesh Roughness: Bakken et al. [19]

For the type of mesh roughness shown in Figure 22(a), the porosity can be calculated using Eq. (5.32) with $k_s = 0.015H$, $\lambda = 0.12H$, and $b = 0.02H$ [19]. The resulting porosity and Darcy number are 0.694 and 8.498×10^{-10}, respectively. The computational results corresponding to the log-law velocity and the Reynolds stresses are shown in Figure 38. It can be observed from Figure 38(a) that log-law velocity profiles predicted from both models have good agreements with the experimental data. Figure 38(b) and Figure 38(c) show the computed Reynolds normal stresses and the Reynolds shear

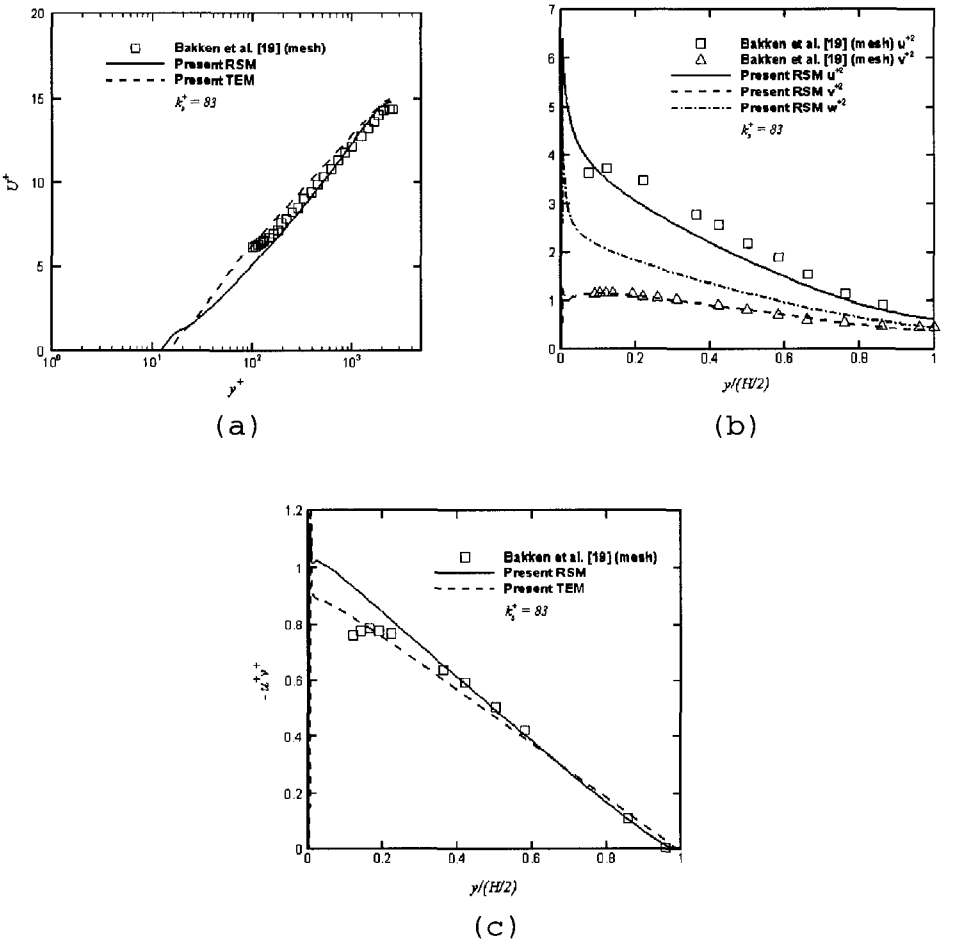

Figure 38. Comparisons of (a) the log-law velocity, (b) the Reynolds normal stresses and (c) the Reynolds shear stress in rough channel flows with mesh roughness.

stress comparing with the experimental data, respectively. The comparisons of the Reynolds normal stresses profiles show the overall trends being very similar to the case with the square rod roughness (Figure 37(b)). It is shown in Figure 38(c) that both models predict well the Reynolds shear stress profiles for the

outer region of $y/(H/2) > 0.2$ comparing to the experimental data [19].

Turbulent boundary layers over rough plates

The turbulent boundary layers over flat plates with different types of surface roughness were calculated. They include woven mesh [13,20], cylinder [43], square rod [27], and perforated plate [16]. The roughness Reynolds number k_s^+ ranges between 94.6 and 150. Based on the geometry of the roughness elements and their formations provided by the corresponding experimental measurements, the porosity ε_β for these different types of surface roughness vary from 0.398 to 0.898. Comparisons of the log-law velocity, the Reynolds shear stress, and the turbulent kinetic energy across the turbulent boundary layers are shown.

Woven Mesh Roughness: Antonia and Krogstad [13]

For the woven mesh roughness of k_s = 1.38 *mm* and k_s^+ = 94.6 (k_{eq}^+ = 340) shown in Figure 25, the porosity is calculated using Eq. (5.36) with λ = 3.18 *mm*, and d_w = 0.69 *mm* [13]. The resulting porosity ε_β = 0.83 and *Da* = 6.30×10^{-13}. The experiment study was conducted at a Reynolds number, based on the plate length, of 4.62×10^6, and the data were measured at Re_θ = 12,800.

The comparison results of the calculated log-law

velocity, the Reynolds stresses, and the turbulent kinetic energy with those by using the present TEM and the experimental measurements are provided in Figure 39. It is shown in Figure 39(a) that both models predict well the log-law velocity in the log-law region and outer layer region comparing to the experiment data. The

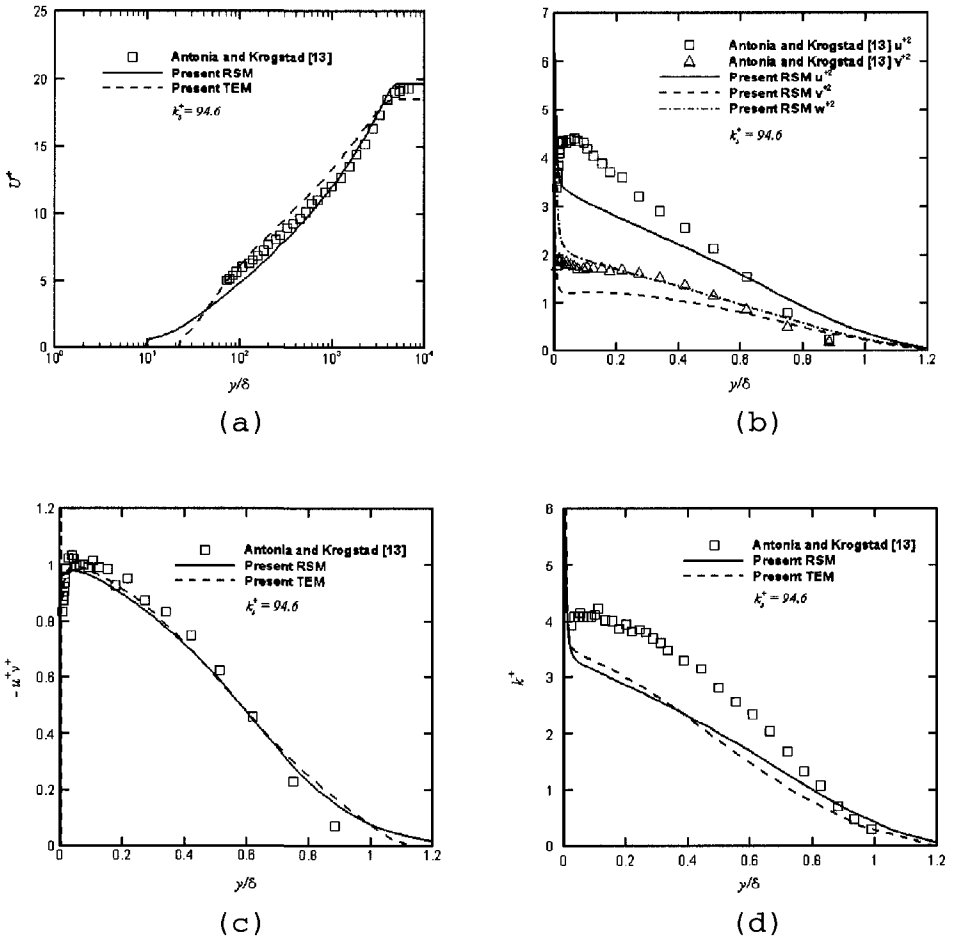

Figure 39. Comparisons of (a) the log-law velocity (b) the Reynolds normal stresses (c) the Reynolds shear stress and (d) the turbulence kinetic energy at Re_θ = 12,800 in turbulent boundary layer with surface roughness of mesh screen.

difference in the skin friction coefficient between the present RSM calculations and the measurements is about 1.5%, compared to about 4.5% for that by the present TEM calculations. It is shown in Figure 39(b) that the present RSM less satisfactorily predicts u^{+2} and v^{+2} across the boundary comparing to the experimental data, yet the predictions of the Reynolds shear stress from both models agree with the experimental data, and broadly follow the trend of the experimental data as shown in Figure 39(c). As mentioned earlier in Chapter V, the present RSM employed an interface condition [81,82] that characterizes the slip velocity at the top of the modeled roughness region by a jump of the velocity gradient across the interface. Except for nearing the interface, the present RSM describes a much reduced turbulent momentum transport in the modeled roughness layer which essentially maintains the same level of the Reynolds stresses in the roughness region. Turbulent fluctuations are mostly dampened in the roughness region. It is reasonable to expect that this damping effect, as is reflected in the present RSM results, lessens near the interface where the flow motion is far less restricted. It is shown in Figure 39(d) that both models less satisfactorily predict the turbulent kinetic energy across the boundary layer.

Woven Mesh Roughness: Flack et al. [20]

For the woven mesh roughness of k_s = 1.40 *mm* and k_s^+ = 150 (k_{eq}^+ = 370), similar to that shown in Figure 25, the porosity is calculated using Eq. (5.36) with λ / d_w = 4.58 [20]. The resulting porosity ε_β = 0.829 and *Da* = 8.943×10^{-13}. The experimental study of Flack et al. [20] was conducted at a Reynolds number, based on the plate length, of 2.7×10^6, and the data were measured at Re_θ = 9110.

The computed mean velocity and the Reynolds stresses are shown in Figure 40. It can be observed from Figure 40(a) that the mean velocity profiles predicted by both models agree well with the experimental data in the log-law and the outer layer regions. It can be observed from Figure 40(b) that the predictions of u^{+2} and v^{+2} from the present RSM agree well with the experimental data for the outer region of y/δ > 0.4, yet the present RSM underpredicts the components of the Reynolds normal stress of u^{+2} and v^{+2} comparing to the experimental data in the inner region of y/δ < 0.4. It is shown in Figure 40(c) that the simulation results of both models show that the Reynolds shear stress profiles generally follow the trend of the experimental data and are in good agreement with the data across the turbulent boundary layer.

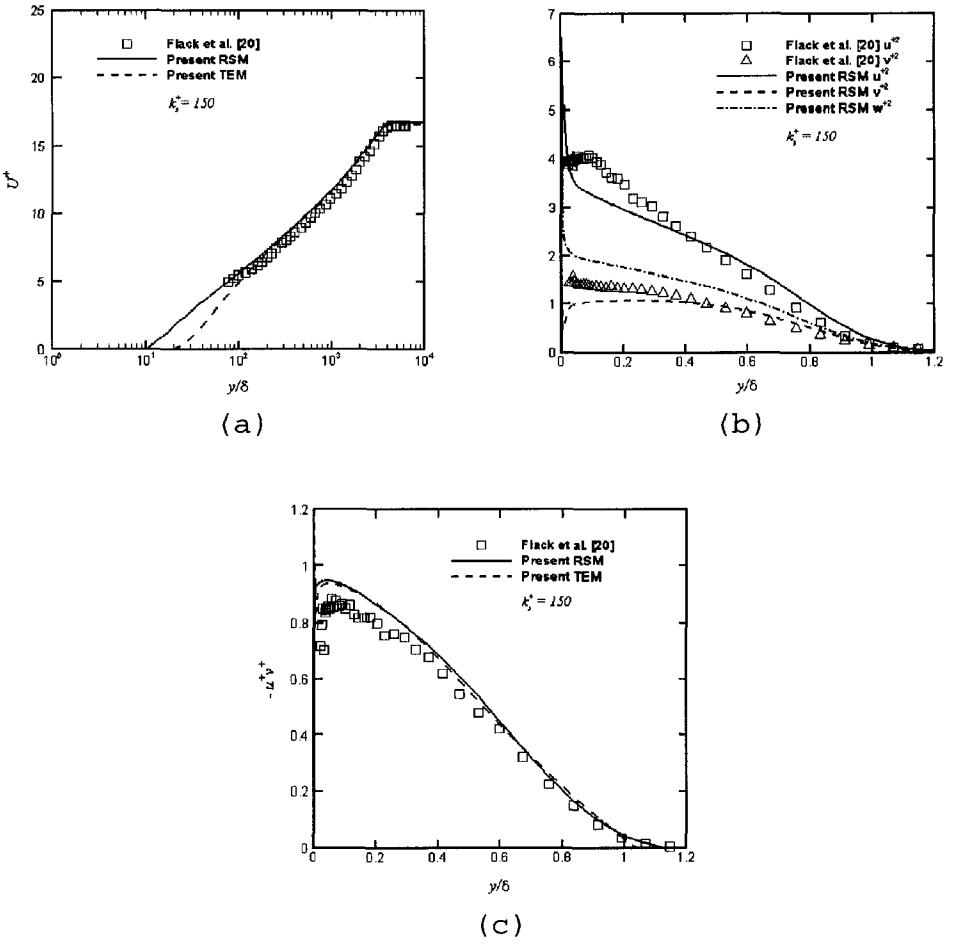

Figure 40. Comparisons of (a) the log-law velocity, (b) the Reynolds normal stresses and (c) the Reynolds shear stress at Re_θ = 9110 in turbulent boundary layer with surface roughness of woven mesh.

Cylinder Roughness: George and Simpson [43]

For the cylinder roughness of k_s = 1.52 *mm* and k_s^+ = 128 shown in Figure 28, the porosity can be calculated using Eq. (5.37) with λ = 5.486 *mm* and d_c = 1.98 *mm* [43].

The resulting porosity ε_β = 0.898 and Da = 7.853×10^{-14}. The experimental study of George and Simpson [43] was conducted at a Reynolds number, based on the plate length, of 4.82×10^{6}, and the data were measured at the half spacing λ location directly behind the cylinder.

It is shown in Figure 41(a) that the simulation results of the log-law mean velocity from both models agree with the experimental data in the log-law region at Re_θ = 13,789. The present RSM provides the better prediction in the outer region than that of the present TEM. As the data were taken directly behind a cylinder roughness, a small reverse flow region is measured. It can be observed from Figure 41(b) that the present RSM underpredicts all three components of the Reynolds normal stress, u^{+2}, v^{+2}, and w^{+2}, across the entire boundary layer comparing to the experimental data. The computed Reynolds shear stress and the turbulent kinetic energy are shown in Figure 41(c) and Figure 41(d), respectively. It can be observed from Figure 41(c) that the predicted Reynolds shear stress profiles from both models agree well with the experimental data in the region where y/δ > 0.1. For the turbulent kinetic energy as shown in Figure 41(d), the calculated distributions from both models are less satisfactorily. The measured Reynolds stresses and turbulent kinetic energy profiles show enhanced peaks

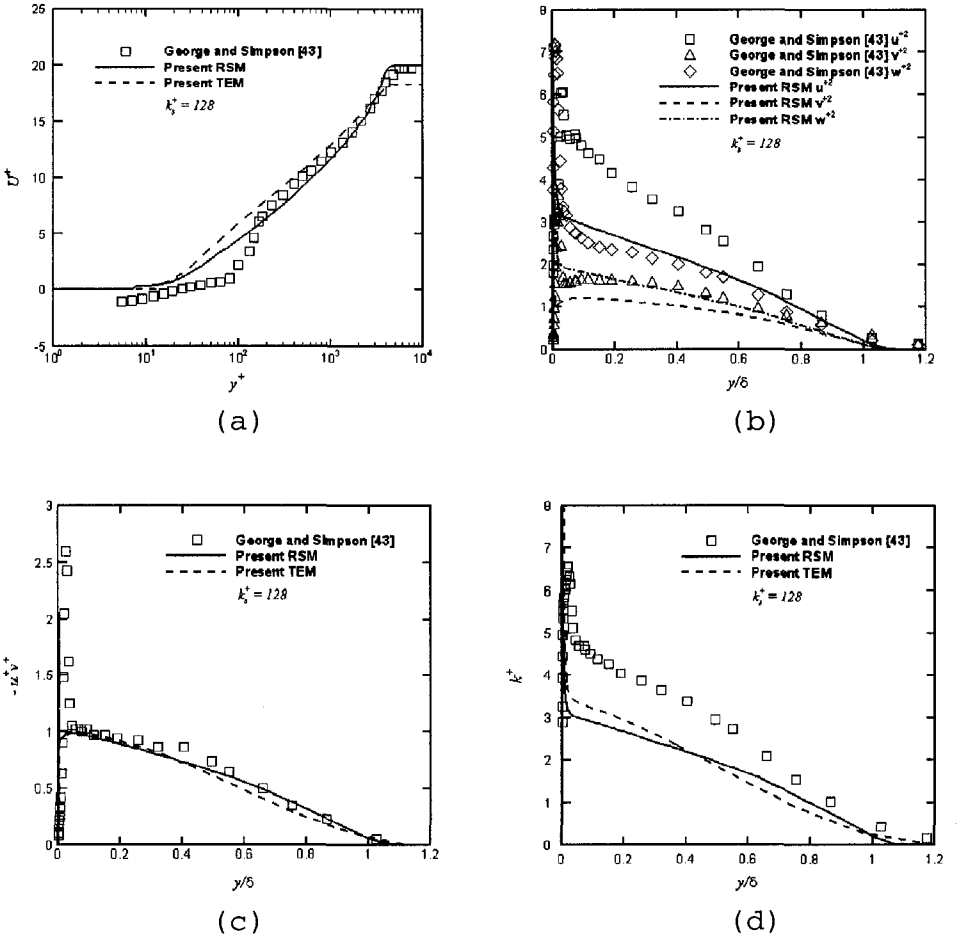

Figure 41. Comparisons of (a) the log-law velocity (b) the Reynolds normal stresses (c) the Reynolds shear stress and (d) the turbulence kinetic energy at Re_θ = 13,789 in turbulent boundary layer with surface roughness of cylinders.

near the top of the cylinder roughness. Arguably the shear-production mechanism associated with the flow around a roughness element is generally captured in the present modeling approach in an (volume) average manner.

Square Rod Roughness: Keirsbulck et al. [27]

For the square rod roughness of k_s = 3 *mm* and k_s^+ = 150, similar to that shown in Figure 22(b), the porosity is calculated using Eq. (5.35) with λ = 10 *mm* [27]. The resulting porosity ε_β = 0.7 and *Da* = 1.334×10^{-12}. The experimental study of Keirsbulck et al. [27] was conducted at a Reynolds number, based on the plate length, of 3.94×10^6, and the data were measured at Re_θ = 8549. The computed mean velocity and the Reynolds stresses are shown in Figure 42. The mean velocity profiles predicted by both models agree well with the experimental data in the log-law layer region and in the outer layer region. It can be observed from Figure 42(b) that the present RSM predicts well the Reynolds normal stress components of u^{+2} for the region y/δ > 0.2, and v^{+2} for the region y/δ > 0.4 comparing to the experimental data, yet underpredicts u^{+2} and v^{+2} in the inner region of y/δ < 0.2. It is shown in Figure 42(c) that predicted Reynolds shear stress profiles from both models agree well with the experimental data for the region of y/δ > 0.6. The present RSM provides the better prediction of the Reynolds shear stress profile than that of the present TEM comparing to the experimental data for the region of 0.3 < y/δ < 0.6. The measured peak Reynolds shear stress level is lower than that calculated and

decreases at a faster rate toward the wall than reported for other types of roughness in boundary layers [13,20,43].

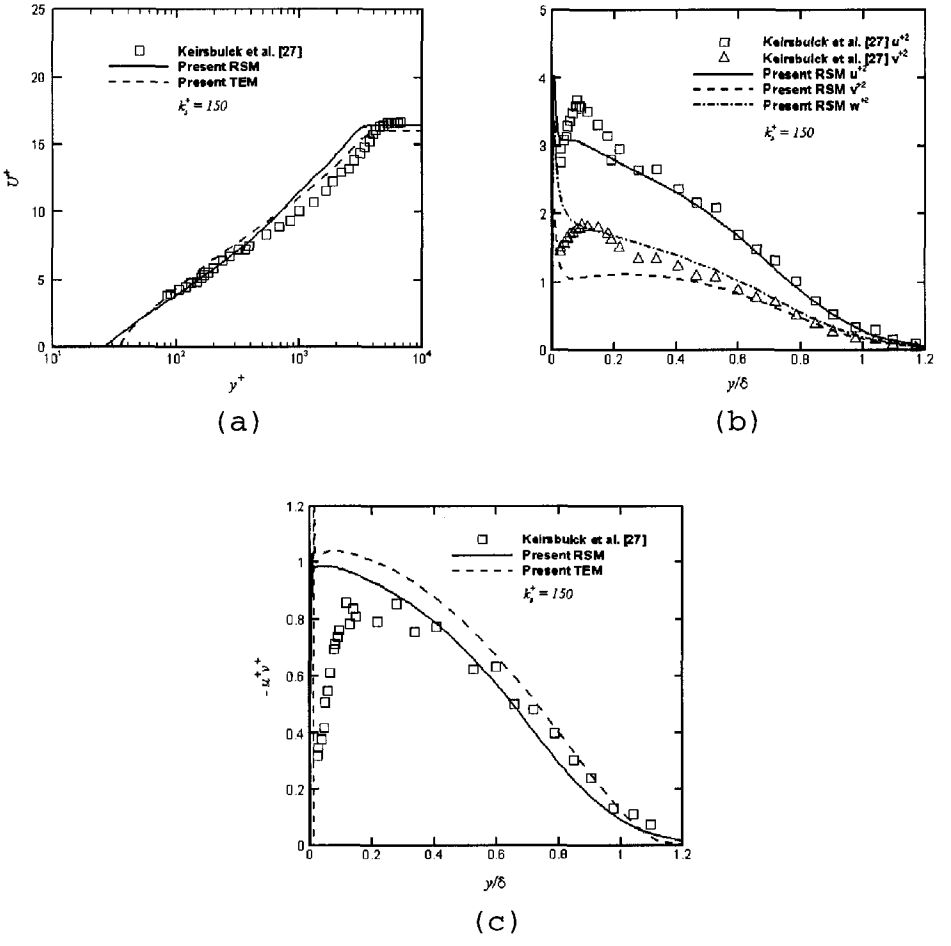

Figure 42. Comparisons of (a) the log-law velocity, (b) the Reynolds normal stresses and (c) the Reynolds shear stress at Re_θ = 8549 in turbulent boundary layer with square rod roughness.

Perforated Plate Roughness: Bergstrom et al. [16]

For the perforated plate roughness of k_s = 0.9 mm and

k_s^+ = 122 (k_{eq}^+ = 149) as shown in Figure 31, the porosity can be calculated using Eq. (5.38) with λ = 2.81 *mm* and d_h = 2 *mm* [16]. The resulting porosity ε_β = 0.398 and *Da* = 3.3487×10^{-13}. The experiment was conducted at a Reynolds number, based on the plate length, of 4.44×10^6, and is among the few available experimental measurements that provide the streamwise variation of skin friction coefficient. For the experimental study [16], the skin friction coefficient is calculated in the constant total stress layer using Eq. (5.34), which is also used in the present RSM to determine the skin friction coefficient.

The computed streamwise development of the skin friction coefficients are presented in Figure 43. Both the models predict well the skin friction coefficient

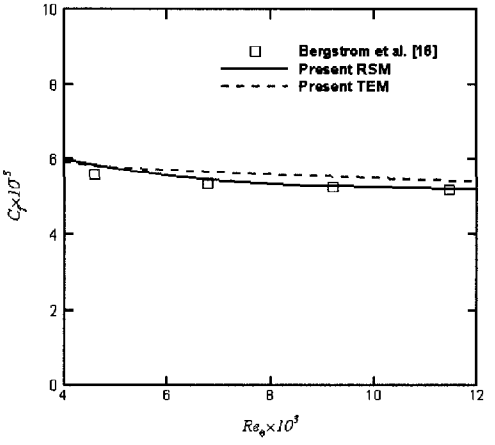

Figure 43. Predictions of the skin friction coefficients in turbulent boundary layer with surface roughness of perforated plate.

changes in the streamwise direction. The differences between the predictions and measurements are about 0.5% for the present RSM at Re_θ = 11,460, and is about 4% for the present TEM. The profiles of the log-law velocity at Re_θ = 11,460 are compared in Figure 44. It is shown that the predictions from both models agree well with the data in the log-law and the outer layer regions.

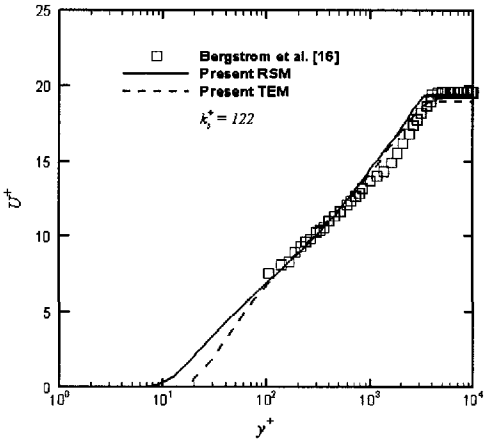

Figure 44. Comparisons of the log-law velocity at Re_θ = 11,460 in turbulent boundary layer with surface roughness of perforated plate.

In the above, the results of the present RSM for seven different rough-wall cases have been shown. The results were compared individually with those reported in the corresponding experimental studies. To provide an overall comparison, in Figure 45, the calculated roughness functions ΔU^+, determined using Eq. (5.33), for

all of these different cases are plotted versus their equivalent sand roughness k_{eq}^{+} and compared with Prandtl and Schlichting [3]. The roughness functions predicted by both models agree well with Prandtl and Schlichting [3] over the entire range of k_{eq}^{+} calculated. In addition, in the region where the k_{eq}^{+} for rough channel flows overlaps with that for rough-wall boundary layers, the predictions consistently agree with Prandtl and Schlichting [3]. It indicates that the present modeling approach that accounts explicitly for the geometry and the formation of the roughness element can lead to more consistent and reliable predictions of the mean flow.

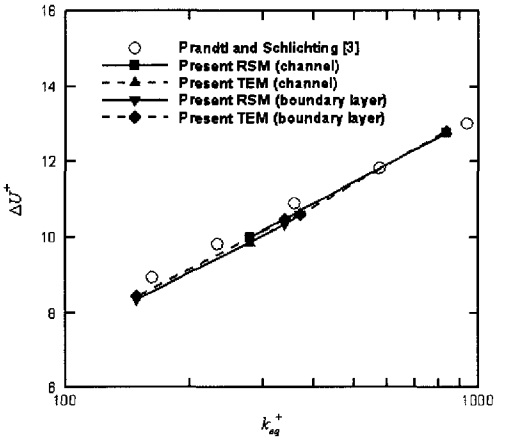

Figure 45. Comparisons of the roughness functions in terms of equivalent sand roughness heights.

Concluding remarks

A new second-order turbulence closure for the new

flow physics-based surface roughness model is developed for the RANS numerical calculations of the high-Reynolds-number turbulent flows over rough walls. For the mean flow in the roughness region, the volume average method is used and the proposed modeling framework results in the Brinkman equation. The porosity ε_β used in the Brinkman equation is obtained based on the geometry and the formation of the surface roughness. For the closure of the turbulent quantities, a second-order Reynolds stress model was developed using a baseline, smooth wall turbulence model of Launder and Shima [98]. The developed model is examined by simulating fully developed turbulent rough channel flows for the square rod and the mesh roughness measured by Bakken et al. [19] with the roughness Reynolds number k_s^+ of 83 and 107, respectively. Rough wall turbulent boundary layers with surface roughness of woven mesh [13,20], cylinder [43], square rod [27], and perforated plate [16] with the roughness Reynolds number k_s^+ ranging between 94.6 and 150 are also studied. The values of the porosity ε_β for these different types of surface roughness vary from 0.398 to 0.898. Based on the results reported, for the different roughness, we found that

(1) the present RSM predicts well the skin friction coefficient, the log-law mean velocity, and the roughness function for the calculated fully developed turbulent

rough channel flows and the rough wall turbulent boundary layers over different types of surface roughness;

(2) the predicted Reynolds shear stress profiles generally agree well with the experimental data in the outer layer region for the calculated fully developed turbulent rough channel flows and the rough wall turbulent boundary layers over different types of surface roughness;

(3) the calculated Reynolds normal stresses and the turbulent kinetic energy agree less satisfactorily with experimental measurements of Antonia and Krogstad [13] and George and Simpson [43] in turbulent boundary layers over rough walls.

The proposed roughness modeling approach takes into account explicitly the effect of the formation and the topographical characteristics of the roughness and resolves the fluid dynamics of the averaged flow in the roughness region using the Brinkman equation. The results show that for the case presented, the new physics-based modeling approach with a second-order Reynolds stress model can also lead to a consistent and reliable modeling of the mean flow for a wide range of roughness type.

CHAPTER VII

CONCLUSIONS

In light of the practical importance of the surface roughness effects in many engineering problems, there is a need to develop mathematical models for RANS-type calculations, which allows for predictive calculations of such flows. It is proposed herein to use the Brinkman equation to model the averaged flow in the surface roughness layer of the turbulent boundary layer due to the geometric and the dynamic similarities between the porous medium flow and the surface roughness flow. The proposed exploratory use of the Brinkman equation is innovative, since this widely used approach in porous medium flow calculations has never been applied to the modeling of the rough wall effects on high-Reynolds-number flows.

The main research objectives were to develop a new flow physics-based surface roughness modeling that can be employed in the RANS numerical calculations of the high-Reynolds-number flows over a wide range of rough surfaces. The developed roughness modeling improves the current predictive capability of the roughness effects. The main results and conclusions of this research are

recapitulated in the following sections.

Rough wall layer modeling equations

In the mathematical formulation of the Brinkman equation modeling approach described in Chapter II, the time- and volume-averaged model equations for the mean flows are derived and turbulence transport equations are developed based on existing smooth wall turbulence closures. The roughness-related model parameters, such as effective diameter d_p, roughness region thickness δ_B, model constants C_{ε_3} and C_3, are also introduced.

For the mean flow, the fluid dynamics of the averaged flow is resolved using the Brinkman equation. Turbulence model of Launder and Sharma [97] for a two-equation closure and Launder and Shima [98] for a second-order closure are adopted for solving the turbulent quantities. The interface conditions of Ochoa-Tapia and Whitaker [81,82] are adopted for the averaged flow properties. The interface stress jump conditions of Silva and de Lemos [78] are employed for a two-equation turbulence closure, while new stress jump conditions including the Reynolds stress components are developed for a second-order turbulence closure. The interface conditions enforced the continuity of velocity, pressure, and turbulence properties, and the stress jump at the interface between the roughness and the free flow

regions.

Assessment of existing RANS-type rough wall models

In Chapter IV, the performance of two existing RANS-type rough wall low-Reynolds-number $k-\varepsilon$ models, Zhang et al. [66] (ZH) and Foti and Scandura [67] (FS), has been assessed by simulating the fully developed turbulent flow in rough pipes, rough channels and over rough plates. The predictions of the two models are examined against the published experimental measurements with the equivalent sand roughness k_{eq}^{+} ranging from 26.6 to 834.6.

The FS model predicts reasonably well the log-law mean velocity profiles and the roughness function ΔU^{+} for all of the flows calculated, while the predictions of those from the ZH model are only satisfactory for low roughness height of $k_{eq}^{+} < 30$. In general, both models predict well the Reynolds shear stress profiles comparing to the experimental data, yet predict less satisfactorily the skin friction coefficient and the turbulent kinetic energy in the turbulent boundary layers over rough walls.

The results of Chapter IV, which examines only flows with simple geometries, suggest that there is a need for roughness modeling that can consistently predict the effect of roughness on not only the mean flow, but also the turbulence quantities in the RANS framework. Modeling may be developed that includes consideration of the

interactions of the flow structures and roughness. Such physics-based modeling approaches may lead to more consistent and reliable predictions of turbulent flows over roughness.

A new rough wall layer modeling approach

A new flow physics-based surface roughness model is developed for the RANS numerical calculations of the high-Reynolds-number turbulent flows over rough walls. For the mean flow in the roughness region, the fluid dynamics of the time- and volume-averaged flow in the near-wall rough layer is modeled by using the Brinkman equation. The porosity used in the Brinkman equation is obtained based on the geometry and the formation of the surface roughness. The roughness-related model parameters, d_p and δ_B, are propose to relate with the physical roughness height, k_s. This provides a direct link between the physical length scale and that needed for the modeling.

The developed model is examined by simulating fully developed turbulent rough channel flows for the mesh and the square rod roughness measured by Bakken et al. [19], and rough wall turbulent boundary layers with surface roughness of woven mesh [13,20], cylinder [43], square rod [27], and perforated plate [16] in the fully rough regime. The values of the porosity for these different

types of surface roughness vary from 0.398 to 0.898.

Two-equation closure

In Chapter V, the proposed roughness modeling approach incorporates roughness-related closures to an existing, smooth wall, low-Reynolds-number $k - \varepsilon$ model of Launder and Sharma [97] and is employed to resolve the turbulent quantities in both the roughness and the free flow regions. The results show that the proposed roughness modeling approach with a two-equation closure predicts well the skin friction coefficient, the log-law mean velocity, and the roughness function, yet less satisfactorily predicts the turbulent kinetic energy in the fully developed turbulent rough channel flows and turbulent boundary layers over rough walls.

The proposed roughness modeling approach takes into account explicitly the effect of the formation and the topographical characteristics of the roughness and resolves the fluid dynamics of the averaged flow in the roughness region using the Brinkman equation. The results indicate that for all the cases presented, the new physics-based modeling approach can lead to a consistent and reliable modeling of the mean flow for a wide range of roughness type.

Second-order closure

In Chapter VI, the second-order Reynolds stress model of Launder and Shima [98] is adopted to the proposed rough wall layer modeling approach, that has a consistent and reliable modeling of the mean flow for a wide range of roughness type with a two-equation turbulence closure. The results show that the proposed roughness modeling approach with a second-order closure predicts well the skin friction coefficient, the log-law mean velocity, and the roughness function for the calculated fully developed turbulent rough channel flows and the rough wall turbulent boundary layers over different types of surface roughness. The predicted Reynolds shear stress profiles generally agree well with the experimental data in the outer layer region, yet the calculated Reynolds normal stresses and the turbulent kinetic energy agree less satisfactorily with experimental measurements of Antonia and Krogstad [13] and George and Simpson [43] in turbulent boundary layers over rough walls.

The results show that for the case presented, the new physics-based modeling approach with a second-order Reynolds stress model can also lead to a consistent and reliable modeling of the mean flow for a wide range of roughness type.

In summary, the developed rough wall layer modeling approach improves the current predictive capability of the roughness effects, and is applicable to a wider range of surface roughness.

Recommendations for future research

Complex geometries with surface roughness

We have successfully developed a new flow physics-based surface roughness modeling to be used in the RANS numerical calculations of the high-Reynolds-number flows over rough surfaces. The developed rough wall layer modeling approach improves the current predictive capability of the roughness effects, and is applicable to a wider range of surface roughness. In this dissertation, only turbulent rough-wall flows with simple geometries were examined. The next step will be employed this new flow physics-based surface roughness modeling on the turbulent flows over complex geometries with surface roughness.

Optimizations of modeling constants and parameters

In Chapter II, the values of model constants, C_{ε_3} in Eq. (2.38) and C_{ε_3} in Eq. (2.44), for drag force terms in turbulence transport equation of ε are set to be 0.11. The interface stress jump parameters, β_t and β_n, are set

based on generally accepted values of β_t = -1 and β_n = 5. Those values of model constants and parameters have not been selected nor optimized for the calculations results shown here. The further investigations will be performed to obtain the optimized values for those model constants and parameters.

Rough wall layer modeling approach using LES

In this dissertation, a RANS-type roughness modeling approach is developed and validated with experimental measurements in turbulent boundary layer flows over rough walls. A natural extension of our research is employing the same roughness modeling approach in LES.

Appendix A

Derivation of the volume-averaged dispersive stress equations

To derive the budget equations for the volume-averaged dispersive stress equations in intrinsic form of $\langle u_i'' u_j'' \rangle^\beta$, we first assume the Navier-Stokes equation operator as

$$N(u_i) = \frac{\partial u_i}{\partial t} + u_k \frac{\partial u_i}{\partial x_k} + \frac{1}{\rho} \frac{\partial P}{\partial x_i} - \nu \frac{\partial^2 u_i}{\partial x_k^2} \tag{A.1}$$

Then we apply

$$\langle u_i'' N(u_j) + u_j'' N(u_i) \rangle^\beta = 0 \tag{A.2}$$

The unsteady term:

$$\begin{aligned}
\langle u_i'' \frac{\partial u_j}{\partial t} + u_j'' \frac{\partial u_i}{\partial t} \rangle^\beta &= \langle u_i'' \frac{\partial \left(\langle u_j \rangle^\beta + u_j'' \right)}{\partial t} + u_j'' \frac{\partial \left(\langle u_i \rangle^\beta + u_i'' \right)}{\partial t} \rangle^\beta \\
&= \langle u_i'' \frac{\partial \langle u_j \rangle^\beta}{\partial t} \rangle^\beta + \langle u_i'' \frac{\partial u_j''}{\partial t} \rangle^\beta \\
&\quad + \langle u_j'' \frac{\partial \langle u_i \rangle^\beta}{\partial t} \rangle^\beta + \langle u_j'' \frac{\partial u_i''}{\partial t} \rangle^\beta \\
&= \langle u_i'' \frac{\partial u_j''}{\partial t} \rangle^\beta + \langle u_j'' \frac{\partial u_i''}{\partial t} \rangle^\beta \\
&= \frac{\partial \langle u_i'' u_j'' \rangle^\beta}{\partial t}
\end{aligned} \tag{A.3}$$

The pressure gradient term:

$$
\begin{aligned}
\langle u_i'' \frac{1}{\rho}\frac{\partial P}{\partial x_j} + u_j'' \frac{1}{\rho}\frac{\partial P}{\partial x_i}\rangle^\beta &= \langle u_i'' \frac{1}{\rho}\frac{\partial\left(P + P''\right)}{\partial x_j} + u_j'' \frac{1}{\rho}\frac{\partial\left(P + P''\right)}{\partial x_i}\rangle^\beta \\
&= \frac{1}{\rho}\left(\langle u_i'' \frac{\partial P''}{\partial x_j}\rangle^\beta + \langle u_j'' \frac{\partial P''}{\partial x_i}\rangle^\beta\right) \\
&= \frac{1}{\rho}\left(\langle\frac{\partial u_i'' P''}{\partial x_j}\rangle^\beta + \langle\frac{\partial u_j'' P''}{\partial x_i}\rangle^\beta\right) \\
&\quad - \frac{1}{\rho}\langle P''\left(\frac{\partial u_i''}{\partial x_j} + \frac{\partial u_j''}{\partial x_i}\right)\rangle^\beta \\
&= \frac{1}{\rho}\left(\frac{\partial\langle u_i'' P''\rangle^\beta}{\partial x_j} + \frac{\partial\langle u_j'' P''\rangle^\beta}{\partial x_i}\right) \\
&\quad + \frac{1}{\Delta V_\beta}\int_{A_i}\left[\frac{P''}{\rho}\left(n_j u_i'' + n_i u_j''\right)\right]dA \\
&\quad - \frac{1}{\rho}\langle P''\left(\frac{\partial u_i''}{\partial x_j} + \frac{\partial u_j''}{\partial x_i}\right)\rangle^\beta
\end{aligned}
\tag{A.4}
$$

The convective term:

$$
\begin{aligned}
\langle u_i'' u_k \frac{\partial u_j}{\partial x_k} + u_j'' u_k \frac{\partial u_i}{\partial x_k}\rangle^\beta &= \langle u_i''\left(\langle u_k\rangle^\beta + u_k''\right)\frac{\partial\left(\langle u_j\rangle^\beta + u_j''\right)}{\partial x_k}\rangle^\beta \\
&\quad + \langle u_j''\left(\langle u_k\rangle^\beta + u_k''\right)\frac{\partial\left(\langle u_i\rangle^\beta + u_i''\right)}{\partial x_k}\rangle^\beta \\
&= \langle u_i''\langle u_k\rangle^\beta \frac{\partial u_j''}{\partial x_k}\rangle^\beta + \langle u_i'' u_k'' \frac{\partial\left(\langle u_j\rangle^\beta + u_j''\right)}{\partial x_k}\rangle^\beta \\
&\quad + \langle u_j''\langle u_k\rangle^\beta \frac{\partial\tilde{u}_i}{\partial x_k}\rangle^\beta + \langle u_j'' u_k'' \frac{\partial\left(\langle u_i\rangle^\beta + u_i''\right)}{\partial x_k}\rangle^\beta \\
&= \langle u_k\rangle^\beta \frac{\partial\langle u_i'' u_j''\rangle^\beta}{\partial x_k} + \langle u_i'' u_k''\rangle^\beta \frac{\partial\langle u_j\rangle^\beta}{\partial x_k} \\
&\quad + \langle u_j'' u_k''\rangle^\beta \frac{\partial\langle u_i\rangle^\beta}{\partial x_k} + \frac{\partial\langle u_i'' u_j'' u_k''\rangle^\beta}{\partial x_k}
\end{aligned}
\tag{A.5}
$$

The viscous diffusion term:

$$
\begin{aligned}
\langle -u_i''\nu\frac{\partial^2 u_j}{\partial x_k^2} - u_j''\nu\frac{\partial^2 u_i}{\partial x_k^2}\rangle^\beta &= -\nu\langle u_i''\frac{\partial^2\left(\langle u_j\rangle^\beta + u_j''\right)}{\partial x_k^2} - u_j''\frac{\partial^2\left(\langle u_i\rangle^\beta + u_i''\right)}{\partial x_k^2}\rangle^\beta \\
&= -\nu\langle u_i''\frac{\partial^2 u_j''}{\partial x_k^2}\rangle^\beta - \nu\langle u_j''\frac{\partial^2 u_i''}{\partial x_k^2}\rangle^\beta \\
&= -\nu\langle\frac{\partial}{\partial x_k}\left(u_j''\frac{\partial u_i''}{\partial x_k} + u_i''\frac{\partial u_j''}{\partial x_k}\right)\rangle^\beta + 2\nu\langle\frac{\partial u_i''}{\partial x_k}\frac{\partial u_j''}{\partial x_k}\rangle^\beta \\
&= -\nu\frac{\partial^2\langle u_i''u_j''\rangle^\beta}{\partial x_k^2} \\
&\quad -\frac{1}{\Delta V_\beta}\int_{A_i}\left[\nu\left(u_j''\frac{\partial u_i''}{\partial n} + u_i''\frac{\partial u_j''}{\partial n}\right)\right]dA \\
&\quad + 2\nu\langle\frac{\partial u_i''}{\partial x_k}\frac{\partial u_j''}{\partial x_k}\rangle^\beta \qquad \text{(A.6)}
\end{aligned}
$$

Substitution of Eqs. (A.3)-(A.6) into Eq. (A.2) gives the budget equations for the volume-averaged dispersive stress equations in intrinsic form of $\langle\tilde{u}_i\tilde{u}_j\rangle^\beta$ as follows,

$$
\begin{aligned}
\frac{\partial\langle u_i''u_j''\rangle^\beta}{\partial t} + \langle u_k\rangle^\beta\frac{\partial\langle u_i''u_j''\rangle^\beta}{\partial x_k} &= -\left[\langle u_i''u_k''\rangle^\beta\frac{\partial\langle u_j\rangle^\beta}{\partial x_k} + \langle u_j''u_k''\rangle^\beta\frac{\partial\langle u_i\rangle^\beta}{\partial x_k}\right] \\
&\quad -\frac{1}{\rho}\left(\frac{\partial\langle P''u_i''\rangle^\beta}{\partial x_j} + \frac{\partial\langle P''u_j''\rangle^\beta}{\partial x_i}\right) \\
&\quad -\frac{\partial\langle u_i''u_j''u_k''\rangle^\beta}{\partial x_k} + \frac{1}{\rho}\langle P''\left(\frac{\partial u_i''}{\partial x_j} + \frac{\partial u_j''}{\partial x_i}\right)\rangle^\beta \\
&\quad + \nu\frac{\partial^2\langle u_i''u_j''\rangle^\beta}{\partial x_k^2} - 2\nu\langle\frac{\partial u_i''}{\partial x_k}\frac{\partial u_j''}{\partial x_k}\rangle^\beta \\
&\quad + \frac{1}{\Delta V_\beta}\int_{A_i}\left[-\frac{P''}{\rho}\left(n_j u_i'' + n_i u_j''\right)\right]dA \\
&\quad + \frac{1}{\Delta V_\beta}\int_{A_i}\left[\nu\left(u_j''\frac{\partial u_i''}{\partial n} + u_i''\frac{\partial u_j''}{\partial n}\right)\right]dA \qquad \text{(A.7)}
\end{aligned}
$$

Eq. (A.7) is basically the same as that derived by Wang

and Takle [73], except for not considering the effect of the Coriolis and buoyance forces in this study. For $i = j$, we have transport equation for $e^{\beta} = \frac{1}{2}\langle \tilde{u}_i \tilde{u}_i \rangle^{\beta}$ as follows,

$$\frac{\partial e^{\beta}}{\partial t} + \langle u_k \rangle^{\beta} \frac{\partial e^{\beta}}{\partial x_k} = - \langle u_i'' u_k'' \rangle^{\beta} \frac{\partial \langle u_i \rangle^{\beta}}{\partial x_k} - \frac{1}{\rho} \frac{\partial \langle P'' u_i'' \rangle^{\beta}}{\partial x_i} - \frac{\partial \frac{1}{2} \langle u_i'' u_i'' u_k'' \rangle^{\beta}}{\partial x_k} + \nu \frac{\partial^2 e^{\beta}}{\partial x_k^2} - \nu \langle \frac{\partial u_i''}{\partial x_j} \frac{\partial u_i''}{\partial x_j} \rangle^{\beta} + \frac{1}{\Delta V_{\beta}} \int_{A_i} \left[- \frac{P''}{\rho} n_i u_i'' + \nu u_i'' \frac{\partial u_i''}{\partial n} \right] dA \qquad (A.8)$$

The budget equations for the volume-averaged dispersive stress equations in superficial form of $\langle \tilde{u}_i \tilde{u}_j \rangle$ can be obtained as follows,

$$\frac{\partial \langle u_i'' u_j'' \rangle}{\partial t} + \frac{1}{\varepsilon_{\beta}} \langle u_k \rangle \frac{\partial \langle u_i'' u_j'' \rangle}{\partial x_k} = - \frac{1}{\varepsilon_{\beta}} \left[\langle u_i'' u_k'' \rangle \frac{\partial \langle u_j \rangle}{\partial x_k} + \langle u_j'' u_k'' \rangle \frac{\partial \langle u_i \rangle}{\partial x_k} \right] - \frac{1}{\rho} \left(\frac{\partial \langle P'' u_i'' \rangle}{\partial x_j} + \frac{\partial \langle P'' u_j'' \rangle}{\partial x_i} \right) - \frac{\partial \langle u_i'' u_j'' u_k'' \rangle}{\partial x_k} + \frac{1}{\rho} \langle P'' \left(\frac{\partial u_i''}{\partial x_j} + \frac{\partial u_j''}{\partial x_i} \right) \rangle + \nu \frac{\partial^2 \langle u_i'' u_j'' \rangle}{\partial x_k^2} - 2\nu \langle \frac{\partial u_i''}{\partial x_k} \frac{\partial u_j''}{\partial x_k} \rangle + \frac{1}{\Delta V} \int_{A_i} \left[- \frac{P''}{\rho} \left(n_j u_i'' + n_i u_j'' \right) \right] dA + \frac{1}{\Delta V} \int_{A_i} \left[\nu \left(u_j'' \frac{\partial u_i''}{\partial n} + u_i'' \frac{\partial u_j''}{\partial n} \right) \right] dA \qquad (A.9)$$

The transport equation for $e = \frac{1}{2}\langle u_i'' u_i'' \rangle$ can be obtained

when $i = j$ in Eq. (A.9) as follows,

$$\frac{\partial e}{\partial t} + \frac{1}{\varepsilon_\beta}\langle u_k\rangle\frac{\partial e}{\partial x_k} = -\frac{1}{\varepsilon_\beta}\langle u_i'' u_k''\rangle\frac{\partial\langle u_i\rangle}{\partial x_k} - \frac{1}{\rho}\frac{\partial\langle P'' u_i''\rangle}{\partial x_i} - \frac{\partial\,\frac{1}{2}\langle u_i'' u_i'' u_k''\rangle}{\partial x_k} + \nu\frac{\partial^2 e}{\partial x_k^2} - \nu\langle\frac{\partial u_i''}{\partial x_j}\frac{\partial u_i''}{\partial x_j}\rangle + \frac{1}{\Delta V}\int_{A_i}\left[-\frac{P''}{\rho}n_i u_i'' + \nu u_i''\frac{\partial u_i''}{\partial n}\right]dA \qquad (A.10)$$

Appendix B

Derivation of the volume- and time-averaged Reynolds stress equations

To derive the volume- and time-averaged Reynolds stress equations of $\langle\overline{u_i'u_j'}\rangle^\beta$, we apply the volume-average operator on the time-averaged Reynolds stress equations

$$\underbrace{\langle\frac{\partial\overline{u_i'u_j'}}{\partial t}\rangle^\beta}_{I} + \underbrace{\langle\overline{u}_k\frac{\partial\overline{u_i'u_j'}}{\partial x_k}\rangle^\beta}_{II} = \underbrace{-\left\langle\left(\overline{u_i'u_k'}\frac{\partial\overline{u}_j}{\partial x_k} + \overline{u_j'u_k'}\frac{\partial\overline{u}_i}{\partial x_k}\right)\right\rangle^\beta}_{III} \underbrace{-\langle\frac{\partial\overline{u_i'u_j'u_k'}}{\partial x_k}\rangle^\beta}_{IV}$$
$$\underbrace{-\langle\frac{1}{\rho}\left(\frac{\partial\overline{P'u_i'}}{\partial x_j} + \frac{\partial\overline{P'u_j'}}{\partial x_i}\right)\rangle^\beta}_{V} + \underbrace{\langle\overline{\frac{P'}{\rho}\left(\frac{\partial u_i'}{\partial x_j} + \frac{\partial u_j'}{\partial x_i}\right)}\rangle^\beta}_{VI}$$
$$\underbrace{+\langle\nu\frac{\partial^2\overline{u_i'u_j'}}{\partial x_k^2}\rangle^\beta}_{VII} \underbrace{-\langle 2\nu\overline{\left(\frac{\partial u_i'}{\partial x_k}\frac{\partial u_j'}{\partial x_k}\right)}\rangle^\beta}_{VIII} \qquad \text{(B.1)}$$

First noting that at interface A_i, $\overline{u}_i = u_i' = 0$.

The term *I*:

$$\langle\frac{\partial\overline{u_i'u_j'}}{\partial t}\rangle^\beta = \frac{1}{\Delta V_\beta}\int_{\Delta V_\beta}\frac{\partial\overline{u_i'u_j'}}{\partial t}dV$$
$$= \frac{\partial}{\partial t}\left\{\frac{1}{\Delta V_\beta}\int_{\Delta V_\beta}\overline{u_i'u_j'}dV\right\}$$
$$= \frac{\partial\langle\overline{u_i'u_j'}\rangle^\beta}{\partial t} \qquad \text{(B.2)}$$

The term *II*:

$$\langle \overline{u}_k \frac{\partial \overline{u_i' u_j'}}{\partial x_k} \rangle^\beta = \langle \left(\langle \overline{u}_k \rangle^\beta + \overline{u}_k'' \right) \frac{\partial \left(\langle \overline{u_i' u_j'} \rangle^\beta + \overline{u_i' u_j'}'' \right)}{\partial x_k} \rangle^\beta$$

$$= \langle \langle \overline{u}_k \rangle^\beta \frac{\partial \langle \overline{u_i' u_j'} \rangle^\beta}{\partial x_k} \rangle^\beta + \langle \langle \overline{u}_k \rangle^\beta \frac{\partial \overline{u_i' u_j'}''}{\partial x_k} \rangle^\beta$$

$$+ \langle \overline{u}_k'' \frac{\partial \langle \overline{u_i' u_j'} \rangle^\beta}{\partial x_k} \rangle^\beta + \langle \overline{u}_k'' \frac{\partial \overline{u_i' u_j'}''}{\partial x_k} \rangle^\beta$$

$$= \langle \overline{u}_k \rangle^\beta \frac{\partial \langle \overline{u_i' u_j'} \rangle^\beta}{\partial x_k} + \langle \overline{u}_k'' \frac{\partial \overline{u_i' u_j'}''}{\partial x_k} \rangle^\beta \qquad \text{(B.3)}$$

The term *III*:

$$- \langle \left(\overline{u_i' u_k'} \frac{\partial \overline{u}_j}{\partial x_k} + \overline{u_j' u_k'} \frac{\partial \overline{u}_i}{\partial x_k} \right) \rangle^\beta = - \langle \left(\langle \overline{u_i' u_k'} \rangle^\beta + \overline{u_i' u_k'}'' \right) \frac{\partial \left(\langle \overline{u}_j \rangle^\beta + \overline{u}_j'' \right)}{\partial x_k}$$

$$+ \left(\langle \overline{u_j' u_k'} \rangle^\beta + \overline{u_j' u_k'}'' \right) \frac{\partial \left(\langle \overline{u}_i \rangle^\beta + \overline{u}_i'' \right)}{\partial x_k} \rangle^\beta$$

$$= - \langle \langle \overline{u_i' u_k'} \rangle^\beta \frac{\partial \langle \overline{u}_j \rangle^\beta}{\partial x_k} - \langle \overline{u_i' u_k'}'' \frac{\partial \overline{u}_j''}{\partial x_k} \rangle^\beta$$

$$- \langle \overline{u_j' u_k'} \rangle^\beta \frac{\partial \langle \overline{u}_i \rangle^\beta}{\partial x_k} - \langle \overline{u_j' u_k'}'' \frac{\partial \overline{u}_i''}{\partial x_k} \rangle^\beta \qquad \text{(B.4)}$$

The term *IV*:

$$- \langle \frac{\partial \overline{u_i' u_j' u_k'}}{\partial x_k} \rangle^\beta = - \frac{\partial \langle \overline{u_i' u_j' u_k'} \rangle^\beta}{\partial x_k} + \frac{1}{\Delta V_\beta} \int_{A_i} n_i \overline{u_i' u_j' u_k'} dA$$

$$= - \frac{\partial \langle \overline{u_i' u_j' u_k'} \rangle^\beta}{\partial x_k} \qquad \text{(B.5)}$$

The term *V*:

$$-\langle\frac{1}{\rho}\left(\frac{\partial\overline{P'u_i'}}{\partial x_j}+\frac{\partial\overline{P'u_j'}}{\partial x_i}\right)\rangle^{\beta} = -\frac{1}{\rho}\left(\frac{\partial\langle\overline{P'u_i'}\rangle^{\beta}}{\partial x_j}+\frac{\partial\langle\overline{P'u_j'}\rangle^{\beta}}{\partial x_i}\right) - \frac{1}{\Delta V_{\beta}}\int_{A_i}\left[-\overline{\frac{P'}{\rho}\left(u_i'n_j+u_j'n_i\right)}\right]dA \quad (B.6)$$

The term *VII*:

$$\langle\nu\frac{\partial^2\overline{u_i'u_j'}}{\partial x_k^2}\rangle^{\beta} = \nu\frac{\partial^2\langle\overline{u_i'u_j'}\rangle^{\beta}}{\partial x_k^2}+\frac{1}{\Delta V_{\beta}}\int_{A_i}\left[\nu\left(\overline{u_j'\frac{\partial u_i'}{\partial n}+u_i'\frac{\partial u_j'}{\partial n}}\right)\right]dA \quad (B.7)$$

Substitution of Eqs. (B.2)-(B.7) into Eq. (B.1) gives the volume- and time-averaged Reynolds stress equations of $\langle\overline{u_i'u_j'}\rangle^{\beta}$ as follows,

$$\begin{aligned}\frac{\partial\langle\overline{u_i'u_j'}\rangle^{\beta}}{\partial t}+\langle\overline{u}_k\rangle^{\beta}\frac{\partial\langle\overline{u_i'u_j'}\rangle^{\beta}}{\partial x_k} = &-\left(\langle\overline{u_i'u_k'}\rangle^{\beta}\frac{\partial\langle\overline{u}_j\rangle^{\beta}}{\partial x_k}+\langle\overline{u_j'u_k'}\rangle^{\beta}\frac{\partial\langle\overline{u}_i\rangle^{\beta}}{\partial x_k}\right)\\ &-\frac{\partial\langle\overline{u_i'u_j'u_k'}\rangle^{\beta}}{\partial x_k}+\langle\overline{\frac{P'}{\rho}\left(\frac{\partial u_i'}{\partial x_j}+\frac{\partial u_j'}{\partial x_i}\right)}\rangle^{\beta}\\ &-\frac{1}{\rho}\left(\frac{\partial\langle\overline{P'u_i'}\rangle^{\beta}}{\partial x_j}+\frac{\partial\langle\overline{P'u_j'}\rangle^{\beta}}{\partial x_i}\right)+\nu\frac{\partial^2\langle\overline{u_i'u_j'}\rangle^{\beta}}{\partial x_k^2}\\ &-2\nu\langle\overline{\frac{\partial u_i'}{\partial x_k}\frac{\partial u_j'}{\partial x_k}}\rangle^{\beta}-\langle\overline{u}_k''\frac{\partial\overline{u_i'u_j'}''}{\partial x_k}\rangle^{\beta}\\ &-\left(\langle\overline{u_i'u_k'}''\frac{\partial\overline{u}_j''}{\partial x_k}\rangle^{\beta}+\langle\overline{u_j'u_k'}''\frac{\partial\overline{u}_i''}{\partial x_k}\rangle^{\beta}\right)\\ &+\frac{1}{\Delta V_{\beta}}\int_{A_i}\left[-\overline{\frac{P'}{\rho}\left(u_i'n_j+u_j'n_i\right)}\right]dA\\ &+\frac{1}{\Delta V_{\beta}}\int_{A_i}\left[\nu\left(\overline{u_j'\frac{\partial u_i'}{\partial n}+u_i'\frac{\partial u_j'}{\partial n}}\right)\right]dA \quad (B.8)\end{aligned}$$

Eq. (B.8) is basically the same as that derived by Brunet et al. [72]. Comparing to the conventional time-averaged Reynolds stress equations, the last four terms in the right-hand side of Eq. (B.8) are the extra terms resulting from both volume- and time-averaged.

The volume- and time-averaged Reynolds stress equations in superficial form of $\langle\overline{u_i'u_j'}\rangle$ can be obtained as follows,

$$\begin{aligned}
\frac{\partial\langle\overline{u_i'u_j'}\rangle}{\partial t} + \frac{1}{\varepsilon_\beta}\langle\overline{u}_k\rangle\frac{\partial\langle\overline{u_i'u_j'}\rangle}{\partial x_k} = & -\frac{1}{\varepsilon_\beta}\left(\langle\overline{u_i'u_k'}\rangle\frac{\partial\langle\overline{u}_j\rangle}{\partial x_k} + \langle\overline{u_j'u_k'}\rangle\frac{\partial\langle\overline{u}_i\rangle}{\partial x_k}\right) \\
& - \frac{\partial\langle\overline{u_i'u_j'u_k'}\rangle}{\partial x_k} - \frac{1}{\rho}\left(\frac{\partial\langle\overline{P'u_i'}\rangle}{\partial x_j} + \frac{\partial\langle\overline{P'u_j'}\rangle}{\partial x_i}\right) \\
& + \langle\overline{\frac{P'}{\rho}\left(\frac{\partial u_i'}{\partial x_j} + \frac{\partial u_j'}{\partial x_i}\right)}\rangle + \nu\frac{\partial^2\langle\overline{u_i'u_j'}\rangle}{\partial x_k^2} \\
& - 2\nu\langle\overline{\frac{\partial u_i'}{\partial x_k}\frac{\partial u_j'}{\partial x_k}}\rangle - \langle\overline{u}_k''\frac{\partial\overline{u_i'u_j'}''}{\partial x_k}\rangle \\
& - \left(\langle\overline{u_i'u_k'}''\frac{\partial\overline{u}_j''}{\partial x_k}\rangle + \langle\overline{u_j'u_k'}''\frac{\partial\overline{u}_i''}{\partial x_k}\rangle\right) \\
& + \frac{1}{\Delta V}\int_{A_i}\left[-\overline{\frac{P'}{\rho}\left(u_i'n_j + u_j'n_i\right)}\right]dA \\
& + \frac{1}{\Delta V}\int_{A_i}\left[\nu\overline{\left(u_j'\frac{\partial u_i'}{\partial n} + u_i'\frac{\partial u_j'}{\partial n}\right)}\right]dA \qquad \text{(B.9)}
\end{aligned}$$

The transport equation for $k = \frac{1}{2}\langle\overline{u_i'u_i'}\rangle$ can be obtained when $i = j$ in Eq. (B.9) as follows,

$$\frac{\partial k}{\partial t} + \frac{1}{\varepsilon_\beta}\langle \overline{u}_k \rangle \frac{\partial k}{\partial x_k} = -\frac{1}{\varepsilon_\beta}\langle \overline{u_i' u_k'} \rangle \frac{\partial \langle \overline{u}_i \rangle}{\partial x_k} - \frac{\partial \frac{1}{2}\langle \overline{u_i' u_j' u_k'} \rangle}{\partial x_k} - \frac{1}{\rho}\left(\frac{\partial \langle \overline{P' u_k'} \rangle}{\partial x_k} \right)$$
$$+ \nu \frac{\partial^2 k}{\partial x_k^2} - \nu \langle \overline{\frac{\partial u_i'}{\partial x_k} \frac{\partial u_i'}{\partial x_k}} \rangle$$
$$- \frac{1}{2}\langle \overline{u}_k'' \frac{\partial \overline{u_i' u_i'}''}{\partial x_k} \rangle - \langle \overline{u_i' u_k'}'' \frac{\partial \overline{u}_i''}{\partial x_k} \rangle$$
$$+ \frac{1}{\Delta V}\int_{A_i} \left[-\overline{\frac{P'}{\rho} u_i' n_i} + \nu \overline{u_i' \frac{\partial u_i'}{\partial n}} \right] dA \qquad \text{(B.10)}$$

Appendix C

Derivation of interface stress jump conditions for a second-order closure

In the homogeneous parts of the roughness and free flow regions, we present the governing equations (closure time-averaged VANS equations) by neglecting the left-hand side of Eq. (2.27).

Roughness region:

$$\frac{\partial \langle \overline{u}_i \rangle_R}{\partial x_i} = 0 \tag{C.1}$$

$$0 = -\frac{1}{\rho}\frac{\partial \langle \overline{P} \rangle_R^{\beta}}{\partial x_i} + \varepsilon_\beta^{-1}\nu \frac{\partial^2 \langle \overline{u}_i \rangle_R}{\partial x_j^2} - \varepsilon_\beta^{-1}\frac{\partial \langle \overline{u_i' u_j'} \rangle_R}{\partial x_j} + \overline{f}_i \tag{C.2}$$

Free flow region:

$$\frac{\partial \langle \overline{u}_i \rangle_F}{\partial x_i} = 0 \tag{C.3}$$

$$0 = -\frac{1}{\rho}\frac{\partial \langle \overline{P} \rangle_F^{\beta}}{\partial x_i} + \nu \frac{\partial^2 \langle \overline{u}_i \rangle_F}{\partial x_j^2} - \frac{\partial \langle \overline{u_i' u_j'} \rangle_F}{\partial x_j} \tag{C.4}$$

and boundary conditions at the interface are

$$\langle \overline{u}_i \rangle_R = \langle \overline{u}_i \rangle_F \tag{C.5}$$

$$\langle \overline{u_i' u_j'} \rangle_R = \langle \overline{u_i' u_j'} \rangle_F \tag{C.6}$$

$$\langle \overline{P} \rangle_R^\beta = \langle \overline{P} \rangle_F^\beta \tag{C.7}$$

To develop the interface jump condition, we form the volume integral, and subtract the momentum equation in free flow region, Eq. (C.4), from that in roughness region, Eq. (C.2). Assuming negligible excess stresses [81], we have

$$\mathbf{n}_{RF} \cdot \left[-\frac{1}{\rho} \mathbf{I} \left(\langle \overline{P} \rangle_R^\beta - \langle \overline{P} \rangle_F^\beta \right) + \nu \left(\varepsilon_\beta^{-1} \frac{\partial \langle \overline{u}_i \rangle_R}{\partial x_j} - \frac{\partial \langle \overline{u}_i \rangle_F}{\partial x_j} \right) - \left(\varepsilon_\beta^{-1} \langle \overline{u_i' u_j'} \rangle_R - \langle \overline{u_i' u_j'} \rangle_F \right) \right] = \nu \frac{\beta_{jump}}{\sqrt{K}} \cdot \langle \overline{u}_i \rangle_R \tag{C.8}$$

where $\mathbf{n}_{RF}$ is the unit normal vector directed from the roughness region to the free flow region, and β_{jump} is the dimensionless coefficient to be on the order of one.

Applying boundary condition of pressure, Eq. (C.7), at the interface, we can obtain

$$\mathbf{n}_{RF} \cdot \left[\nu \left(\varepsilon_\beta^{-1} \frac{\partial \langle \overline{u}_i \rangle_R}{\partial x_j} - \frac{\partial \langle \overline{u}_i \rangle_F}{\partial x_j} \right) - \left(\varepsilon_\beta^{-1} \langle \overline{u_i' u_j'} \rangle_R - \langle \overline{u_i' u_j'} \rangle_F \right) \right] = \nu \frac{\beta_{jump}}{\sqrt{K}} \cdot \langle \overline{u}_i \rangle_R \tag{C.9}$$

To consider streamwise velocity component and the

tangential stress, we have

$$\nu\left(\varepsilon_\beta^{-1}\frac{\partial\langle\overline{u}\rangle_R}{\partial y}-\frac{\partial\langle\overline{u}\rangle_F}{\partial y}\right)-\left(\varepsilon_\beta^{-1}\langle\overline{u'v'}\rangle_R-\langle\overline{u'v'}\rangle_F\right)=\nu\frac{\beta_t}{\sqrt{K}}\cdot\langle\overline{u}\rangle_R \quad \text{(C.10)}$$

For the wall-normal velocity component and stress, we get

$$\nu\left(\varepsilon_\beta^{-1}\frac{\partial\langle\overline{v}\rangle_R}{\partial y}-\frac{\partial\langle\overline{v}\rangle_F}{\partial y}\right)-\left(\varepsilon_\beta^{-1}\langle\overline{v'v'}\rangle_R-\langle\overline{v'v'}\rangle_F\right)=\nu\frac{\beta_n}{\sqrt{K}}\cdot\langle\overline{v}\rangle_R \quad \text{(C.11)}$$

where β_t and β_n are tangential and normal stress jump parameters, respectively.

BIBLIOGRAPHY

1. Nikuradse, J., (1933), "Laws of flow in rough pipes," NACA technical memorandum 1292.

2. Schlichting, H., (1960), Boundary Layer Theory, 4th Edition, McGraw Hill Book Company, New York.

3. Prandtl, L., and Schlichting, H., (1934), "Das wiederstandagesetz rouher platten," Werft Reederere Hafen, Vol. 15, pp. 1-4.

4. Colebrook, C.M., and White, C.M., (1937), "Experiments with fluid motion in roughened pipes," Proceedings of the Royal Society of London, Series A, Vol. 161, pp. 367-381.

5. Hama, F.R., (1954), "Boundary-layer characteristics for smooth and rough surfaces," Transactions./The Society of Naval Architecture and Marine Engineers, Vol. 62, pp. 333-358.

6. Laganelli, A.L., and Sontowski, J., (1982), "Prediction of skin friction with couple roughness and blowing based on transformation functions," AIAA paper 82-0033.

7. Dvorak, F.A., (1969), "Calculation of turbulent boundary layers on rough surfaces in pressure gradient," AIAA Journal, Vol. 7, No. 9, pp. 1752-1759.

8. Clauser, F.H., (1954), "Turbulent boundary layers in adverse pressure gradient," J. Aeronaut. Sci., Vol. 21, pp. 91-108.

9. Clauser, F.H., (1956), "Turbulent boundary layer," Adv. Appl. Mech., Vol. 4, pp.1-51.

10. Perry, A.E., Schofield W.H., and Joubert, P.N., (1969)," Rough wall turbulent boundary layer," Journal of Fluid Mechanics, Vol. 37, No. 2, pp. 383-413.

11. Raupach, M.R., Antonia, R.A., and Rajagopalan, S., (1991), "Rough-wall turbulent boundary layers," Appl. Mech. Rev., Vol. 44, No.2, pp.1-25.

12. Bandyopadhyay, P.R., (1987), "Rough-wall turbulent boundary layers in the transition regime," Journal of Fluid Mechanics, Vol. 180, pp. 231-266.

13. Antonia, R.A., and Krogstad, P.-Å., (2001), "Turbulence structure in boundary layers over different types of surface roughness," Fluid Dynamics Research, Vol. 28, No.2, pp. 139-157.

14. Schultz, M.P., and Flack, K.A., (2003), "Turbulent Boundary Layers over Surfaces Smoothed by Sanding," Transactions of the ASME, Journal of Fluids Engineering, Vol. 125, No. 5, pp. 863-870.

15. Akinlade, O.G., Bergstrom, D.J., Tachie, M.F., and Castillo L., (2004), "Outer flow scaling of smooth and rough wall turbulent boundary layers," Experiments in Fluids, Vol. 37, pp.604-612.

16. Bergstrom, D.J., Akinlade, O.G., and Tachie, M.F., (2005), " Skin friction correlation for smooth and rough wall turbulent boundary layers," Journal of Fluids Engineering, Vol. 127, No. 6, pp. 1146-1153.

17. Schultz, M.P., and Flack, K.A., (2005), "Outer layer similarity in fully rough turbulent boundary layers," Experiments in Fluids, Vol. 38, No. 3, pp. 328-340.

18. Flack, K.A., Schultz, M.P., and Shapiro, T.A., (2005), "Experimental support for Townsend's Reynolds number similarity hypothesis on rough walls," Physics of Fluids, Vol. 17, No. 3, pp. 035102-1-035102-9.

19. Bakken, O.M., Krogstad, P.-Å., Ashrafian, A., and Andersson, H.I., (2005), " Reynolds number effects in the outer layer of the turbulent flow in a channel with rough walls," Physics of Fluids, Vol. 17, No. 6, pp. 065101.

20. Flack, K.A., Schultz, M.P., and Connelly, J.A., (2007), "Examination of a critical roughness height for outer layer similarity," Physics of Fluids, Vol. 19, pp. 095104-9.

21. Brzek, B., Cal, R.B., Johansson, G., and Castillo, L., (2007), "Inner and outer scalings in rough surface zero pressure gradient turbulent boundary layers," Physics of Fluids, Vol. 19, No. 6, pp. 065101-17.

22. Townsend, A.A., (1976), The structure of turbulent shear flow, Cambridge University Press, Cambridge, UK.

23. Acharya, M., Bornstein, J., and Escudier, M.P., (1986), "Turbulent boundary layers on rough surfaces," Experiments in Fluids, Vol. 4, pp. 33-47.

24. Krogstad, P.-Å., Antonia, R.A., and Browne, L.W.B., "Comparison between rough- and smooth-wall turbulent boundary layers," Journal of Fluid Mechanics, Vol. 245, pp. 599-617, (1992).

25. Krogstad, P.-Å., and Antonia, R.A., (1994), "Structure of turbulent boundary layers on smooth and rough walls," Journal of Fluid Mechanics, Vol. 277, pp. 1-21.

26. Krogstad, P.-Å., and Antonia, R.A., (1999), "Surface roughness effects in turbulent boundary layers," Experiments in Fluids, Vol. 27, No. 5, pp. 450-460.

27. Keirsbulck, L., Labraga, L., Mazouz, A., and Tournier, C., (2002), "Surface roughness effects on turbulent boundary layer structures," Transactions of the ASME, Journal of Fluids Engineering, Vol. 124 , No. 1, pp. 127-135.

28. Poggi, D, Porporato, A., and Ridolfi, L., (2003), "Analysis of the small-scale structure of turbulence on smooth and rough walls," Physics of Fluids, Vol. 15, No. 1, pp. 35-46.

29. Patel, V.C., (1998), "Perspective: Flow at high Reynolds number and over rough surface-Achilles heel of CFD," Transactions of the ASME, Journal of Fluids Engineering, Vol. 120, pp. 434-444.

30. Wilcox, D.C., (1988), "Reassessment of the scale-determining equation for advanced turbulence models," AIAA Journal, Vol. 26, No. 11, pp. 1299-1310.

31. Durbin, P.A., Medic, G, Seo, J.-M., Eaton, J.K., and Song, S., (2001), "Rough wall modification of two-layer k-ε," Transactions of the ASME, Journal of Fluids Engineering, Vol. 123, pp. 16-21.

32. Chen, H.C., and Patel, V.C., (1988), "Near-wall turbulence models for complex flows including separation," AIAA Journal, Vol. 26, No.6, pp. 641-648.

33. Maruyama, T., (1993), "Optimization of roughness parameters for staggered arrayed cubic blocks using experimental data," Journal of Wind Engineering and Industrial Aerodynamics, Vol. 46-47, pp. 165-171.

34. Miyake, Y., Tsujimoto, K., and Agata, Y., (2000), "DNS of a turbulent flow in a rough-wall channel using roughness elements model," JSME International Journal, Series B, Vol. 43, No. 2, pp. 233-242.

35. Cui, J., Patel, V.C., and Lin, C., (2003), "Prediction of turbulent flow over rough surfaces using a force field in large eddy simulation," Transactions of the ASME, Journal of Fluids Engineering, Vol. 125, No. 1, pp. 2-9.

36. Finnigan, J., (2000), "Turbulence in plant canopies," Annual Review of Fluid Mechanics, Vol. 32, pp.519-571.

37. Jimenez, J., (2004), "Turbulent flows over rough walls," Annual Review of Fluid Mechanics, Vol. 36, pp. 173-196.

38. Rotta, J.C., (1962), Turbulent boundary layers in incompressible flow, Progress in Aeronautical Science, Pergamon, Oxford, pp. 1-220.

39. Wood, D.H., and Antonia, R.A., (1975), "Measurements of a turbulent boundary layer over a d-type surface roughness," J. Appl. Mech., Vol. 42, pp. 591-597.

40. Osaka, H., Nishino, T., Oyama, S., and Kageyama, Y., (1982), "Self-preservation for a turbulent boundary layer over a d-type rough surface," Memoirs of the Faculty of Engineering, Vol. 33, Yamaguchi University, pp. 9-16.

41. Tani, I., (1986), "Some equilibrium turbulent boundary layers," Fluid Dyn. Res., Vol. 1, pp. 49-58.

42. Connelly, J.S., Schultz, M.P., and Flack, K.A., (2006), "Velocity-defect scaling for turbulent boundary layers with a range of relative roughness," Experiments in Fluids, Vol. 40, No. 2, pp. 188-195.

43. George, J., and Simpson, R.L., (2004), "Transport-rate budgets of Reynolds stresses in 2-D and 3-D rough-wall turbulent boundary layers," AIAA Paper 2004-1286.

44. George, J., and Simpson, R.L., (2006), "Propagation of vorticity and turbulence in 2-D and 3-D rough-wall turbulent boundary layers," AIAA Paper 2006-0323.

45. Zagarola, M. V., and Smits, J., (1998), "A new mean velocity scaling for turbulent boundary layers," in Proceedings of FEDSM98-4950.

46. Bradshaw, P., (2000), "A note on 'critical roughness height' and 'transitional roughness'," Physics of Fluids, Vol. 12, No. 6, pp. 1611-1614.

47. Perry, A.E., and Li, J.D., (1990), "Experimental support for the attached-eddy hypothesis in zero-pressure-gradient turbulent boundary layers," Journal of Fluid Mechanics, Vol. 218, pp. 405-438.

48. Choi, K.S., and Fujisawa, N., (1993), "Possibility of drag reduction using d-type roughness," Applied Scientific Research, Vol. 50, No. 3-4, pp. 315-324.

49. Matsumoto, A., (1994), "Some features of turbulent boundary layers over grooved rough walls," Transactions of the Japan Society for Aeronautical and Space Sciences, Vol. 37, No. 115, pp. 27-41.

50. Djenidi, L, Antonia, R.A., and Anselmet, F., (1994), "LDA measurements in a turbulent boundary layer over a d-type rough wall," Experiments in Fluids, Vol. 16, No. 5, pp. 323-329.

51. Djenidi, L, Elavarasan, R., and Antonia, R.A., (1999), "The turbulent boundary layer over transverse square cavities," Journal of Fluid Mechanics, Vol. 395, pp. 253-270.

52. Miyake, Y., Tsujimoto, K., and Nakaji, M., (2001), "Direct numerical simulation of rough-wall heat transfer in a turbulent channel flow," International Journal of Heat and Fluid Flow, Vol. 22, No. 3, pp. 237-244.

53. Li, A., and Shao, Y., (2003), "Numerical simulation of drag partition over rough surfaces," Boundary-Layer Meteorology, Vol. 108, No. 3, pp. 317-342.

54. Scotti, A., (2006), "Direct numerical simulation of turbulent channel flows with boundary roughened with virtual sandpaper," Physics of Fluids, Vol. 18, No. 3, pp. 031701.

55. Goldstein, D., Handler, R., and Sirovich, L., (1995), "Direct numerical simulation of turbulent flow over a modelled riblet covered surface," Journal of Fluid Mechanics, Vol. 302, pp. 333-376.

56. Lee, C., (2002), "Large-eddy simulation of rough-wall turbulent boundary layers," AIAA Journal, Vol. 40, No. 10, pp. 2127-2130.

57. Bhaganagar, K., Kim, J., and Coleman, G., (2004), "Effect of roughness on wall-bounded turbulence," Flow, Turbulence and Combustion, Vol. 72, No. 2-4 SPEC. ISS., pp. 463-492.

58. Taylor, R.P., Coleman, H.W., and Hodge, B.K., (1985), "Prediction of turbulent rough-wall skin friction using a discrete element approach," Transactions of the ASME, Journal of Fluids Engineering, Vol. 107, No. 2, pp. 251-257.

59. Taylor, R.P., Scaggs, W.F., and Coleman, H.W., (1988), "Measurement and prediction of the effects of nonuniform surface roughness on turbulent flow friction coefficients," Transactions of the ASME, Journal of Fluids Engineering, Vol. 110, pp. 380-384.

60. Taylor, R.P., Hodge, B.K., and Coleman, H.W., (1989), "Discrete element model for turbulent skin friction prediction for rib-type surface roughness," Heat and Technology, Vol. 7, No. 1, pp. 29-48.

61. Tarada, F., (1990), "Prediction of rough-wall boundary layers using a low Reynolds number $k-\varepsilon$ model," International Journal of Heat and Fluid Flow, Vol. 11, No. 4, pp. 331-345.

62. Maruyama, T., (1999), "Surface and inlet boundary conditions for the simulation of turbulent boundary layer over complex rough surfaces," Journal of Wind Engineering and Industrial Aerodynamics, Vol. 81, pp. 311-322.

63. Yamamoto, M., (2003), "Proposal of a RANS model to predict both k- and d-type roughness," Proceedings of the 4th ASME/JSME Joint Fluids Engineering Conference: Volume 1, Part C, Forums, pp. 2019-2024.

64. Krogstad, P.-Å., (1991), "Modification of the van Driest damping function to include the effects of

surface roughness," AIAA Journal, Vol. 29, No. 6, pp. 888-894.

65. Youn, B., Yuen, C., and Mills, A.F., (1994), "Friction factor for flow in rectangular ducts with one side rib-roughened," Transactions of the ASME, Journal of Fluids Engineering, Vol. 116, No. 3, pp. 488-493.

66. Zhang, H., Faghri, M., and White, F.M., (1996), "New low-Reynolds-number $k-\varepsilon$ model for turbulent flow over smooth and rough surfaces," Transactions of the ASME, Journal of Fluids Engineering, Vol. 118, No. 2, pp. 255-259.

67. Foti, E., and Scandura, P., (2004), "A low Reynolds number $k-\varepsilon$ model validated for oscillatory flows over smooth and rough wall," Coastal Engineering, Vol. 51, No. 2, pp. 173-184.

68. van Driest, E.R., (1956), "On turbulent flow near a wall," Journal of Aerospace Science, Vol. 23, pp. 1007-1011.

69. Lam, C.K.G., and Bremhorst, K., (1981), "A modified form of the $k-\varepsilon$ model for predicting wall turbulence," Transactions of the ASME, Journal of Fluids Engineering, Vol. 103, No. 3, pp. 456-460.

70. Scheidegger, A.E., (1974), The Physics of Flow Through Porous Media, University of Toronto Press, Toronto.

71. Brinkman, H.C., (1948), "A calculation of the viscous force exerted by a flowing fluid on a dense swarm of particles," Applied Scientific Research, A 1, 27-34.

72. Brunet, Y., Finnigan, J.J., and Raupach, M.R., (1994), "A wind tunnel study of air flow in waving wheat single-point velocity statistics," Boundary-Layer Meteorology, Vol. 70, No. 1, pp. 95-132.

73. Wang, H., and Takle, E.S., (1995), "Boundary-layer flow and turbulence near porous obstacles. I. Derivation of a general equation set for a porous medium," Boundary-Layer Meteorology, Vol. 74, No. 1-2, pp. 73-88.

74. Antohe, B.V., and Lage, J.L., (1997), "A general two-equation macroscopic turbulence model for incompressible flow in porous media," International

Journal of Heat and Mass Transfer, Vol. 40, No. 13, pp. 3013-3024.

75. Ayotte, K.W., Finnigan, J.J, and Rupch, M.R., (1999), "A second-order closure for neutrally stratified vegetative canopy flows," Boundary-Layer Meteorology, Vol. 90, pp.189-216.

76. Getachew, D., Minkowycz, W.J., and Lage, J.L., (2000), "Modified form of the $k-\varepsilon$ model for turbulent flows of an incompressible fluid in porous media," International Journal of Heat and Mass Transfer, Vol. 43, No. 16, pp. 2909-2915.

77. Pedras, M.H.J., and de Lemos, M.J.S., (2001), "Macroscopic turbulence modeling for incompressible flow through undefromable porous media," International Journal of Heat and Mass Transfer, Vol. 44, No. 6, pp. 1081-1093.

78. Silva, R.A., and de Lemos, M.J.S., (2003), "Turbulent flow in a channel occupied by a porous layer considering the stress jump at the interface," International Journal of Heat and Mass Transfer, Vol. 46, No. 26, pp. 5113-5121.

79. Breugem, W.P., (2004), "The influence of wall permeability on laminar and turbulent flows," Ph.D. dissertation, Technische Universiteit Delft.

80. de Lemos, M.J.S., and Silva, R.A., (2006), "Turbulent flow over a layer of a highly permeable medium simulated with a diffusion-jump model for the interface," International Journal of Heat and Mass Transfer, Vol. 49, No. 3-4, pp. 546-556.

81. Ochoa-Tapia, J.A., and Whitaker, S., (1995), "Momentum transfer at the boundary between a porous medium and a homogeneous fluid - I. Theoretical development," International Journal of Heat and Mass Transfer, Vol. 38, No. 14, pp. 2635-2646.

82. Ochoa-Tapia, J.A., and Whitaker, S., (1995), "Momentum transfer at the boundary between a porous medium and a homogeneous fluid - II. Comparison with experiment," International Journal of Heat and Mass Transfer, Vol. 38, No. 14, pp. 2647-2655

83. Koplik, J., Levine, H., and Zee, A., (1983), "Viscosity renormalization in the Brinkman equation," Physics of Fluids, Vol. 26, No. 10, pp. 2864-2870.

84. Kaviany, M., (1985), "Laminar flow through a porous channel bounded by isothermal parallel plates," International Journal of Heat and Mass Transfer, Vol. 28, pp. 851-858.

85. Durlofsky, L., and Brady, J.F., (1987), "Analysis of the Brinkman equation as a model for flow in porous media," Physics of Fluids, Vol. 30, No. 11, pp. 3329-3341.

86. Renken, K.J., and Carneiro, M.J., (1992), "Effect of forced convection on enhanced film condensation within thin porous coatings," American Society of Mechanical Engineers, Heat Transfer Division, (Publication) HTD, Vol. 216, Heat and Mass Transfer in Porous Media, pp 27-34.

87. Goyeau, B., Songbe, J.-P., and Gobin, D., (1996), " Numerical study of double-diffusive natural convection in a porous cavity using the Darcy-Brinkman formulation," International Journal of Heat and Mass Transfer, Vol. 39, No. 7, pp. 1363-1378.

88. Kuznetsov, A.V., and Xiong, M., (2000), "Numerical simulation of the effect of thermal dispersion on forced convection in a circular duct partly filled with a Brinkman-Forchheimer porous medium," International Journal of Numerical Methods for Heat and Fluid Flow, Vol. 10, No. 5, pp. 488-501.

89. Martys, N.S., (2002), "Improved approximation of the Brinkman equation using a lattice Boltzmann method," Physics of Fluids, Vol. 13, No. 6, pp. 1807-1810.

90. Parvazinia, M., Nassehi, V., Wakeman, R.J., and Ghoreishy, M.H.R., (2006), "Finite element modelling of flow through a porous medium between two parallel plates using the Brinkman equation," Transport in Porous Media, Vol. 63, No. 1, pp. 71-90.

91. Beavers, G.S., and Joseph, D.D., (1967), "Boundary conditions at a naturally permeable wall," Journal of Fluid Mechanics, Vol. 30, pp. 197-207.

92. Chellaiah, S., and Viskanta, R., (1989), "Freezing of water-saturated porous media in the presence of natural convection: Experiments and analysis,"

Journal of Heat Transfer, Vol. 111, No. 2, pp. 425-432.

93. Kladias, N., and Prasad, V., (1991), "Experimental verification of Darcy-Brinkman-Forchheimer flow model for natural convection in porous media," Journal of Thermophysics and Heat Transfer, Vol. 5, No. 4, pp. 560-576.

94. Zhong, W.H., Currie, I.G., and James, D.F., (2006), "Creeping flow through a model fibrous porous medium," Experiments in Fluids, Vol. 40, No. 1, pp. 119-126.

95. Shukla, J.B., (1978), "A new theory of lubrication for roughness," Wear, Vol. 49, No. 1, pp. 33-42.

96. Tichy, J.A., (1995), "Porous media model for thin film lubrication," Journal of Tribology, Vol. 117, pp. 16-21.

97. Launder, B.E., and Sharma, B.I., (1974), "Application of the energy-dissipation model of turbulence to the calculation of flow near a spinning disc," Letters in Heat and Mass Transfer, Vol. 1, 1974, pp. 131-138.

98. Launder, B.E., and Shima, N., (1989), "Second-moment closure for the near-wall sublayer: development and application," AIAA Journal, Vol. 27, No. 10, pp. 1319-1325.

99. Whitaker, S., (1999), The Method of Volume Averaging, Kluwer, Dordrecht.

100. Hsu, C.T., and Cheng, P.,(1990), "Thermal dispersion in a porous medium," Int. J. Heat Mass Transfer, Vol. 33, pp. 1587-1597.

101. Carbonell, R.G., and Whitaker, S., (1984), "Heat and mass transport in porous media," NATO ASI Series, Series E: Applied Sciences, No. 82, pp. 121-198.

102. Pedras, M.H.J., and de Lemos, M.J.S., (2000), "On the definition of turbulent kinetic energy for flow in porous media," International Communications in Heat and Mass Transfer, Vol. 27, No. 2, pp. 211-220.

103. Whitaker, S., (1996), "Forchheimer equation: A theoretical development," Transport in Porous Media, Vol. 25, No. 1, pp. 27-61.

104. Hanjalic, K., and Launder, B.E., (1976), "Contribution towards a Reynolds-stress closure for low-Reynolds-number turbulence," Journal of Fluid Mechanics, Vol. 74, pp. 593-610.

105. Sotiropoulos, F., and Abdallah, S., (1992), "A Primitive variable method for the solution of three-dimensional incompressible viscous flows," Journal of Computational Physics, Vol. 103, pp. 336-349.

106. Sotiropoulos, F., and Abdallah, S., (1991), "The discrete continuity equation in primitive variable solutions of incompressible flow," Journal of Computational Physics, Vol. 95, pp. 212-227.

107. Kunz, R.F., and Lakshminarayana, B., (1992), "Three-dimensional Navier-Stokes computation of turbomachinery flows using an explicit numerical procedure and a coupled $k-\varepsilon$ turbulence model," Journal of Turbomachinery, Vol. 114, No. 3, pp. 627-642

108. Jameson, A., and Baker, T.J, (1983), "Solution of the Euler equations for complex configurations," AIAA Paper 83-1929.

109. Hollander, H., Lerat, A., and Peyret, R., (1985), "Three-dimensional calculation of transonic viscous flows by an implicit method," AIAA Journal, Vol. 23, No. 11, pp. 1670-1678.

110. Martinelli, L., (1987), "Calculation of viscous flows with multigrid methods," Ph.D. dissertation, Department of Mechanical and Aerospace Engineering, Princeton University.

111. Radiespiel, R., Rossow, C., Swanson, R., (1990), "Efficient cell-vertex multigrid scheme for the three-dimensional Navier-Stokes equations," AIAA Journal, Vol. 28, No. 8, pp. 1464-1472.

112. Liu, F, and Jameson, A., (1993), "Multigrid Navier-Stokes calculations for three-dimensional cascades," AIAA Journal, Vol. 31, No. 10, pp. 1785-1791.

113. Laufer, J., (1954), "The structure of turbulence in fully developed pipe flow," NACA TM 1174.

114. Mansour, N.N., Kim, J., and Moin, P., (1988), "Reynolds stress and dissipation rate budgets in turbulent

channel flow," Journal of Fluids Mechanics, Vol. 194, pp. 15-44.

115. Klebanoff, P.S., (1955), "Characteristic of turbulence in a boundary layer with zero pressure gradient," NACA TM1247.

116. Ligrani, P.M., and Moffat, R.J., (1986), "Structure of transitionally rough and fully rough turbulent boundary layers," Journal of Fluid Mechanics, Vol. 162, pp. 69-98.

117. Yaras, M.I., and Grosvenor, A.D., (2003), "Evaluation of one- and two-equation low-Re turbulence models. Part I-Axisymmetric separating and swirling flows," Int. J. Numer. Meth. Fluids, Vol. 42, pp. 1293-1319.

118. Patel, V.C., Rodi, W., Scheuerer, G., (1985), "Turbulence models for near-wall and low Reynolds number flows: A review," AIAA Journal, Vol. 23, No.9, pp. 1308-1319.

119. Zhang, H., (1993), "Study of a numerical turbulence model for flow past smooth and rough surfaces," Ph.D. dissertation, Department of Mechanical Engineering, University of Rhode Island.